UNIVERSITY OF PANNONIA

IRON AND MANGANESE COMPLEXES IN BIOMIMETIC CATALYTIC OXIDATIONS

DOI:10.18136/PE.2020.755

PhD. Dissertation

Bashdar Ismael Meena

Supervisor:

Dr. József Kaizer, D.Sc.

Professor of Chemistry

Doctoral School of Chemistry and Environmental Science

Veszprém

2020

IRON AND MANGANESE COMPLEXES IN BIOMIMETIC CATALYTIC OXIDATIONS

Értekezés doktori (PhD) fokozat elnyerése érdekében

Írta: Bashdar Ismael Meena

Készült a Pannon Egyetem Kémiai és Környezettudományi Doktori Iskolájának keretében.

Témavezető: Dr. József Kaizer

Elfogadásra javaslom (igen/nem)

…….……

(aláírás)

A jelölt a doktori szigorlaton ..... %-ot ért el.

Veszprém …….....

Szigorlati Bizottság elnöke

Az értekezést bírálóként elfogadásra javaslom:

Bíráló neve: .....igen/nem

……

(aláírás)

Bíráló neve: .....igen/nem

.....

(aláírás)

A jelölt az értekezés nyilvános vitáján ..... %-ot ért el.

Veszprém .....

Bíráló Bizottság elnöke

A doktori (PhD) oklevél minősítése: .....

.....

EDT elnöke

Abstract

High-valent non-heme iron(IV)-oxo species were proposed as an active oxidant in several catalytic cycles in many biological iron dependent oxygenases. The reactivity of the formerly reported low-spin (S = 1) iron(IV)-oxo complex $[Fe^{IV}(asN4Py)(O)]^{2+}$ (**1b)** with the chiral pentadentate ligand has been investigated in the oxidation reaction of various alkenes, such as, cis-cyclooctene and styrene derivatives. In addition, the oxidation of ethylbenzene by the chiral iron(IV)-oxo intermediate achieves moderate enantioselectivity and high yield.

Manganese-isoindoline complexes such as, $[Mn^{II}(HL^{3})Cl_2]$ (3), $[Mn^{II}(HL^{4})Cl_2]$ (4), $[Mn^{II}(HL^{5})Cl_2]$ (5), $[Mn^{II}(HL^{6})Cl_2]$ (6), $[Mn^{II}(HL^{7})Cl_2]$ (7) and $[Mn^{II}(HL^{8})Cl_2]$ (8), were synthesized and characterized by various electrochemical and spectroscopic methods. Efforts have been made to work out highly efficient and highly selective manganese-based catalytic system for the disproportionation reaction of H_2O_2. After that, investigated the effect of the ligand modification by varying the aryl substituent on the bis-iminoisoindoline moiety with emphasis on the redox potential. The catalase-like activity of the manganese-isoindoline complexes **(3-8)** was studied in an aqueous medium at pH 9.5. We observed that the higher the redox potentials of Mn^{III}/Mn^{II} redox couple the higher is the catalase-like and bleaching activity. The bleaching and catalase-like activity of the catalysts showed a linear correlation with the Mn^{III}/Mn^{II} redox potentials. The manganese-isoindoline complexes **(3-8)** have been used for flavanone oxidation as flavanone oxidase model.

The catalytic oxidation of *N*,*N*-dimethylaniline (DMA) with *meta*-chloro perbenzoic acid (*m*-CPBA), peracetic acid (PAA), hydrogen peroxide (H_2O_2), *tert*-butyl hydroperoxide (TBHP), and iodosobenzene (PhIO), by non-heme $[Mn^{II}(asN4Py)(CH_3CN)](ClO_4)_2$, Mn(II) manganese-isoindoline complexes **(3-8)** and $Mn(ClO_4)_2$ salt, under air and argon atmosphere were also investigated. The main products observed under air were *N*-methylaniline (MA) and *N*-methyl-formanilide (MFA) while under argon atmosphere yielded *N*-methylaniline (MA) as a predominant product.

Acknowledgements

I am very grateful to Professor József Kaizer for inspiration, advice and motivation on this project. I would also like to thank the staff of the chemistry department. I would like to thank Dr. Balázs Kripli. I have to special thanks to Stipendium Hungaricum scholarship programme for the financially support this research work, also I would like to thanks for the ministry of higher education and scientific research of Kurdistan/ Iraq for permission the PhD study.

Last but not least, I have to thank my family and friends. I never would have made it to this point in my life without the support and constant sacrifice of my parents.

Compound abbreviations

(**1a**)	$[Fe^{II}(asN4Py)](CF_3SO_3)_2$
(HL^1)	*N*,*N*-bis(2-pyridylmethyl)-1,2-di(2-pyridyl)ethylamine
(**1b**)	$[Fe^{IV}(asN4Py)(O)]^{2+}$
(**2a**)	(-)-$[Fe^{II}(asN4Py)](CF_3SO_3)_2$
(HL^2)	(-)-*N*,*N*-bis(2-pyridylmethyl)-1,2-di(2-pyridyl)ethylamine
(**2b**)	(-)-$[Fe^{IV}(asN4Py)(O)]^{2+}$
(**3**)	$[Mn^{II}\{(Py)_2\text{-indH}\}(Cl)_2]$
(HL^3)	1,3-bis(2′-pyridylimino)isoindoline
(**4**)	$[Mn^{II}\{(4\text{-Me-Py})_2\text{-indH}\}(Cl)_2]$
(HL^4)	1,3-bis(4′-methyl-2′-pyridylimino)isoindoline
(**5**)	$[Mn^{II}\{(im)_2\text{-indH}\}(Cl)_2]$
(HL^5)	1,3-bis(2′-imidazolylimino)isoindoline
(**6**)	$[Mn^{II}\{(tia)_2\text{-indH}\}(Cl)_2]$
(HL^6)	1,3-bis(2′-tiazolylimino)isoindoline
(**7**)	$[Mn^{II}\{(bim)_2\text{-indH}\}(Cl)_2]$
(HL^7)	1,3-bis(2′-benzimidazolylimino)isoindoline
(**8**)	$[Mn^{II}\{(N\text{-Me-bim})_2\text{-indH}\}(Cl)_2]$
(HL^8)	1,3-bis(*N*-methylbenzimidazolylimino)isoindoline
N3S2	2,6-bis(2-methylthiophenyliminomethyl)pyridine
Cl-acac	3-chloro-acetylacetonate
TMC	1,4,8,11-tetramethyl-1,4,8,11-tetraazacyclotetra-decane
TPFPP	meso-tetrakis(pentafluorophenyl)porphinato dianion
Me_4cyclam	1,4,8,11-tetramethylcyclam
TQA	tris(2-quinolylmethyl)amine

PyMac	2,7,12-trimethyl-3,7,11,17-tetraazabicyclo[11.3.1]heptadeca-1(17),13,15-triene)
Bn-tpen	*N*-benzyl-*N*,*N'*,*N'*-tris(2-pyridylmethyl)-1,2-diaminoethane
Hb4Mepi	1,3-bis(4'-methyl-2'-pyridylimino)isoindoline
TBC	1,4,8,11-tetrabenzyl-1,4,8,11-tetraazacyclotetradecane
Me_3NTB	tris((*N*-methyl-benzimi-dazol-2-yl)methyl)amine
TPA	tris(2-pyridylmethyl)amine
$PhCH(CH_3)_2$	isopropyl benzene
Ph_3CH	triphenyl methane
2,3-DMB	2,3-dimethylbutane
N4Py	*N*,*N*-bis(2-pyridylmethyl)-*N*-bis(2-pyridyl)methylamine
asN4Py	*N*,*N*-bis(2-pyridylmethyl)-1,2-di(2-pyridyl)ethylamine
HRMS	High resolution mass spectroscopy
BDE	Bond dissociation energy
HAT	Hydrogen atom transfer
OAT	Oxygen atom transfer
KIE	Kinetic isotope effect
Me	methyl
OTf	triflate
PhIO	iodosobenzene
MeOH	methanol
MeCN	acetonitrile
ee	Enantiomeric Excess
m-CPBA	*meta*-chloroperoxybenzoic acid
DMA	*N*,*N*-dimethylaniline
MFA	*N*-methylformanilide
TBHP	*tert*-butyl hydroperoxide
TON	Turnover number
TOF	Turnover frequency
PAA	peracetic acid
MA	*N*-methylaniline

H_2O_2	Hydrogen peroxide
ET–PT	Electron transfer–proton transfer
NMR	Nuclear Magnetic Resonance
FTIR	Fourier Transform Infrared Spectroscopy
UV–Vis	Ultraviolet–Visible Spectroscopy
CV	Cyclic Voltammetry
GC-MS	Gas Chromatography Mass Spectrometry
GC	Gas Chromatograph
SCE	Saturated Calomel Electrode
Mebpa	*N*-(2-methoxyethyl)-*N*,*N*-bis (pyridin-2-yl-methyl)amine
BPMCN	*N*,*N*′-bis(2-pyridylmethyl)-*N*,*N*′-dimethyl-1,2-diaminocyclohexane
QBPA	2-quinolylmethyl bis(2-pyridylmethyl)amine
Tpy	2,2’,6’,2”-terpyridine
Bph	benzo-pyrene hydroxylase
Tmeda	*N*,*N*,*N’*,*N’*-tetramethylethylenediamine
Dcbpy	6,6’-dichloro-2,2’-bipyridine
Bpy	2,2-bipyridine
PDPP	1,1′-bis(pyridin-2-ylmethyl)-2,2′-bipyrrolidine
Me_3tacn	1,4,7-trimethyl-1,4,7-triazacyclononane
TMpyP	tetra(N-methylpyridyl)porphine
Tpa	tris-(2-pyridylmethyl)amine
Bpmen	*N,N*′-bis-(2-pyridylmethyl)-*N,N*′-dimethyl-1,2-ethylenediamine
Tmeda	*N*,*N*,*N*,*N*-tetramethylethylenediamine
TF_4TMAP	meso-tetrakis(2,3,5,6-tetrafluoro-4-*N*,*N*,*N*-trim-ethylaniliniumyl) porphyrin
TMG_2dien	2′,2′-(2,2′-(methylazanediyl)bis(ethane-1,2-diyl))bis(1,1,3,3-tetramethylguanidine

1 Introduction

Metalloenzymes play an important role in the majority of biological functions. During the 20th century, the chemists started to search for an understanding of the functions of metallobiomolecules which lead to a field of bio-inorganic chemistry. It deals with the applications of the elementary principles of chemistry in the biophysical processes of living organisms and involves the study of most metallic and some nonmetallic elements in biological systems [1-3]. This research field has been expanded significantly during the past three decades due to several reasons such as, swift preparative methods for metalloproteins, the identification of essential elements in plants, animals and human nutrition, advanced diffraction and spectroscopic techniques especially protein crystallography and nuclear magnetic resonance (NMR) spectroscopy, the improved and facile synthesis of simple and inorganic complexes to mimic the various aspects of biomolecules, and the use of metal complexes for therapeutic agents [2, 4].

The majority of metalloenzymes are proteins which contain metals that are tightly bound and always isolated with protein. About one-half of all known proteins contain metals and most of the proteins depend on metals for their biological functions. Metalloenzymes successfully solved the issue of selectivity in the oxidation of non-activated C-H [5, 6], and C=C bonds under mild conditions [7-9]. Metalloenzymes utilize metals as the cofactors to catalyze a diverse array of biochemical reactions. Even though metal ions only account for less than 1% of the total protein weight, they are essential for the enzyme activity. Moreover, the metal ions can exist in multiple oxidation states and different geometries, and these characteristics are vital to promote complex biochemical transformations and participate in highly specialized biological functions such as, oxygen activation.

The nature of the metal and amino acid residues, the coordination geometry of the metal centre, the relative disposition of the metal in the case of polymetallic systems and the three-dimensional configuration are crucial properties for the reactivity of the metalloprotein. All these factors determine the ability of the metal ion to stabilize different reaction intermediates, sometimes with distinct oxidation states, and they can also alter the shape of the active site that controls the accessibility, and the trajectories of the substrate approaching the metal active centre. The purpose of these systems is to mimic the reactivity of the natural enzyme in catalyzed transformations by using synthetic low molecular weight compounds and provide mechanistic, structural and spectroscopic data for comparison with the biological system. This study is based on the design of suitable ligands to generate functional models with first-row transition metals.

2 Literature review

2.1 The biological role of the metal ions

Recently many successful examples of enzyme redesign to modify the active centre have been reported, showing the possibility of changing the inherent catalytic activity of the enzyme. However, due to the time consumption and inherent difficulty of working with proteins, high molecular weight and complicated purification process, the investigation of synthetic bioinspired model comprise an attractive approach for getting advance information about protein chemistry. Metal ions in metalloproteins are usually coordinated by nitrogen, oxygen or sulfur atoms belonging to amino acids in the polypeptide chain of the protein (Table 1). Most of the living organisms constitute iron with only a few exceptions in the bacterial world [2, 7, 10].

Table 1. Lists of some essential metals and enzymes those containing metals in their active sites

Metal	Examples of Metalloenzymes
Iron	Catalase and Hydrogenase, Oxygenase and Oxidase
Manganese	Arginase
Copper	Cytochrome oxidase and Laccase
Nickel	Urease, Hydrogenase
Cobalt	Methionyl aminopeptidase and Nitrile hydratase

Biologically, iron plays a vital role in oxygen transport and storage as well as in electron transport. A large number of metalloenzymes contain iron in their active sites such as, myoglobin and haemoglobin, which were among the first proteins to be structurally characterized and both of them contain iron protoporphyrin as an essential prosthetic centre.

Metalloenzymes containing iron active site comprises a large group of dioxygen activating enzymes that possess the capability of functionalizing a wide range of organic substrates with high efficiency and selectivity. Iron-containing enzymes can be classified based on the structure of the active site, such as, mononuclear non-heme enzymes and heme enzymes. Many enzymes need cofactor to work properly, which can be metal ions such as, Fe^{2+}, Cu^{2+} and Mg^{2+} or organic molecules, for instance, biotin, haem, NAD and FAD. The complete active enzyme with cofactor is called a holoenzyme [182].

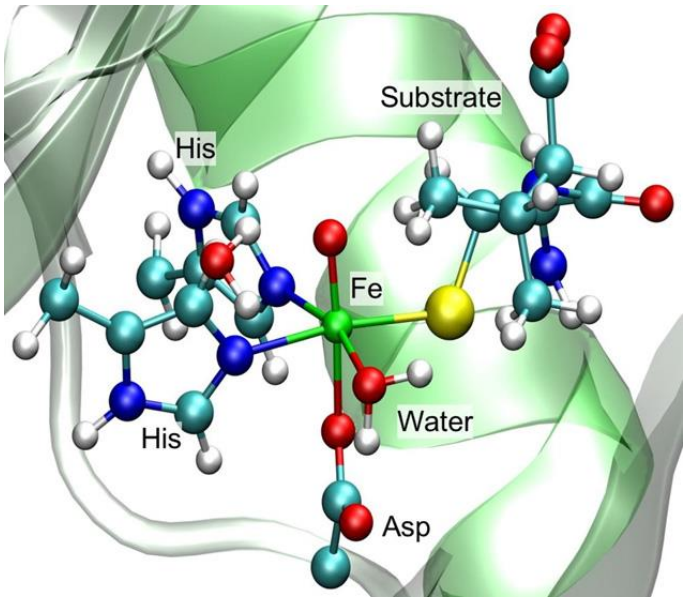

Figure 1. Iron(IV)-oxo intermediate in the mononuclear non-heme iron enzyme isopenicillin *N*-synthase [182].

2.2 Homogeneous catalysis

Catalyst can be classified into two categories, homogeneous and heterogeneous. For the first time, the catalyst was defined in 1894 by Ostwald as a chemical substance that accelerates the reaction without being consumed [11, 12]. In the presence as well as in the absence of the catalyst, the reaction has the same initial and final points, but it occurs through different mechanisms, involving different intermediates and transition states.

The reaction is faster in the presence of the catalyst, which means that it decreases the activation energy of the reaction allowing it to be carried out under milder conditions and more efficiently [13]. Most biological reactions have large activation energies, so without enzymes, they proceed too slowly to be useful. Enzymes reduce the activation energy of a reaction, so that the kinetic energy of most of the molecules exceeds the required activation energy, hence, they can react. For instance, in the case of catalase reaction ($2H_2O_2 \rightarrow 2H_2O + O_2$) the activation energy without a catalyst is 86 kJ mol^{-1}, and just 1 kJ mol^{-1} with the enzyme catalase, and 62 kJ mol^{-1} with an inorganic catalyst (Figure 2) [181].

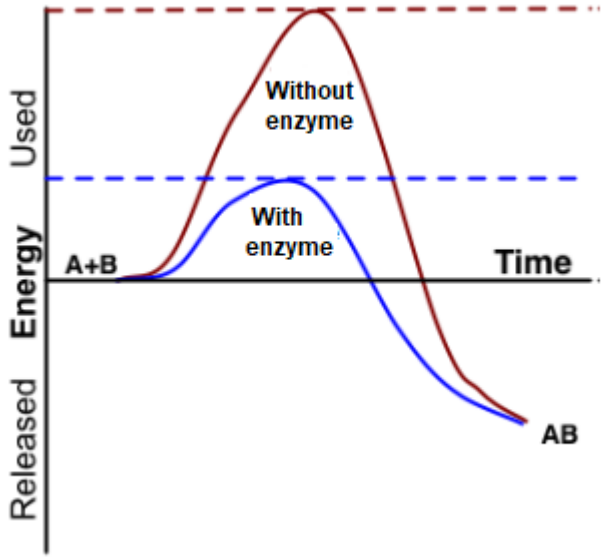

Figure 2. Energy profile in catalase reaction in the presence and absence of enzyme [181]

2.3 Biomimetic heme iron catalysts

High-valent iron complex is supposed as the active oxidant toward bond activation of (C-H). This complex named as Compound I (CpdI) in P450 enzymes has one oxidizing equivalent that is not stored at the iron centre but as a substitute delocalized on the porphyrin macrocycle ring, and formulated as an iron(IV)-oxo unit chelated by porphyrin π-radical [14].

The short-lived nature of this intermediate has long been a difficulty for its assignment as the active oxidant in P450, and only indirectly demonstrated from computational and biomimetic studies [15, 16]. Recently, Green and Rittle have effectively characterized and trapped (CpdI) using UV-Vis, electron paramagnetic resonance and Mössbauer spectroscopic methods, and provided unambiguous proof for its activity in substrate hydroxylation (Figure 3) [16].

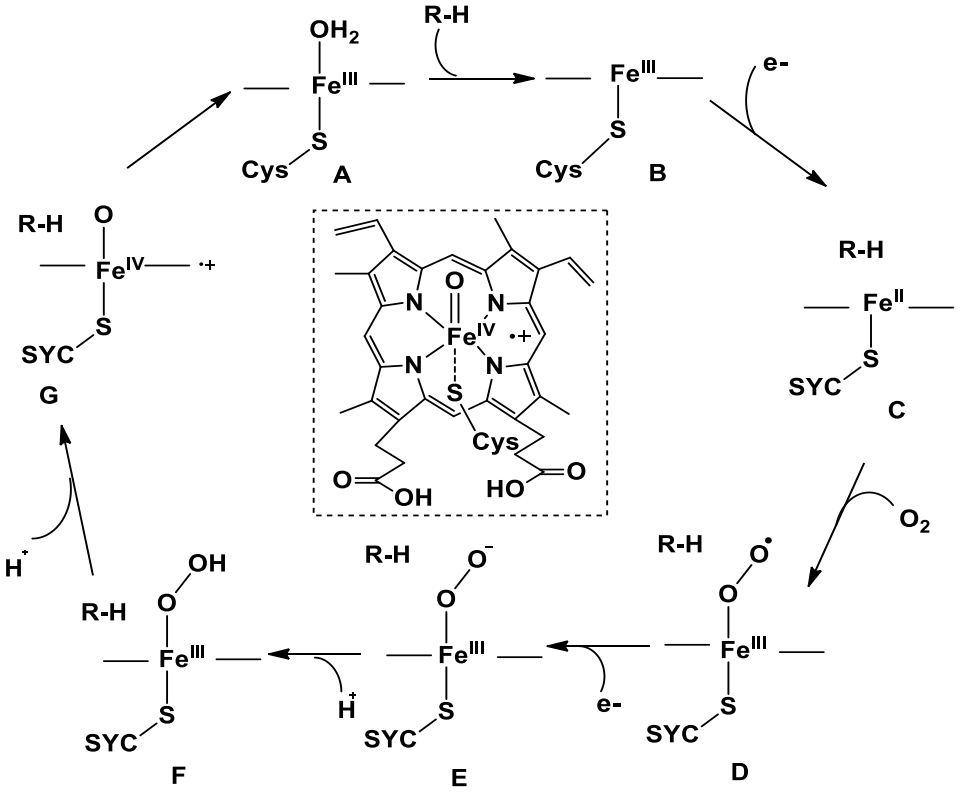

Figure 3. Illustration of different intermediates produced during the catalytic cycle of cytochrome P450 [32]

2.4 Bioinspired non-heme iron enzymes

Metalloenzymes containing non-heme iron centre are common in nature. Several members of this family isolated from plants, mammals and bacteria have now been structurally characterized. Enzymes performing oxidation catalysis can generally be divided into two types: oxidase, use oxygen as an oxidant and reduce dioxygen to H_2O_2 and H_2O, and oxygenase (mono and dioxygenases).

Catalysis the activation and addition of molecular oxygen into organic substrates. Table 2, presented a list of the non-heme metalloenzymes that have been identified to contain mono or diiron active site motif and perform a catalytic function in oxidation reactions [17, 18].

The mononuclear non-heme site is typically penta or hexa-coordinate with one mono or bidentate carboxylate group derived from asparagines, glutamate, cysteine, or tyrosinase and at least two histidines around the iron centre; there are one or two reactive coordination sites that are occupied by water molecules. The mononuclear non-heme iron active sites including enzymes, models, and intermediates have recently been reviewed [19].

Table 2. Selection of important by mono and dinuclear iron(II) with the catalytic function oxidation reaction

Enzyme class	Function	Ref.
α -ketoacid-dependent oxygenases	Unactivated C-H bond oxidation	[2]
Aromatic amino acids hydroxylation	Aromatic amino acid hydroxylases	[20]
Isopenicillin N synthase	Isopenicillin formation	[21]
Lipoxygenases	The unsaturated fatty acid oxidation	[22]
Rieske oxygenase	Arene *cis*-dihydroxylation	[19]
Bleomycin	DNA cleavage	
Alkene monooxygenase	Alkene epoxidation	[19]
Butane monooxygenase	Butane to butanol oxidation	[23]
O-alkane hydroxylase	Alkane to alcohol oxidation	[24]

In contrast to the heme-inspired systems in which the synthesis and characterization of iron(IV)-oxo porphyrin species appeared in 1981 [25], the non-heme iron(IV)-oxo complex appeared almost two decades later in 2000 [26]. For the first time, a non-heme iron(IV)-oxo intermediate was detected spectroscopically in the reaction of $[Fe^{III}(cyclamacetato)(CF_3SO_3)]^+$ and O_3 in acetone and water at –80 ºC by Wieghardt and co-workers [27, 28].

This novel intermediate is a green species, which was characterized as an intermediate-spin (IS) iron(IV)-oxo (S = 1) based on the Mössbauer spectroscopy [26]. Subsequently, the first well-characterized mononuclear non-heme iron(IV)-oxo complex was reported in 2003. Münck, Nam, and Que with their research group presented the first X-ray crystal structure of a mononuclear S = 1 iron(IV)-oxo complex that was produced in the reaction of $[(Me_4cyclam)Fe^{II}(CH_3CN)]^{2+}$ and iodosobenzene (PhIO) in CH_3CN at –40 ºC [29]. This intermediate was characterized with various spectroscopic methods which confirmed the short Fe=O bond distance of 1.646 Å [30, 31]. Later, the researchers investigated the reactivities of mononuclear non-heme iron(IV)-oxo complexes bearing tripodal and macrocyclic tetradentate N4, pentadentate N5 and N4S ligands in the oxidation of a variety of substrates, including olefin epoxidation, alkane hydroxylation, *N*-dealkylation, alcohol oxidation, and the oxidation of sulfides and PPh_3 [27, 32-35].

2.5 Polydentate ligands

Non-macrocyclic polydentate ligands can also support the iron(IV)-oxo unit but with variable thermal stability. The N4Py ligand provides a tertiary amine donor trans to the oxo group and four pyridines bound to the Fe=O unit. The complex $[Fe^{IV}(O)(N4Py)]^{2+}$ has been the most extensively studied in the last few decades. It has a half-life of 60 hours at 25 ºC [36], which was suitable for its crystallization. Its crystal structure showed a Fe=O bond of 1.639 Å, a trans-Fe–N amine bond of 2.033 Å, and average Fe–N, the bond of 1.956 Å [37], while its Fe-O bond [38] is comparable in length to those of $[Fe^{IV}(O)(TMC)(NCCH_3)]^{2+}$ and $[Fe^{IV}(O)(TMC\text{-}Py)]^{2+}$, and the average Fe-N bond length is 0.1 Å shorter, demonstrating the greater ligating ability of the pyridine ligands relative to macrocyclic tertiary amine donors (Figure 4). In recent studies, it has been shown that the polypyridyl complexes of iron are coordinatively stable both in higher and lower oxidation states, and a variety of polypyridyl complexes of iron(IV)-oxo are reportedly known to be effective stoichiometric oxidants toward oxidation of various organic substrates [41].

The oxo atom was shown to drive from water by isotope labelling experiments, $[Fe^{IV}(O)(N4Py)]^{2+}$, the NIR absorption band at 705 nm (ε = 400 M^{-1} cm^{-1}) is comparable in intensity to that of $[Fe^{IV}(O)(TMC)(NCCH_3)]^{2+}$ but significantly blue-shifted in energy [41].

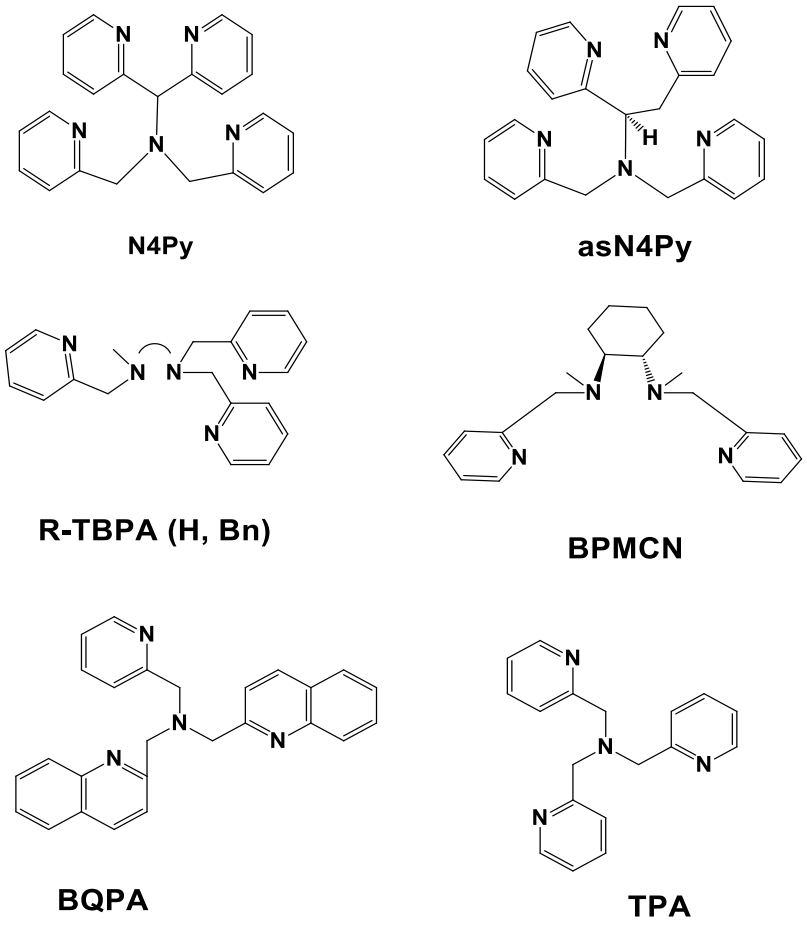

Figure 4. Polydentate chelating ligands used in the synthesis of iron non-heme biomimetic complexes [32]

Besides N4Py, there are other polydentate ligands composed of combinations of pyridine and amine donors in different ligand framework also support the iron(IV)-oxo unit. Generally, these complexes were synthesized by reacting the Fe^{II} precursor with oxidant agents such as, PhIO, *m*-CPBA or BtOH. The well-known examples of pentadentate ligands developed by Comba [42-44]. All these iron(IV)-oxo complexes were found in the S = 1 spin state and revealed significant thermal stability at 25 ºC.

2.6 Comparison between iron(IV)-oxo and iron(V)-oxo complexes

Que and his coworkers achieved significant success in exploring and characterization of iron(IV)-oxo and iron(V)-oxo intermediates, generated from non-heme iron complexes with different co-oxidants such as, PhIO and H_2O_2. For synthetic iron(IV)-oxo intermediates, detailed mechanistic information has been reported [32, 33, 45-47]. Wieghardt with his research group characterized the first non-heme iron(IV)-oxo complex by using Mössbauer spectroscopy and assigned it to a low-spin (S = 1) complex [26]. Until today numerous synthetic non-heme and heme iron(IV)-oxo complexes have been synthesized (Figure 5) and characterized by different spectroscopic techniques such as, X-ray crystallography in some cases. Most of the iron(IV)-oxo species found were low-spin (S = 1), either in solution or in solid-state [48, 49], while only a few compounds revealed a high-spin (S = 2) ground state [50, 51].

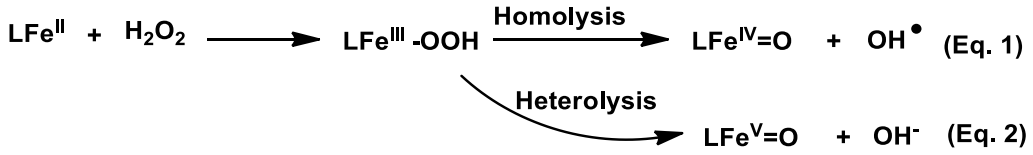

The intermediate (Fe^{III}-OOH) is chemically reactive, due to the weakening of the (O-O) bond and can react in different ways: as oxidant, when the cleavage of the (O-O) bond occurs via the attack of a nucleophile. It can be activated by (O-O) bond homolysis to form iron(IV)-oxo species (Eq. 1) and the short-lived highly reactive HO• radical, which is an immediately transferred to the substrate with suitable ligands, the iron(IV)-oxo species possibly stabilized to act as the key oxidizing species or may undergo (O-O) bond heterolysis to form iron(V)-oxo species (Eq. 2) [52].

Biological system

Heme **Non-heme**

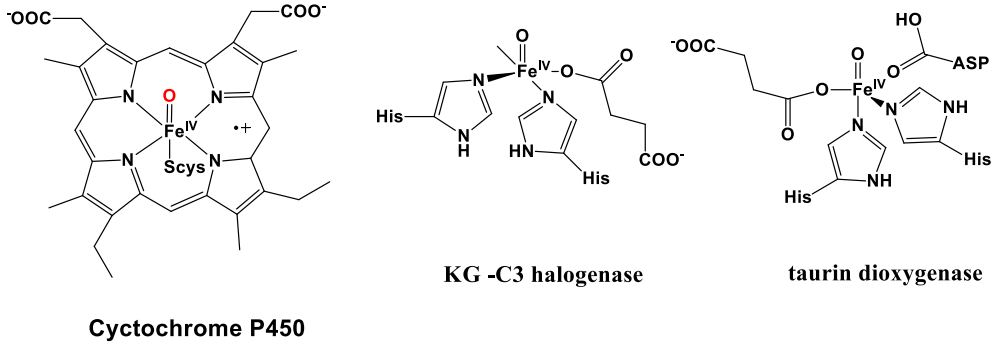

Cyctochrome P450 KG -C3 halogenase taurin dioxygenase

Synthetic model system

Heme

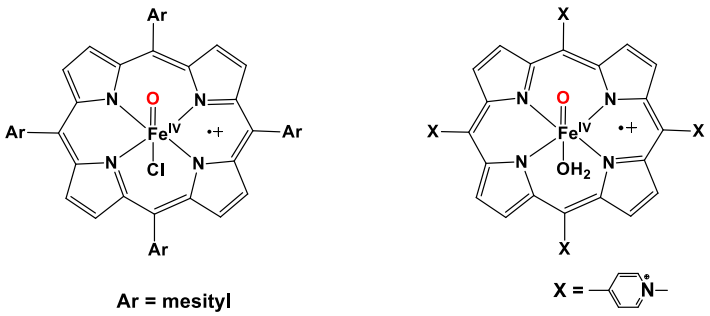

$[(TMP^{\bullet+})Fe^{IV}O(Cl)]$ $[(TMPyP)Fe^{IV}O(H_2O)]^{+}$

Non-heme

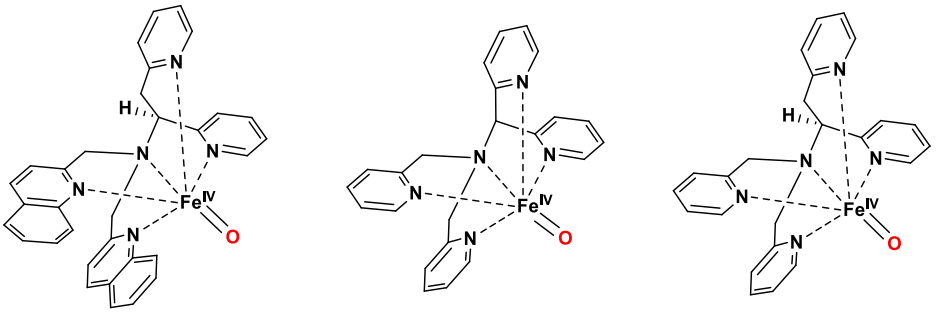

$[(asN2Py2Qu)Fe^{IV}=O]^{2+}$ $[(N4Py)Fe^{IV}=O]^{2+}$ $[(asN4Py)Fe^{IV}=O]^{2+}$

Figure 5. Comparison between the heme enzyme (Fe) [53-55] and non-heme enzymes of (Fe) complexes [55-58]

For the first time, the iron(V)-oxo complex $[(TAML)Fe^{V}=O]^{-}$ was presented in 2007 [59], by the reaction of $[(TAML)Fe^{III}(H_2O)]$ with *m*-CPBA in *n*-butyronitrile at -60 ºC which yielded a deep green complex, confirmed as $[(TAML)Fe^{V}=O]^{-}$ by EPR, Mössbauer, EXAFS and ESI-MS analysis. This low-spin (S = 1/2) complex exhibited a rhombically anisotropic EPR spectrum and was capable of oxidizing various substrates, such as styrene, ethylbenzene, thioanisole, cyclooctene, and 9,10-dihydroanthracene.

Recently, a rapid increase in the number of experimental data supporting the formation of iron(V)-oxo intermediates has been observed. Interestingly these intermediate complexes are considered as active species of the present most active catalyst systems based on non-heme iron complexes with penta-dentate *N*-donor ligands and H_2O_2. Oleg and Alexandra with his research group have carried out the research for $(L^{\bullet+})Fe^{IV}=O$ or $Fe^{V}=O$ species by the use of ferric complex $[Fe^{III}(Me_3tacn)(Cl\text{-}acac)Cl]^{+}$ as a catalyst in the presence of oxone as an oxidant. DFT, EPR, ESI-MS and ^{18}O labelling experiments revealed the intermediate $[(Me_3tacn)Fe^{IV}=O\ (Cl\text{-}acac)^{\bullet+}]$ as an active species in catalysis [59]. The active species of iron(IV)-oxo are considered reliable in the catalyst systems supported on non-heme type iron complexes [60, 61].

2.7 Synthetic non-heme iron(IV)-oxo systems

Karl Weighardt and co-worker in the year 2000, for the first time, synthesized and characterized non-heme high-valent iron(IV)-oxo complex by Mössbauer spectroscopy and assigned it to a low-spin (S = 1) of the complex $[Fe^{III}(cyclam\text{-}acetate)(CF_3SO_3)]^{+}$ [62]. Nam and Que have synthesized another family of iron(IV)-oxo intermediates having tripodal ligands, $[Fe^{IV}(O)TPA]^{2+}$ [63].

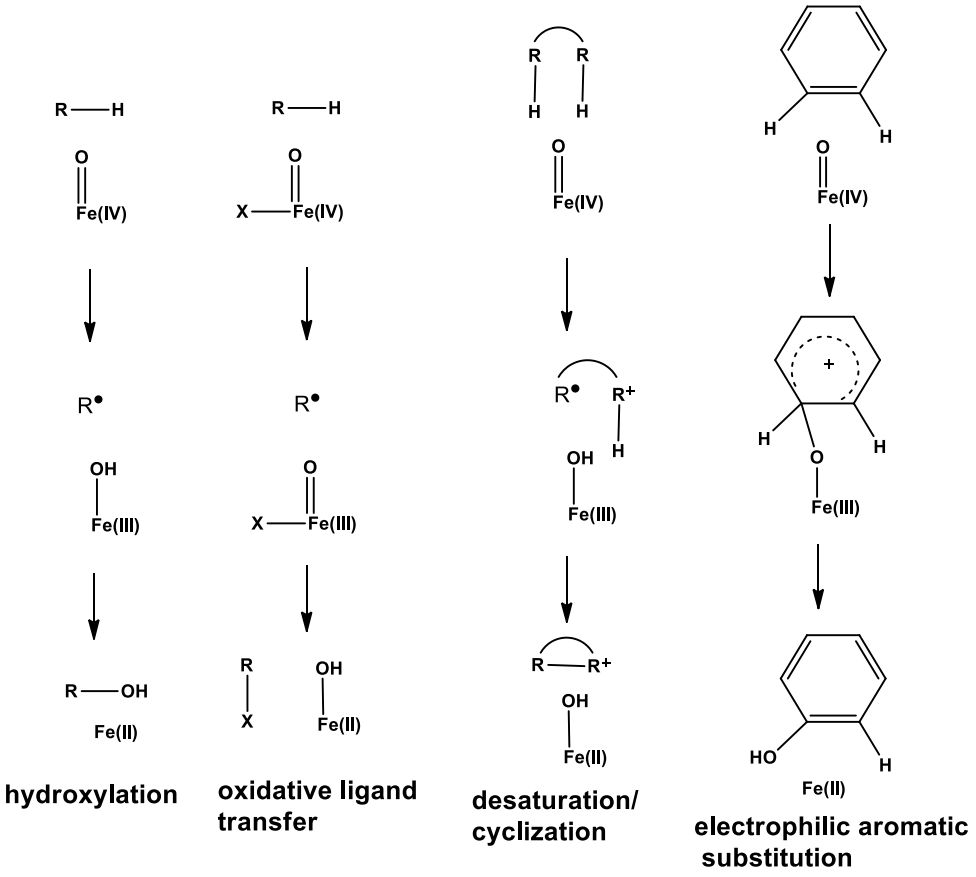

Figure 6. Reactions proposed to be mediated by high-valent Fe(IV)-oxo intermediates [55]

2.8 Oxidants used in the generation of high-valent iron intermediates

In the literature so far, many types of oxidants have been used to achieve non-heme iron(IV)-oxo complexes. Some of the well-known oxygen transfer oxidants are PhIO, *m*-CPBA, tBOOH, PAA and H_2O_2. Iron(IV)-oxo intermediate was generated by the ozonolysis of iron cyclam-acetate [63]. On the other hand, high-valent iron(IV)-oxo intermediates have been produced by two-electron oxidation of the metal complexes in the presence of water as a source of oxygen. Cerium(IV) ammonium nitrate is a potentially strong one-electron oxidant which is usually used for the production of iron(IV)-oxo intermediates [40]. Interestingly iron(IV)-oxo intermediates can also be generated by the combination of a photosensitizer with a weak one-electron oxidant using water as an oxygen source.

Que and his research group presented an indirect way to generate iron(IV)-oxo intermediates wherein, Fe^{III}-OOR complex was converted into iron(IV)-oxo complex with pyridine-N-oxides by homolytic O-O cleavage [64]. They also reported the electrochemical generation of iron(IV)-oxo species in the presence of water [65]. Recently, it has been reported that the treatment of iron(III)-peroxo complexes with Sc^{+3} yields iron(IV)-oxo intermediates [66]. The dioxygen activation of iron(II) complexes with a proton can also generate iron(IV)-oxo intermediates [20] (Scheme 1).

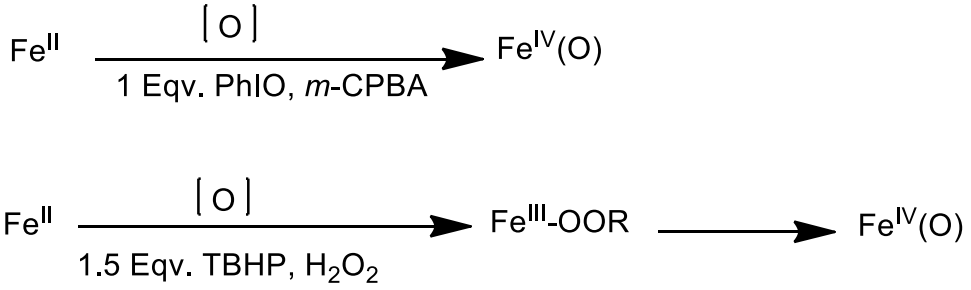

Scheme 1. Generation of high-valent iron intermediates by using different oxidants

2.9 Reactions of non-heme iron(IV)-oxo

Synthetic non-heme iron(IV)-oxo complexes are capable to react with many organic substrates. The well-known studies regarding oxidation reactions relating iron(IV)-oxo species are alkene epoxidation, alcohol oxidation, aliphatic and aromatic hydroxylation, hydride transfer, hydrogen atom abstraction phosphorous oxidation, electron transfer, halide oxidation, and *N*-dealkylation (Figure 7).

Some of the key reactions involving iron(IV)-oxo complexes relevant to this research work include oxidation reactions which are the frequently used substrates to demonstrate Oxygen Atom Transfer (OAT) reactions. Oxygen Atom Transfer is a two-electron oxidation reaction based on S- and P- wherein the transfer of oxygen atom occurred from iron(IV)-oxo to the substrate. The ^{18}O labelled experiments provided the deep and mechanistic insights of OAT [36, 67].

The Hydrogen Atom Transfer (HAT) mechanism based on successive two-electron reactions involving iron(IV)-oxo intermediates, oxidizes organic substrates such as, indene, triphenylmethane, 1,4-cyclohexadiene (CHD) and fluorene to evaluate HAT reactions. The mechanistic conclusion usually comes from the observation of KIE values. The OAT and HAT both have been considered as the key reactions to understand the factors influencing the reactivity of iron(IV)-oxo complexes.

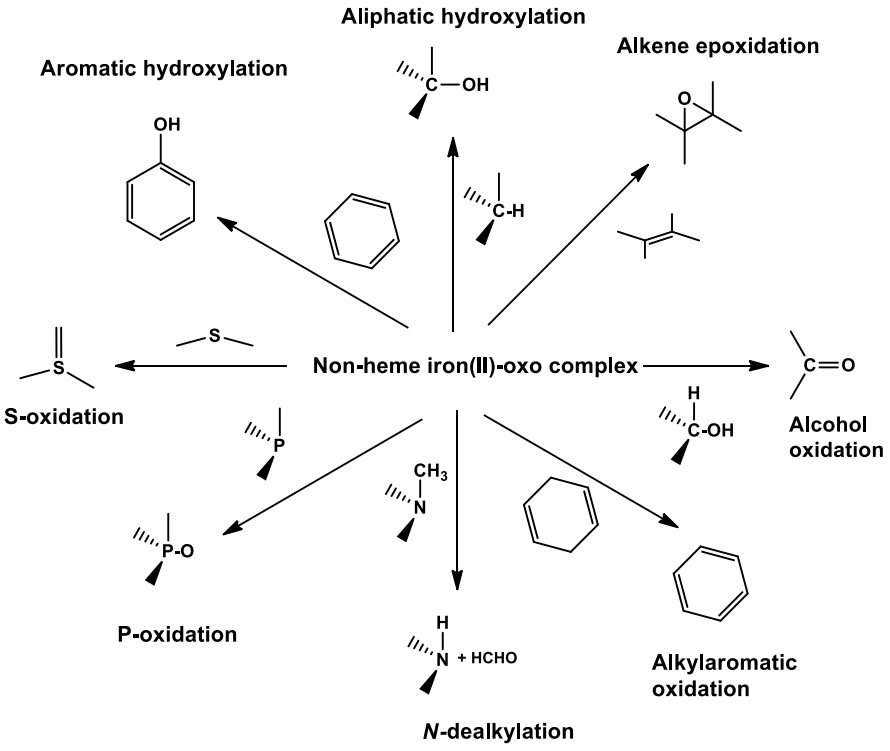

Figure 7. Reactions related to synthetic non-heme iron(IV)-oxo complexes [55]

Recently, the concept of H^+/e- transfer processes have been presented by Meyer and Costentin [183], which is named as, proton-coupled electron transfer (PCET). It includes many redox processes where the rate or energetics are affected by one or more protons, involving processes in which protons and electrons transfer among one or more reactants, by concerted. Hammarström and co-workers used the term concerted electron/proton (CEP), which contrasts with stepwise processes involving either initial PT followed by ET, or ET followed by PT [183].

The reactivity and stability of iron(IV)-oxo complexes depend on many factors, such as the structure of the ligand and the spin state (Table 4 and 5). Complex $[Fe^{IV}(O)(TMC)(CH_3CN)]^{2+}$ showed low reactivity in the HAT and OAT reactions, so a slight modification was made to the complex $[Fe^{IV}(O)(13\text{-}TMC)(CH_3CN)]^{2+}$ [68], which is more reactive complex in the reactions [49]. Complexes of N4Py and Bn-TPEN five donor ligands were highly reactive in oxidation reactions, but Me_3NTB complexes of four donor ligand achieved several orders of magnitude higher reaction rates as mentioned in (Table 3), [49]. During the oxidation of ethylbenzene, the complex $[Fe^{IV}(O)(TBC)(CH_3CN)]^{2+}$ is more reactive than the complex $[Fe^{IV}(O)(N4Py)(CH_3CN)]^{2+}$ [69].

Table 3. Reactivity of (L) Fe^{IV} complexes in OAT and HAT at -40 °C.

	k_{obs} L= TMC	k_{obs} 13-TMC	k_{obs} N4Py	k_{obs} TMG_3TR	k_{obs} Me_3NTB	k_{obs} Bn-TPEN	k_{obs} TBC
$PhCH(CH_3)_2$			2.0×10^{-3} (s^{-1})		1.0×10^{0} (s^{-1})		
Ph_3CH			3.7×10^{-2} (s^{-1})		1.0×10^{1} (s^{-1})		
$AcrH_2$	1.0×10^{0}	5.4×10^{2} (s^{-1})					
PhMe			2.1×10^{-4} (s^{-1})		4.7×10^{-1} (s^{-1})		
DHA	2.5×10^{-3}	$5.\times10^{0}$ (s^{-1})	8.0×10^{-1} (s^{-1})		3.1×10^{3} (s^{-1})	8.8×10^{0}	
PhEt	9.6×10^{-5}		1.2×10^{-3} (s^{-1})		1.5×10^{0} (s^{-1})		1.5×10^{-2}
C_6H_{12}			4.6×10^{-6} (s^{-1})		2.5×10^{-1} (s^{-1})		
2,3-DMB			6.0×10^{-5} (s^{-1})		2.9×10^{-1} (s^{-1})		
PPh_3			1.5×10^{0} (s^{-1})	1.3×10^{0}		1.7×10^{1}	
CHD	6.4×10^{-4}	5.4×10^{0} (s^{-1})	5.0×10^{-1} (s^{-1})	1.2×10^{0}	9.4×10^{2} (s^{-1})	5.7×10^{0}	
PhSMe	1.3×10^{-3}	4.3×10^{2} (s^{-1})	2.4×10^{-4} (s^{-1})		2.1×10^{4} (s^{-1})	1.4×10^{-2}	2.0×10^{1}

Table 4. Structural and spectroscopic characteristics of S = 2 for non-heme Fe complexes

Complexes	λ_{max} (nm), (ε (M^{-1} cm^{-1}))	δ (mm/s)	ΔE_Q (mm/s)	D (cm^{-1})	Fe-O (Å)	νFe=0 (cm^{-1})	Ref.
S = 2 Fe^{IV} = O							
$[Fe^{IV}(O)(H_2O)_5]^{2+}$	320 (500)	0.38	0.33	9.7	-	-	[70]
$[Fe^{IV}(O)(tpaPh)]^{-}$	400 (-) (900)	0.09	0.51	4.3	1.62	850	[71]
$[Fe^{IV}(O)TMG_2dien)(X)]^{2+/+}$							
X= $NCCH_3$	380 (8200) 805 (270)	0.08	0.58	4.5	1,65	807	[45]
N_3	412 (9700) 827 (290)	0.12	-0.30	4.6	-	833	[45]

Table 5. Structural and spectroscopic characteristics of S = 1 for non-heme Fe complexes

Complexes	λ_{max} (nm), (ε (M^{-1} cm^{-1}))	δ (mm/s)	ΔE_Q (mm/s)	D (cm^{-1})	Fe-O (Å)	νFe=0 (cm^{-1})	Ref.
S = 1 Fe^{IV} = O							
$[Fe^{IV}(O)(cyclam\text{-}CH_2CO_2)]^{+}$	676 (−)	0.01	1.37	23	-	-	[26]
$[Fe^{IV}(O)(TMC)(X)]^{2+}$							
X = $NCCH_3$	824 (400)	0.17	1.24	29	1.646	839	[72]
-CN	858 (250)	0.15	0.25	31	1.66	823	[73]
-N_3	850 (130)	0.17	0.70	29	1.66	814	[73]
$[Fe^{IV}(O)(TMC\text{-}Py)]^{2+}$	834 (260)	0.18	1.08	29	1.66	826	[74]
$[Fe^{IV}(O)(TBC)(NCCH_3)]^{2+}$	885 (360)	0.22	0.97	29,5	1.64	842	[69]
$[Fe^{IV}(O)(TMCSO_2)]^{+}$	830 (170)	0.19	1.29	-		831	[75]
$[Fe^{IV}(O)(PyMAC)]^{2+}$	705 (230)	0.03	2.00	-	-	-	[76]
$[Fe^{IV}(O)(15\text{-}TMC)]^{2+}$	890 (−)	-	-	-	-	-	[77]
$[Fe^{IV}(O)(Bn\text{-}TPEN)]^{2+}$	740 (400)	0.01	0.87	-	1.67	-	[78]
$[Fe^{IV}(O)(Me\text{-}TPEN)]^{2+}$	756 (-)	-	-	-	-	-	[79]
$[Fe^{IV}(O)(TPEN)]^{2+}$	730 (380)	0.01	0.87	-	-	818	[78]

Recently, the understanding of catalytic reactions based on mechanistic studies of the enzymes and their model compounds, and the nature of active oxidizing species have been improved. One of the well-known examples is the catalytic cycle of dioxygen activation and oxygen atom transfer by α-KG dependent oxygenases (TauD) (Figure 8). Since decades, the high-valent non-heme iron(IV)-oxo intermediates have been considered as key candidates in many biological oxidation processes [23, 80].

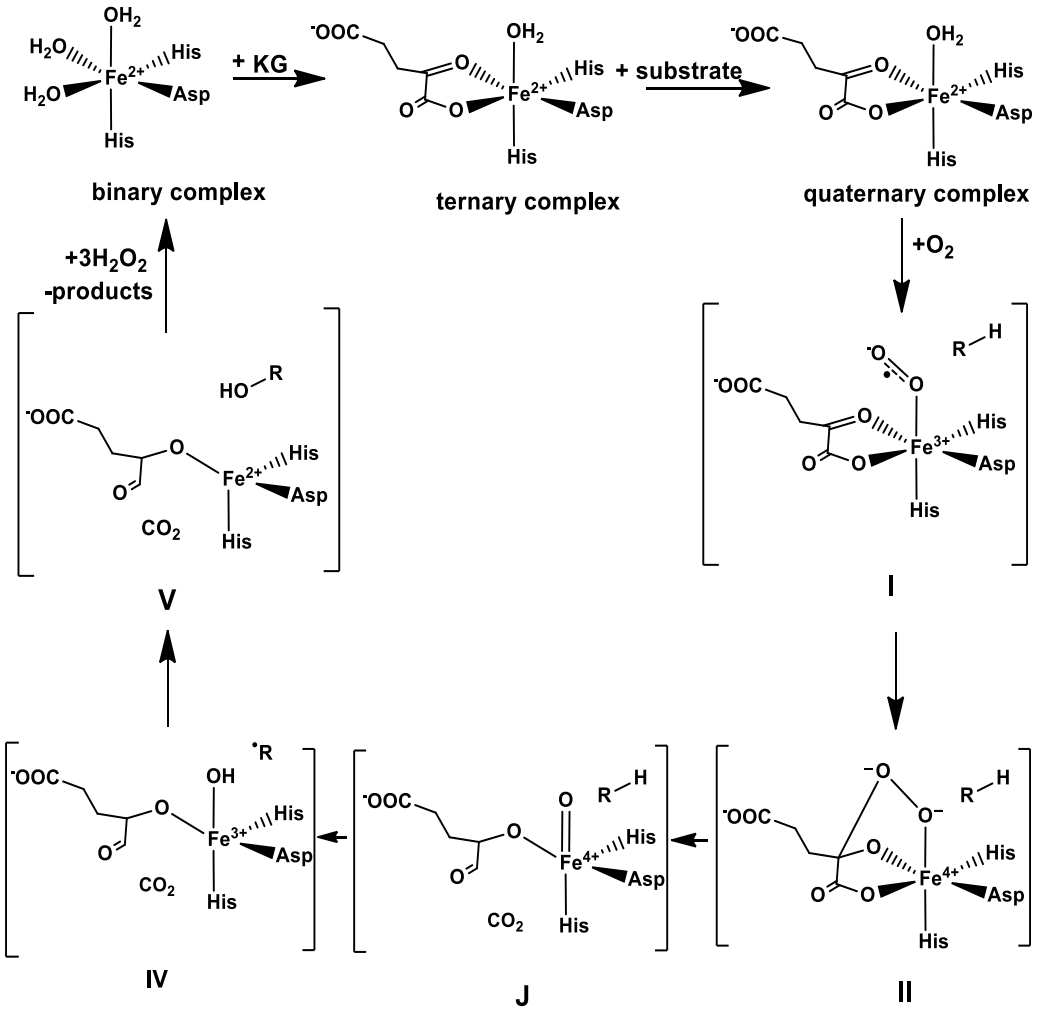

Figure 8. Proposed mechanism of Taurine α-KG dioxygenase [81]

Taurine α-KG dioxygenase (TauD) intermediates were first of mononuclear nonheme iron enzyme presents the creation of an iron(IV)-oxo intermediate (TauD-J) as an active oxidizing species, which has been characterized using various spectroscopic techniques. For most of the α-KG-dependent enzymes, large kinetic isotope effects (KIEs) value greater than 50 were established for the decay of iron(IV)-oxo intermediates in the presence of deuterated substrates, which authenticated the contribution of the iron(IV)-oxo intermediates reactions. The iron(IV)-oxo intermediate is considered to be responsible for the one-electron oxidation of the substrate, which is essential to start the epimerization process mimic their high-valent oxoiron intermediates and emulate their reactivities [81].

2.10 Catalytic epoxidation of olefins by iron (II) complexes

In current studies, it has been investigated that the iron-based polypyridyl complexes are coordinatively stable both in lower and higher oxidation states, and various types of polypyridyl complexes of iron(IV)-oxo are recognized to be efficient stoichiometric oxidants toward oxidation of different organic substrates by oxygen atom transfer (OAT), electron transfer-proton transfer (ET-PT) [82, 83], hydrogen atom transfer (HAT), and electron transfer (ET) reactions [36, 84].

Despite, the widespread interest in ruthenium(IV)-oxo mediated epoxidations [90], there is relatively rare information on the mechanism of alkene oxidations by synthetic, non-heme iron(IV)-oxo complexes. This is mainly as a result of the low stability of the high valent iron(IV)-oxo intermediates which have prevented direct kinetic measurements on their reactions at ambient temperature.

Table 6. Comparison of the efficiency of various iron(IV)-oxo and ruthenium(IV)-oxo complexes toward the oxidation of styrene and *cis*-cyclooctene in acetonitrile

Complex/Substrate	k_2/M^{-1} s^{-1} (°C)	Epoxid/ keton (%)	$\Delta H^{\neq}$(kJ mol^{-1})	$\Delta S^{\neq}$(Jm ol^{-1} K^{-1})	TE	Ref
$[Fe^{IV}(asN4Py)(O)]^{2+}$/ styrene	2.94×10^{-4} (25)	65/12	70.6	-76.4	+0.19	[85]
$[Fe^{IV}(asN4Py)(O)]^{2+}$/cis-cyclooctene	5.41×10^{-4} (25)	75/7	38	-180	-	[85]
$[Fe^{IV}(N3S2)(O)]^{2+}$/ styrene	2.6×10^{-2} (25)	60/20	72	-32	-2.0	[86]
$[Fe^{IV}(PyMac)(O)]^{2+}$/ cyclooctene	0.45 (0)	80	23	-169	n.a.	[76]
$[Fe^{IV}(TQA)(O)]^{2+}$/ cyclooctene	3.3 (-40)	80	n.a.	n.a.	n.a.	[87]
$[Ru^{IV}(tpy)(pic)(O)]^{+}$/ styrene	2.27×10^{-2} (25)	64/11	38.5	-147	+0.16	[87]
$[Ru^{IV}(tpy)(tmeda)(O)]^{2+}$/ styrene	1.95×10^{-2} (25)	64/12	38.1	-151	+0.43	[88]
$[Ru^{IV}(Me_3tacn)(bpy)(O)]^{2+}$/ styrene	1.30×10^{-3} (25)	62/12	42.3	-159	+0.5	[89]

Table 7. Catalytic oxidation of cyclooctene catalyzed by mononuclear iron(II) complexes

Catalyst	Substrate	% diol	epoxide %	Ref.
$[Fe(N4Py)(CH_3CN)](ClO_4)$	Cyclooctene	0	0.6	[91]
$[Fe(bph)(CH_3CN)_2](ClO_4)_2$	Cyclooctene	0	2.5	[92]
$[Fe(cyclam)(CH_3CN)_2](ClO_4)_2$	Cyclohexene	0	20	[93]
$[Fe(N4Py)(CH_3CN)](ClO_4)_2$	Cyclooctene	0	0.6	[94]
$[Fe(mebpa)Cl](ClO_4)_2$	Cyclooctene	0	20	[92]
$(Me4N)[Fe_2(L_3)(OAc)_2]$	Cyclohexene	0	10	[95]
$[Fe(tpa)(CH_3CN)_2](ClO_4)_2$	Cyclooctene	0	2.6	[96]

2.11 Catalytic oxidation of C-H by iron(II) complexes

Commonly used metalloproteins utilize the oxidative power of dioxygen to catalyse a broad spectrum of key metabolizing reactions, which have medical, pharmaceutical, commercial and agricultural significance [2, 18]. The preparation of enantiopure compounds for drug production and agricultural chemicals is one of the most dynamic fields in organic chemistry, but the big challenge is the asymmetric functionalization of sp^3 C-H bonds, including the asymmetric hydroxylation of alkanes [97, 98]. Extensive research has been carried out on non-heme iron enzymes, and their related biomimetic complexes, such as the reactivity and formation of high-valent oxoiron species [99, 100]. The mentioned systems are accountable for a broad range of oxidative transformations. Fe(II)/α-ketoglutarate dependent taurine dioxygenase, that catalyses the hydroxylation of taurine yielding sulfite and amino acetaldehyde, is one of the famous nonheme iron enzymes which is capable to carry out enantioselective and stereospecific C-H oxidation, where the production of (O_2^-) derived high-valent iron(IV)-oxo was proposed as the iron-based oxidant [101]. Our research group had been successful in getting well-characterized synthetic analogues of high-valent non-heme iron species with chiral ligands, $[Fe^{IV}(asN4Py)(O)]^{2+}$ (**2b**) which serve as synthetic models for non-heme iron-dependent oxygenases [102]**.**

2.12 Manganese redox enzymes

There are several well-known enzymes, that contains manganese in their active site such as transferases, lectins, oxidoreductases, isomerases, ligases, hydrolases, lyases, and integrins [103]. Few classes of the enzyme are involved in catalytic transformations (Table 8). The dioxygen evolving complex of manganese catalase and Photosystem II (PSII) is among the deeply studied manganese enzymes [104]. The oxygen evolving complex (OEC) is involved during the initial stages of the overall photosynthetic processes, in which NADPH is formed for carbohydrate biosynthesis. The OEC catalyses the photo-induced oxidation of water, thereby releasing molecular dioxygen [105, 106].

Table 8. Selection of important mono and dinuclear Mn(II) in the catalytic oxidation reactions

Enzyme class	Function	Ref.
Mn catalase	Hydrogen peroxide decomposition	[107]
Oxygen evolving complex	Water to dioxygen conversion	[106]
Mn lipoxygenase	The polyunsaturated fatty acid oxidation	[107]

2.13 Isoindoline ligand derivatives (pincer-type)

Since the late 1970s, pincer-type ligands have been broadly investigated in organometallic chemistry and homogeneous catalysis [109]. The term pincer is usually used for all meridionally coordinating tridentate chelate ligands. The ancillary ligands present the coordination chemistry of transition-metal complexes and also describe their physical and chemical properties [108, 109]. The use of pincer structures in metal complexes has led to extraordinary achievements in the field of small molecule bond activation, which is related to catalytic applications [110].

In 1952, Elvidge and Linstead reported the first 1,3-bis(2'-pyridylimino) isoindoline (bpi) ligand as a byproduct of phthalocyanine derivatives, which are consumed as organic dyes. The bpi structure consists of a central isoindoline group that is connected to two pyridyl rings with imine moieties (Scheme 2) [111]. The exploration into the coordination chemistry of metal– bpi complexes initiated in the early 1970s, and bpi-type ligands typically coordinate in a meridional tridentate (*N*,*N*,*N*) style to the metal centre as an L_3-type donor [112]. Until now, bispidine (bpi) scaffolds have been in use as pincer ligands with the full range of transition metals, including Mn^{II} [113, 114].

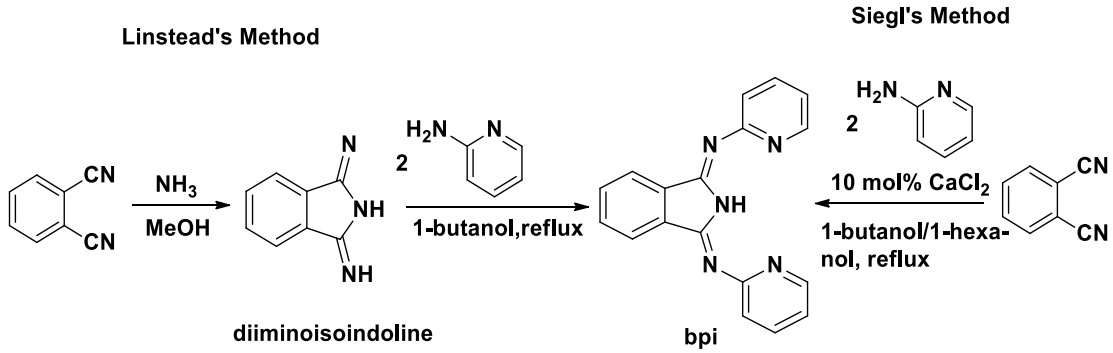

Scheme 2. Synthesis of bis(pyridylimino)isoindoline compounds

Recent advancements established bpi metal complexes as versatile and tunable structural building blocks for attractive applications in the field of enzyme modelling such as, catalase [114, 115], and phenoxazinone synthases [116]. These complexes exhibit a vast range of applications in the field of material science including photoactive materials [117], ion sensors [117], and molecular electronics [118]. However, in some cases, these transition-metal complexes have appeared as molecular catalysts in oxidation [118-120], asymmetric hydrosilylation [121], and hydrogenation reactions [119].

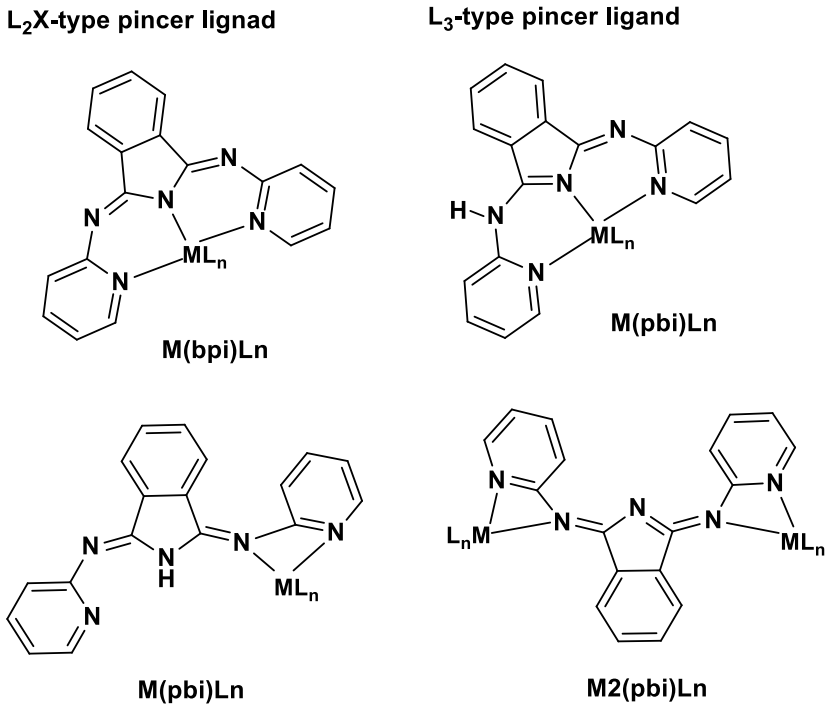

Scheme 3. Coordination modes of bis(pyridylimino)isoindoline ligand

The imine patterns on the bpi structure strongly influence the electronic and structural properties of the free ligand and the coordinated complexes [111]. The double bond of the imine linkers extends the π system throughout the bpi scaffold, which forces a planar structure and improves the robustness and rigidity of the system (Scheme 3) [122]. Depending on the exchange pattern in the pyridyl rings, for example sterically encumbered groups ortho to the pyridyl nitrogens, this planar confirmation may be disrupted by the twisting of the pyridyl groups out of the molecular plane. Additionally, the N–H proton lies in the plane of the molecule and display hydrogen bonding to the pyridyl nitrogen atoms, which is revealed by a downfield chemical shift of the N–H hydrogens (12–14 ppm) in the ^{1}H NMR spectrum. The N–H functionality coupled with imine groups, whose lone electron pair can be engaged upon protonation (Scheme 4), enable proton-responsive activity in bpi compounds depending on the pH environment [123].

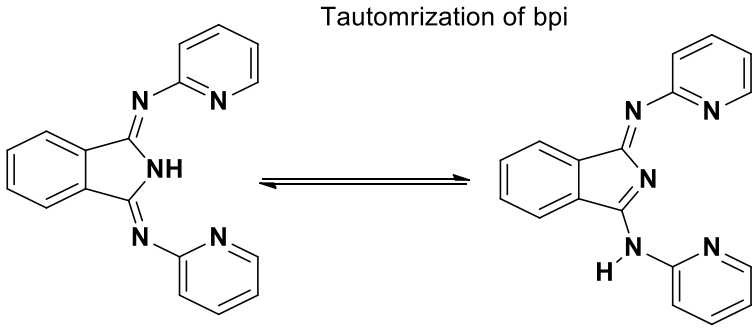

Scheme 4. Structure of the ligand and the possible tautomerization

2.14 Ligand design for biomimetic non-heme Mn and Fe complexes

Knowledge of homogeneous catalysis at the metal centres of model complexes depends upon the understanding and progress of their chemical reactivity. The selectivity and stability of a catalyst are strongly linked to its molecular structure. Consideration of electronic, steric, and conformational properties is mandatory to design suitable ligands for the synthesis of various catalysts [25]. The main aim is the development of practical biomimetic catalysts to design sterically demanding polydentate ligands that can attach one or two metal centres and grasp them in proximity.

These ligands must be strongly electron-donating and also be resistant to oxidation, due to high oxidation states. Additionally, these ligands should exhibit versatility to bind various metal centres, to be able to control the reactivity by changing the metal ions.

Another way to modulate the reactivity of the catalyst can be accomplished by modification of the ligand donor properties. As far as hydrocarbon oxidation is concerned, a selective and rapid C-H bond activation is required. Particularly in the case of manganese/hydrogen peroxide catalyzed oxidations. This can be achieved by using strongly electron-donating ligands, which allow stabilization of high-valent metal complexes. The ancillary *N*-donor ligands take part in the making and stabilization of high-valent manganese species, which has been characterized by extensive EXAFS, EPR, and X-ray analysis [106].

Manganese has a distinctive role in bioinspired, most of the enzymes possess manganese (II or III) cofactor. The data in Table 9, contains the characteristic features of the manganese complexes. The distance between the amino group of the isoindoline core and the metal ion varies in a narrow interval among the manganese complexes.

Table 9. (a) The average pyridyl N–Mn distance, (b) The isoindoline N(H)–Mn distance [124]

Complex	N_{py}-Mn(Å)	N(H)-Mn (Å)	T(¢)	Ref.
$[Mn^{II}(ind)_2]$	2.295	2.163	-	[125]
$[Mn^{II}(indH)Cl_2]$	2.249	2.153	0.69	[126]
$[Mn^{II}(3\text{-Me-BPI})_2]$	2.293	2.144	-	[127]
$[Mn^{II}(bimindH)Cl_2](DMF)$	1.959	2.007	0.93	[128]
$[Mn^{II}(6\text{-}Me_2\text{-}indH)(H_2O)_2(CH_3CN)](ClO_4)_2$	-	-	-	[114]
$[Me^{II}(Mebimind)_2]$	-	-	-	[129]
$[Mn^{II}(bimind)_2]$	-	-	-	[129]
$[Mn^{II}(BTI)_2]$	2.220	2.211	-	[129]

Table 9. (a) The average pyridyl N–Fe distance, (b) The isoindoline N(H)–Fe distance [124]

Complex	N_{py}-Fe (Å)	N(H)-Fe (Å)	T(¢)	Ref.
$[Fe^{II}(ind)CH_3CN)](ClO_4)_2$	2.200	2.072	-	[130]
$[Fe^{III}(bimind)_2]$	1.979	1.912	-	[131]
$[Fe^{III}(4\text{-Me-ind})Cl_2)]$	2.144	1.978	0.77	[132]
$[Fe^{III}(ind)Cl_2$	2.148	1.963	0.86	[133]
$[Fe^{II}(Mebimind)_2]$	2.136	2.057	-	[127]
$[Fe^{II}(bimind)_2]$	2.067	2.045	-	[134]
$[Fe^{III}(BTI)Cl_2]$	2.095	2.019	0.83	[132]
$[Fe^{III}(BTI)_2]MeCN$	2.002	1.928	-	[127]
$[Fe^{III}(5\text{-Me-BTI})Cl_2]$	2.098	2.029	0.59	[135]
$[Fe_2^{III}(\mu\text{-}O(ind)_2Cl_2)]THF$	2.153	1.998	0.88	[136]

2.15 Investigation of manganese(IV)-oxo and manganese(V)-oxo complexes

So far some manganese(IV)-oxo compounds have been characterized by different spectroscopic analysis such as, IR, UV-vis, ESI-MS, EPR and X-ray [137]. Groves and coworkers for the first time reported the characterization of complex namely, mononuclear manganese(IV)-oxo for porphirinic ligand and the oxidation of (chloro)(5,10,15,20-tetramesitylporphirinato)manganese(III) [(TMP)-Mn^{III}Cl] in the presence of peroxy acid results in intermediates such as, [(TMP)Mn^{IV}=O] and [(TMP)Mn^{IV}=O(OH)] which are stable manganese(IV)-oxo porphyrin complexes [137, 138]. These complexes have the capability of relocating their oxo group to olefins to give epoxides. However, a significant change in the reactivity of the manganese(IV)-oxo and manganese(V)-oxo was reported. Particularly, the manganese(IV)-oxo complexes gradually exchanged their terminal oxo groups in the ^{18}O-water medium. For example, a highly reactive manganese(IV)-oxo complex $[(Bn\text{-}TPEN)Mn^{IV}=O]^{2+}$ was presented by Nam with his coworkers [139], which was analyzed by ESI-MS, UV-vis, and EPR analytical techniques.

These complexes confirmed high reactivity in the oxidation of a variety of substrates, such as, aromatic compounds and olefins. On the other hand, the manganese(V)-oxo intermediates have been proven to be a highly reactive species during the catalytic oxygenation of organic substrates by utilizing a variety of oxidants in the presence of manganese(III) porphyrins [140,141]. In addition, these complexes were low-spin d^2 configuration diamagnetic and stable at ambient temperature rather than reactive in oxygen atom transfer reactions. Up to date, successful research for reactive manganese(V)-oxo complexes supported by porphyrinic ligands has been carried out. Groves and his coworkers reported the synthesis and ultraviolet-visible (UV-Vis) characterization of the first manganese(V)-oxo porphyrin complex $[(TM\text{-}4\text{-}PyP)Mn^{V}{=}O]^{5+}$ in an aqueous medium [142]. The attention towards non-porphyrinic manganese catalysts increased considerably soon after the synthesis of manganese salen-type catalysts by Jacobsen and Katsuki [143-145].

2.16 Oxidation reactions catalyzed by bis(pyridylimino)isoindoline complexes

The investigation of the coordination chemistry related to transition-metal bpi complexes; and their catalytic capabilities in oxidative catalysis has been presented by many studies. The hydrogen peroxide produced as a by-product in respiration possesses harmful effects on cells. Moreover, non-hem catalases are considered a suitable choice for biomimetic or catalytic applications due to free sites at the metal centre. The isoindoline derivatives in (Scheme 4) can bind to the metal ion in the neutral or anionic form [120, 146]. The tridentate ligands with N3 donor sets are a well-known class of metal-binding structure because of similarity to porphyrins [127, 147]. The mimics become the primary target for extensive research because various pathological conditions, such as, diabetes excessive inflammatory responses, neurodegenerative diseases, cardiovascular conditions, and cancer [148, 149], are widely associated with an increase in oxidative stress, e.g. the imbalanced production of reactive species [150, 151].

Turnover number (TON) is the maximum number molecules of the substrate that can be converted into product per catalytic site of a given catalyst under defined conditions. Turnover frequency (TOF) is the measure of the specific activity of a catalytic centre of a given catalyst by the number of molecular reactions or catalytic cycles occurring at the centre per unit time. Kozuch and Martin tried to clarify these concepts, which are commonly used in catalytic studies. Despite its utility and common use, the TOF concept is still not well-defined. The concept of TOF is focused on kinetic information about the catalytic reactions while, TON depicts stoichiometric information [184].

2.17 Flavanone oxidase model

Flavanones, a type of flavonoids, which are found in citrus fruits render many beneficial pharmacologic properties such as, antioxidant, anti-inflammatory, anticarcinogenic, antibacterial, antiviral and antifungal. Oxidation of flavones was explained as a two-electron process coupled with two-proton transfer and fast hydroxylation caused by traces of water. Many studies reported the oxidation of flavanones to flavones by using stoichiometric reagents, such as, manganese acetate and Fe^{II}(asN4Py) [152]. Non-radical C-H oxidations with hydrogen peroxide in the presence of non-porphyrinic Mn catalysts have been rarely reported in the literature [153, 154]. Costas with his coworkers presented that complex [(HMePytacn)-$Mn(CF_3SO_3)_2$] carried out eight catalytic turnovers in the oxidation of cis-1,2-dimethylcyclohexane [154]. The oxidation of aliphatic C-H groups with hydrogen peroxide is professionally catalyzed by aminopyridine manganese complexes in the acetic acid medium. All these catalysts demonstrate unprecedented high selectivity and stereospecificity, indicative of a non-radical oxidation mechanism.

2.18 The bleaching test of the manganese-isoindoline complexes

Bleaching processes have been extensively studied in the textile industry and the oldest bleaching procedures for laundry cleaning utilize hydrogen peroxide at high temperatures. Researchers investigated several catalysts to attain bleaching at low temperatures, such as, 40-60 °C under conditions [155].

The well-known example of manganese complexes derived from 1,4,7-trimethyl-1,4,7-triazacyclo-nonane ligands was comprehensively studied by Unilever research as bleaching catalysts for stain removal at room temperature [156]. The Mn-tmtacn lab-scale textile damage was observed and the detergents were later withdrawn from the market [157]. Based on bleaching catalyst, hydrogen peroxide could play a major role in the pulp and paper production, wastewater treatment, laundry for industrial and domestic applications. Oxidation reactions have a significant role in the chemical industry. Hydrogen peroxide is used as an effective oxidant. Recurrently, bleaching developments are carried out through oxidative mechanisms by the degradation of chromophores into the water soluble products. So far, several novel transition metal complexes of terpyridine-type, saltren, salen, ligands and triazole derivatives possessing the significant potential for the activation of hydrogen peroxide have been synthesized as bleaching catalysts and established. These results encouraged us to progress new transition-metal catalyst applicants containing phthalocyanine molecules for laundry bleaching applications [151].

2.19 Catalytic oxidation of *N,N*-dimethylanilines

N-Alkyl functions are used in a variety of drug molecules, usually in saturated cyclic structures or alkylamine chains. In the design of a new drug, it is often required to remove the *N*-alkyl function from the parent drug to form the nor-intermediate and replace it with different *N*-substituents. Heme and non-heme enzymes *N*-dealkylation reactions play significant roles in several biological processes from DNA repair to the detoxification and metabolism of a variety of xenobiotics, for example, tertiary amine-containing drugs [158].

The complex 1-methyl-4phenyl-1,2,3,6-tetrahydropyridine (MPTP) is a neurotoxic byproduct of the heroin synthesis, which is capable to induce a Parkinson's disease in humans. Its detoxification by P450s can safeguard neurons within the central nervous system (CNS) in humans as well as animals [159].

The mechanism of these key processes has been widely studied but it is still hidden, whether the oxoiron-mediated *N*-dealkylations advance through a C-H abstraction mechanism [160]. In the case of horseradish peroxidase (HRP) the formation of ammonium radicals (EPR) during the oxidation process can be discussed by the participation of the rate-determining electron-transfer before the α-hydroxylation step [159]. Though direct hydrogen atom transfer (HAT) has been proposed for cytochrome P450, 2-Oxoglutarate/Fe(II)-dependent dioxygenases are also recognized to catalyze *N*-demethylation reactions. For example, AlkB-type proteins catalyse the elimination of *N*-linked methyl groups at positions 1 and 3 of purine and pyrimidine bases, respectively, in DNA and RNA [161].

As a functional model for the iron-containing proteins, numerous catalytic systems have been inspected for *N*,*N*-dimethylaniline (DMA) derivatives. Iron(II, III)-2,2'-bipyridine and iron(III)-porphyrin complexes, where the product mechanism and composition were significantly influenced by the nature of the utilized iron catalyst, although the active species in each case is uncertain [162]. It is important to discuss the *N*-methylformanilide which is the main intermediate in organic synthesis, also it is extensively used in the Vilsmeier-Haack reaction [163]

3 Aim of the work

- Investigation of reactivities of the non-heme iron and manganese catalysts in oxygen atom transfer and hydrogen atom transfer reactions
- Synthesis and characterization of manganese-isoindoline complexes and investigations of catalytic activities
- The bleaching performances of the Mn^{II} complexes by the degradation of morin
- The catalase-like activities for manganese-isoindoline complexes in aqueous solutions
- The catalytic dealkylation of *N*,*N*-methylaniline by $[Mn^{II}(asN4Py)]^{2+}$

4 Result and discussion

4.1 Reactions of iron(IV)-oxo intermediates

High-valent iron(IV)-oxo species have a key role in the catalytic cycle of mononuclear non-heme iron enzymes such as, Rieske dioxygenases that are capable of a wide range of synthetically difficult oxidations, for instance, epoxidation and C-H oxidation. Que with his co-workers presented a mechanistic proposal for the (N4Py)Fe^{III}OOH mediated epoxidation of alkenes, depending on the oxidizing power of pentadentate ligated hydroperoxy compounds with *cis*-labile sites on the iron, and the centre has been confirmed to be more capable in electrophilic epoxidation [164, 165].

Banse described that iron(IV)-oxo complex having the pentadentate ligand, *N*-methyl-*N*,*N*,*N*-tris(2-pyridylmethyl)propane-1,3-diamine, reveals incredibly selective in the epoxidation of cis-stilbene and cyclooctene in less than 20 % yield. Rybak-Akimova observed that S = 1 [Fe^{IV}(PyMAC)(O)(ClO_4)$_2$], *cis*-cyclooctene oxidation to epoxide with second-order k_2 = 0.17 M^{-1} s^{-1} at 0 °C, in 80 % yield [164]. Significantly higher reactivity (3.3 M^{-1} s^{-1} at -40 °C) of the S = 2 complex [Fe^{IV}(TQA)(O)(OTf)$_2$] was revealed toward *cis*-cyclooctene [87]. In addition, it was also observed, that [Fe^{IV}(N3S2)(O)(ClO_4)$_2$] is able to epoxidize styrene via an electrophilic oxidation mechanism with k_2 = 0.03 M^{-1} s^{-1} at 25 °C, in about 60 % yield [86]. Reactive and well-characterized chiral terminal oxo-metal complexes capable to go through oxygen-atom transfer reactions to styrene in an enantioselective manner are also rarely reported in the literature [90, 166].

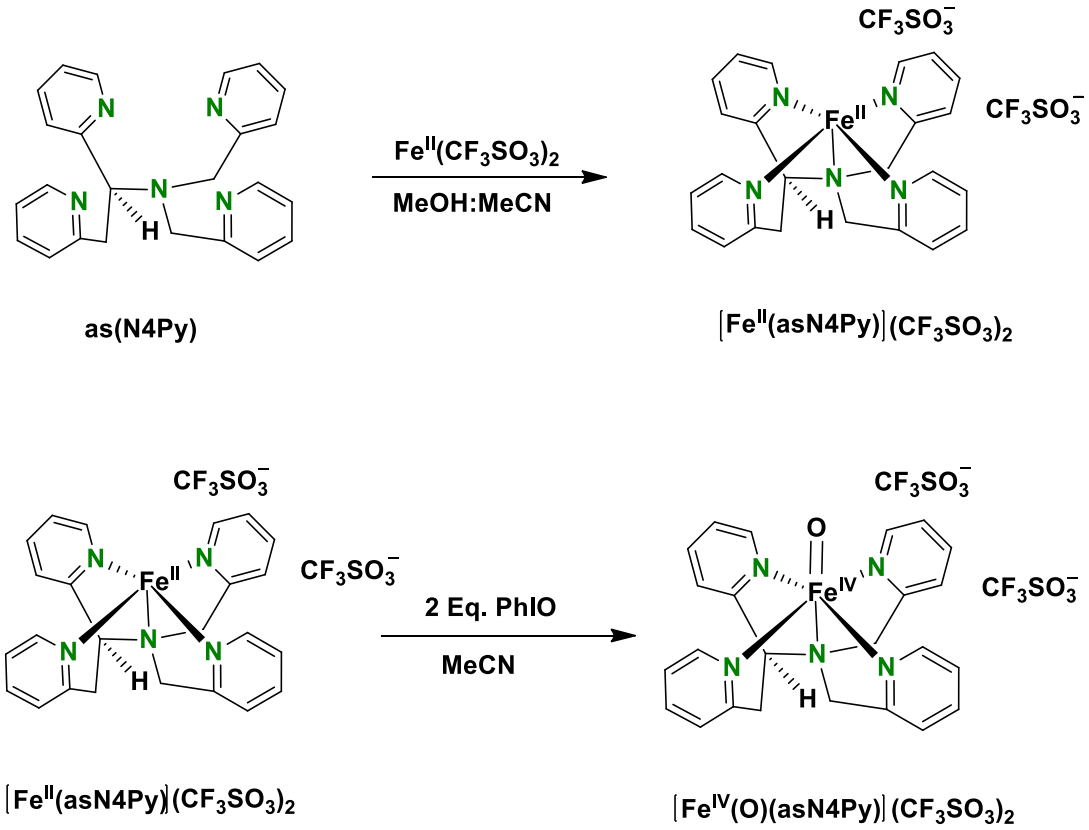

Scheme 5. Generation of the $[Fe^{IV}(O)(asN4Py)]^{2+}$ from the precursor Fe^{II} complex

Due to the highly stable iron(IV)-oxo species $[Fe^{IV}(asN4Py)(O)]^{2+}$ **(1b)** with a half-life ($t_{1/2}$) of 10 days in acetonitrile (CH_3CN) at room temperature, it is suitable to deeply investigate the mechanism of the iron(IV)-oxo mediated epoxidation. In addition, the reactivity of independently generated iron(IV)-oxo species with olefins was studied experimentally. Complex **(1b)** was generated by the reaction of $[Fe^{II}(asN4Py)](CF_3SO_3)_2$ **(1a)** with 2 eqv., of PhIO for about 40 min (Scheme 5), and the rate of its rapid breakdown at 705 nm (Figure 9), was measured as a function of the concentration of added olefins, and no shifts have been observed for the olefins.

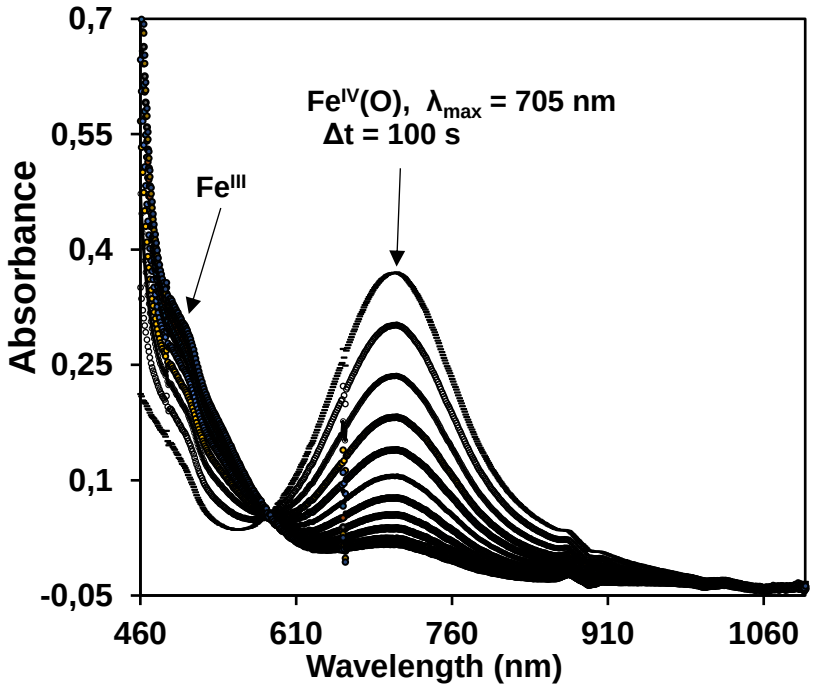

Figure 9. UV-vis spectral changes of $[[Fe^{IV}(asN4Py)(O)]^{2+}]_0 = 1.5\times10^{-3}$ M, upon addition of $[styrene]_0 = 0.3$ M in CH_3CN at 298 K

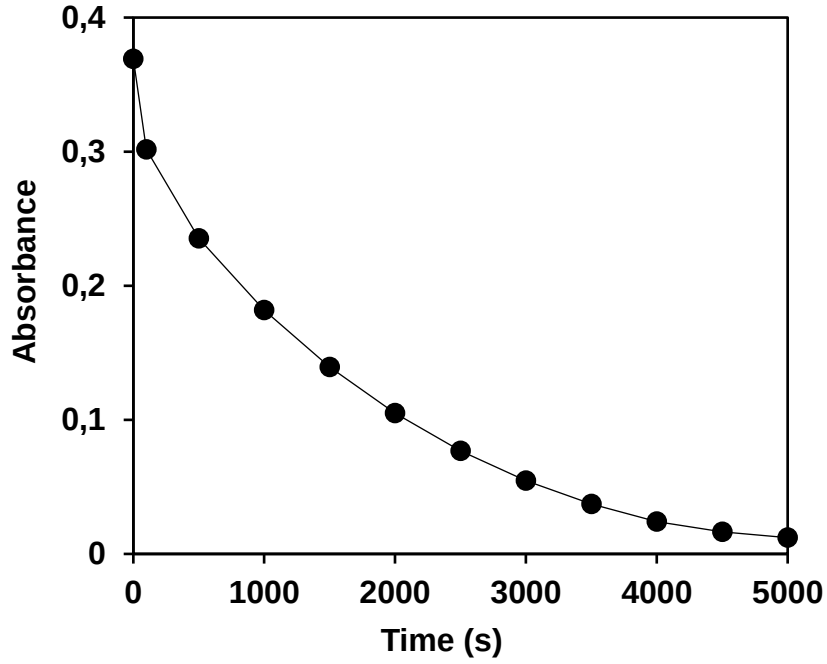

Figure 10. The decay of **(1b)** monitored at 705 nm. $[[Fe^{IV}(asN4Py)(O)]^{2+}]_0 = 1.5\times10^{-3}$ M, $[styrene]_0 = 0.3$ M in CH_3CN at 298 K

Table 11. Intermediates of complexes $[Fe^{IV}(N4Py)(O)]^{2+}$and $[Fe^{IV}(asN4Py)(O)]^{2+}$

[Comp.]	λ_{max} (nm)	ε ($dm^3\,mol^{-1}\,cm^{-1}$)	T(K)	$t_{1/2}$(h)	Ref.
$[Fe^{IV}(N4Py)(O)]^{2+}$	695	400	298	60	[167]
$[Fe^{IV}(asN4Py)(O)]^{2+}$	705	400	298	233	[167]

The oxoiron(IV) complex (**1b**) reacts with the C=C bonds of a number of substrates such as, cis-cyclooctene and substituted styrene derivatives at room temperature to give epoxides as the main products, with carbonyl compounds. The addition of 200 eqv. of cis-cyclooctene to (**1b**) resulted in the quick decomposition of (**1a**) to its Fe(II) precursor species as confirmed by UV-vis spectroscopy at the λ_{max} = 409 nm, the oxidation of styrene yielded 65% epoxide and 12% benzaldehyde, and cis-cyclooctene oxidation produced 75% cyclooctene oxide and 7% cyclooct-2-enone. (Scheme 6).

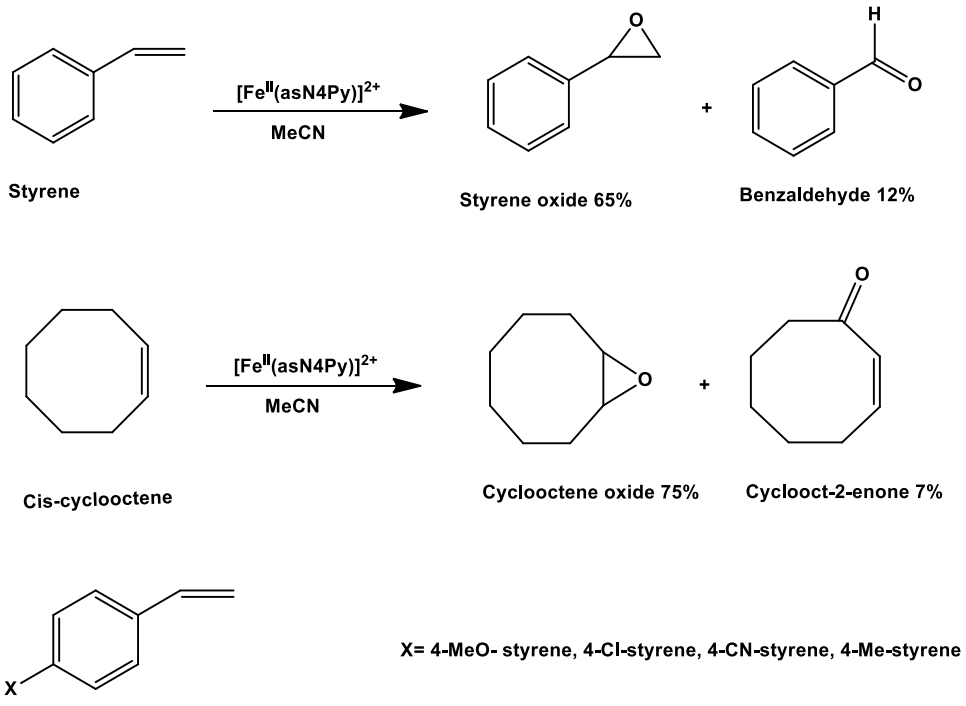

Scheme 6. Oxidation reactions of olefins by non-heme $[[Fe^{II}(asN4Py)]^{2+}]_0$ = 1.5×10^{-3} M

The rates in the presence of excess *cis*-cyclooctene (200-1000 eqv.) followed pseudo-first-order kinetics -d[**1b**]/dt = k_{obs} [**1b**], where $k_{obs} = k_{dec} + k_2$ [S] and $k_{dec} < k_2$ [S]). The deduction from the absence of saturation kinetics (Michaelis-Menten kinetics) under this condition is that the substrate does not or only weakly binds to the oxidant prior to the rate-controlling step. This plot shows the second-order rate constant k_2 to be 5.41×10^{-4} M^{-1} s^{-1} at 298 K (Table S1, Figure 11), which is much smaller than those achieved for the epoxidation of *cis*-cyclooctene by $[Fe^{IV}(PyMac)(O)]^{2+}$ and $[Fe^{IV}(TQA)(O)]^{2+}$ complexes (0.45 at 0 °C and 3.3 M^{-1} s^{-1} at -40 °C, respectively) (Table 6).

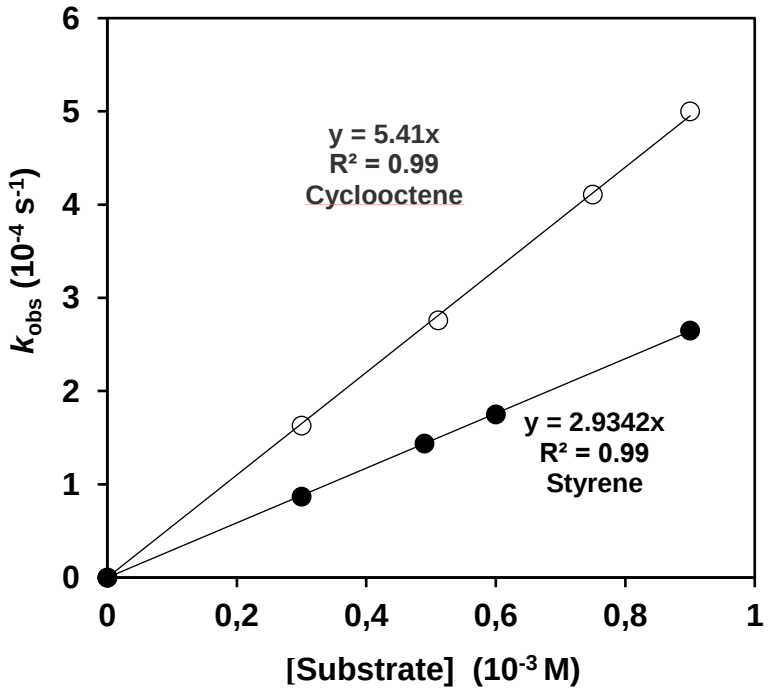

Figure 11. Reaction rate of $[[Fe^{IV}(asN4Py)(O)]^{2+}]_0 = 1.5\times10^{-3}$ M with *cis*-cyclooctene (O) and styrene (●) in CH_3CN at 298 K

At constant styrene and cyclooctene concentrations, the k_{obs} values were shown to be independent of the initial concentration of the iron(IV)-oxo species which is obvious from the linear log[**1b**] versus time. The linear plot of the reaction rate values ($V_i = k_{obs}$ [**1b**]) versus the initial concentration of **(1b)** states that the reaction is first-order with respect to the iron(IV)-oxo concentration directly proportional to the concentration of the reactant, (Table S4, Figure 12). The above results found a rate law of -d[**1b**]/dt = k_2[**1b**][alkene] for both substrates.

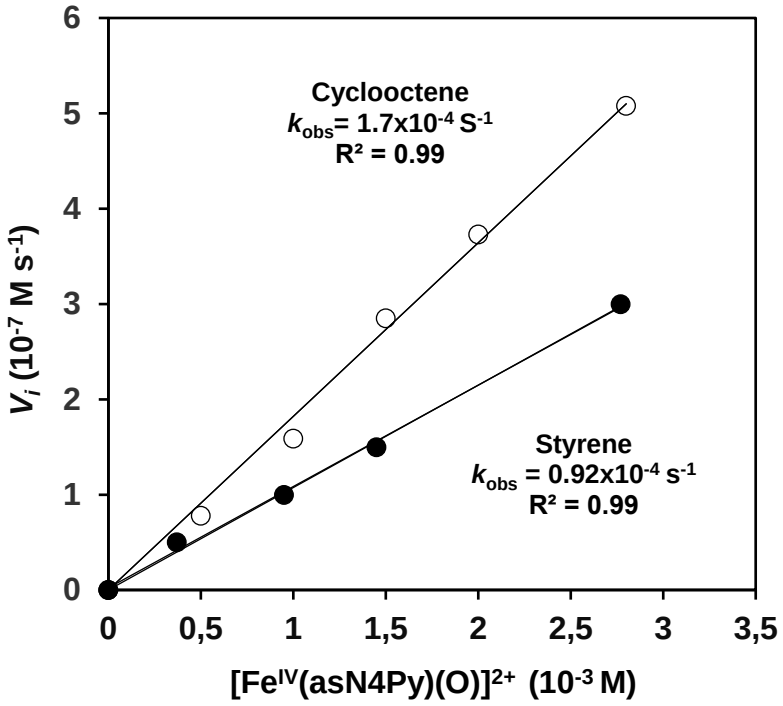

Figure 12. Plot of *V*i versus $[[Fe^{IV}(asN4Py)(O)]^{2+}]_0 = 1.5\times10^{-3}$ M, for reactions of (0.3 M) *cis*-cyclooctene (O) and styrene (●) in CH_3CN at 298 K

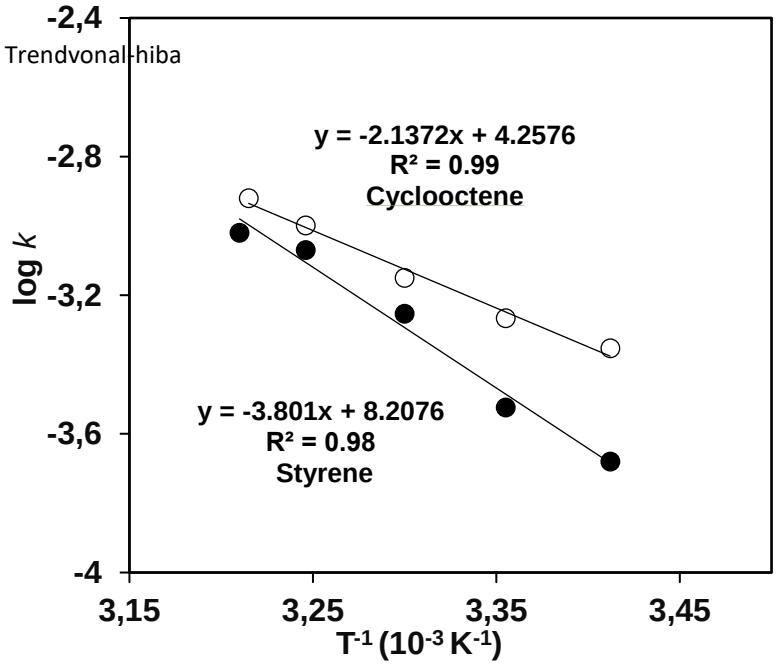

Figure 13. Arrhenius plot of the reaction of $[[Fe^{IV}(asN4Py)(O)]^{2+}]_0 = 1.5\times10^{-3}$ M, $[cyclooctene]_0 = 7.5\times10^{-1}$ M, $[styrene]_0 = 1.5$ M in CH_3CN at 298 - 311 K, (Table S3)

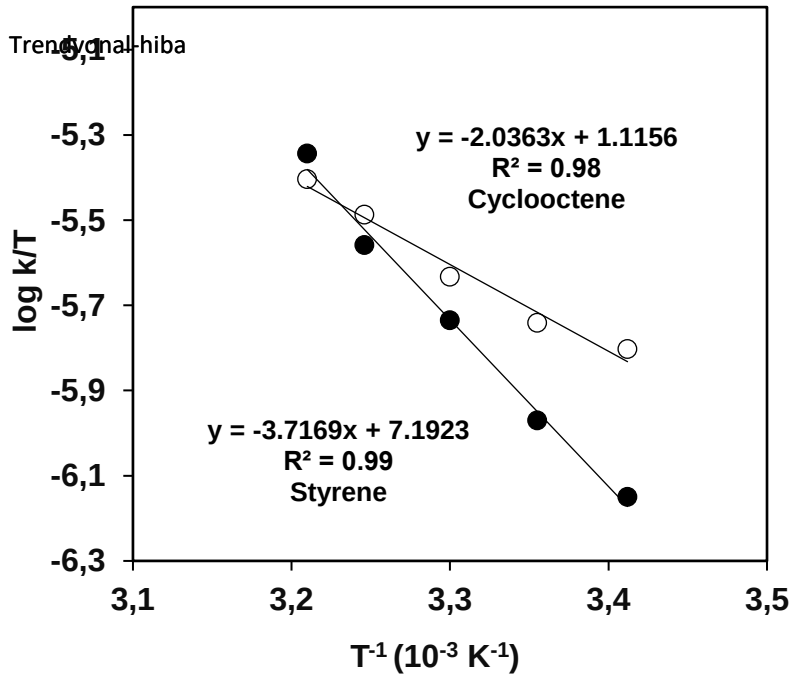

Figure 14. Eyring plot of the reaction $[[Fe^{IV}(asN4Py)(O)]^{2+}]_0 = 1.5\times10^{-3}$ M, with cyclooctene (o) and styrene (●) (Table S3)

Table 12. The calculated *E*A, *ΔH* and *ΔS* values in the reaction of $[Fe^{IV}(asN4Py)(O)]^{2+}$ with cyclooctene and styrene in MeCN

S	E_A ***(kJ×mol^{-1})***	$\Delta H^{\neq}$ ***(kJ×mol^{-1})***	$\Delta S^{\neq}$ ***(J×mol^{-1}×K^{-1})***
Cyclooctene	40.45	38.35	-180.21
Styrene	72.7	71.0	-76.41

Activation parameters of ΔH = 38 kJ mol^{-1}, ΔS = -180 J mol^{-1} K^{-1} at 298 K, and ΔH = 70.6 kJ mol^{-1}, ΔS = -76 J mol^{-1} K^{-1} at 298 K, these values were calculated from the plot of log(k_2/T) against 1/T in CH_3CN over the temperature range 293 to 313 K for the *cis*-cyclooctene and styrene oxidation, respectively.

The activation enthalpy of 71 kJ mol^{-1} for the $[Fe^{IV}(asN4Py)(O)]^{2+}$ mediated epoxidation of styrene is roughly the same with that presented for $[Fe^{IV}(N3S2)(O)]^{2+}$. Linear correlation between the relative rate and the total substituted effect (TE) for the iron(IV)-oxo mediated oxidation of *p*-substituted styrenes is established (Figure 15).

$$E_A = 2.303 \times R \times \mathbf{dlog}(k)/\mathbf{d}(T^{-1}) \qquad \text{Eq. 3}$$

E_A Cycloocten = 2.303 × 8.314 × 2.113 = 40.45 kJ×mol^{-1}

E_A Styrene = 2.303 × 8.314 × 3.801 = 72.7 kJ×mol^{-1}

$$\Delta H^{\neq} = 2.303\ R \times \mathbf{dlog}(kT^{-1})/\mathbf{d}(T^{-1}) \qquad \text{Eq. 4}$$

$\Delta H^{\neq}$ Cycloocten = 2.303 × 8.314 × 2.013 = 38.35 kJ×mol^{-1}

$\Delta H^{\neq}$ Styrene = 2.303 × 8.314 × 3.71 = 71 kJ×mol^{-1}

The calculated spin density variations at the benzylic radical centres correlate well with both the hyperfine coupling constants (ESR) determined by Arnold *et al*. and the calculated radical effects of the substituents. It has been suggested that in the absence of sizable steric interactions, both polar parameters and radical stabilization parameters are needed for the description of the substituent effect on carbon radical systems [185].

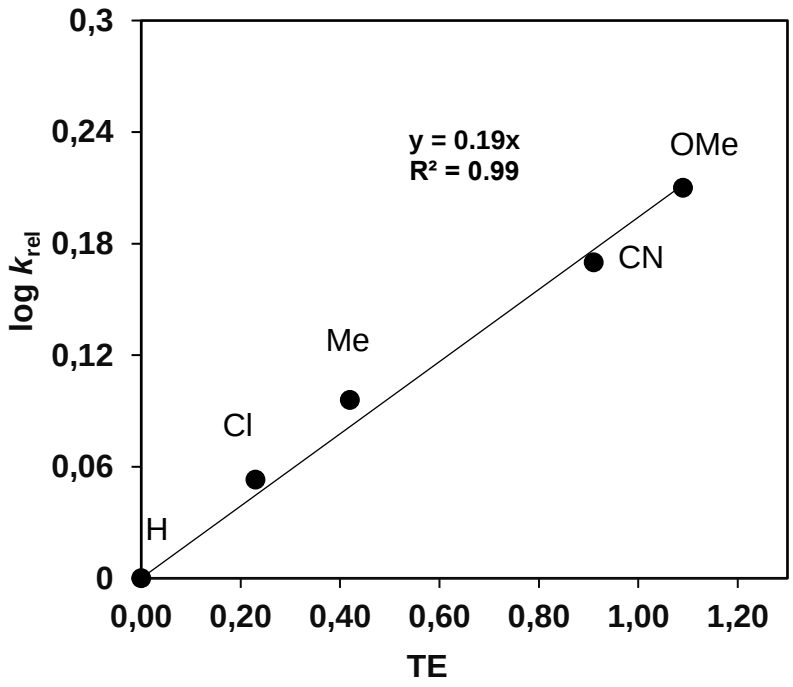

Figure 15. Hammett plot of log k_{rel} against TE of *p*-substituted styrene

Competitive reactions were performed with *p*-substituted styrene derivatives in order to calculate the effect of electronic factors on the reaction. Since, both electron-withdrawing (-Cl, -CN) and electron-releasing (-OMe, -Me) substituents can speed up the reaction. The linear free-energy connection between the second-order rate constants for the *p*-substituted styrene oxidations and the total substituent effect (TE), stabilities of the benzylic radicals including spin delocalization and polar effects [168] parameters has been established: ρ_{TE} = +0.19. A comparison of this correlation for the corresponding ruthenium(IV)-oxo mediated epoxidation reactions have discovered that the oxidation of aromatic alkenes mediated by **(1b)** proceeds via the rate-limiting formation of a benzylic radical intermediate (C in Scheme 8), the correlation of the relative reactivity (log k_{rel}) on the substituent constants (σ_p) of *p*-substituted styrene is non-linear, gives rise to concave Hammett curve (Table S5, Figure 16).

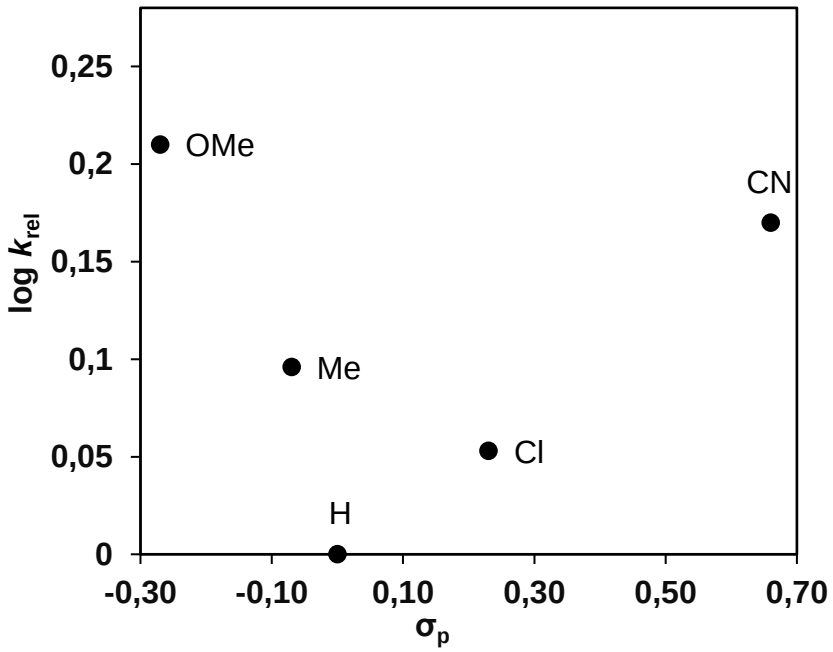

Figure 16. Plot of log (k_{rel}) against σ_p of *p*-substituted styrene

Table 13. Reactions of *p*-substituted styrene derivatives

styrene	k_{obs} (10^{-4} s^{-1})	S [M]	k_2(10^{-4} M^{-1} s^{-1})	σ constants	k_{rel}	log k_{rel}
-OMe	1.43	0.3	4.76	0.27	1.64	0.21
-H	0.87	0.3	2.9	0	1	0
-4-Cl	0.948	0.3	3.16	0.23	1.13	0.053
-4-CN	1.31	0.3	3.46	0.66	1.48	0.17

Four alternative mechanisms including four possible intermediates can be proposed for the epoxidation of alkenes by oxometal complexes, namely two concerted via [2+1] oxene insertion (A in Scheme 7) or [2+2] metallaoxetane formation (B in Scheme 7), and two nonconcerted via an alkene-derived benzylic radical (C in Scheme 7) or a carbocation intermediates (D in Scheme 7).

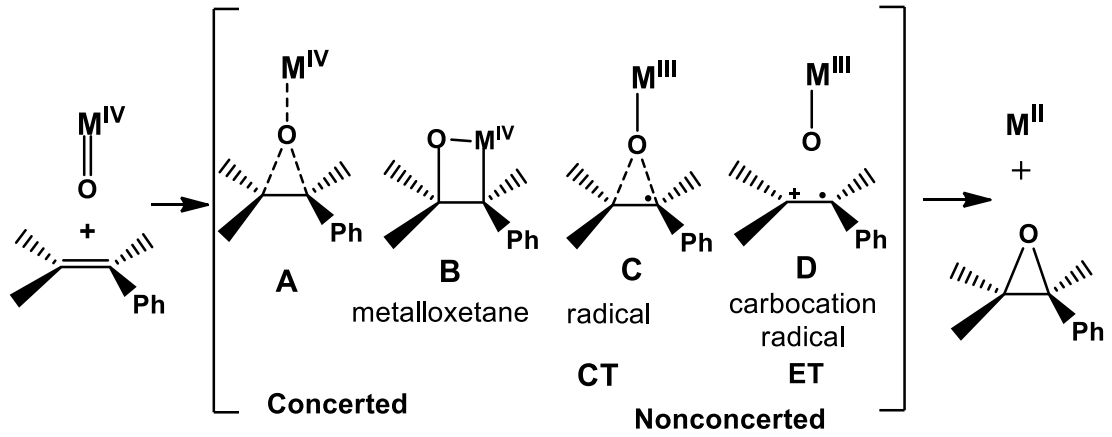

Scheme 7. Proposed mechanism of styrene oxidation by iron(IV)-oxo species

There are several studies that support the radical mechanism. The insensitivity of the k_2 values to the *p*-substituent effect and the concave-type Hammett curve can be assigned to the rate-limiting formation of a benzylic radical species. If the carbocation ion is supposed as an intermediate, a more negative value would be expected (-3.5) in the electrophilic process [168-170].

In addition, benzaldehyde formation can also be described by the reaction of the forming carboradical species with the oxidation of aromatic alkenes mediated by **(1b)** proceeds via the rate-limiting formation of a benzylic radical intermediate (C in Scheme 7) through rapid and reversible charge-transfer (CT) complex formation in a non-concerted process. The forming carboradical then can undergo ring closure to produce epoxide.

Stoichiometric oxidation of 4-chlorostyrene and styrene by (-)-Fe^{IV}(asN4Py)(O)]$^{2+}$ (-)-(**2b**) gave a 12 % of 4-chlorostyrene oxide and 8 % enantiomeric excess of styrene oxide (Table 14), even though the asymmetric induction is not impressive when compared with other published studies [171]. Because of the selectivity loss, the concerted [2+1] and [2+2] cycloaddition mechanisms can be excluded (A and B in Scheme 7).

The moderate enantioselectivities for the oxidation of styrene derivatives (8-12 % ee) can be elucidated by the rotation/collapse processes through C-C bond of the radicalized species prior to the epoxide ring closure.

Table 14. Stoichiometric styrene oxidations by (-) $[Fe^{IV}(asN4Py)(O)]^{2+}$ complex.

No.	oxidant	substrate	ee (%)	yield (%) (epoxide/aldehyde)
1	(-)-**2b**	4-Cl-styrene	12 (R)	58/12
2	(-)-**2b**	4-H-styrene	8 (R)	52/14

In summary, the reaction of $[Fe^{IV}(asN4Py)(O)]^{2+}$ generated from iron(II) and PhIO, with cis-cyclooctene and styrene in MeCN shows first-order dependence on the concentration of the alkene and the oxidant. The higher reaction rate for cis-cyclooctene compared to styrenes can be explained by the two electron-donor alkyl groups in the cyclic alkene, and the stabilities of the benzylic radicals in the case of styrenes due to spin delocalization. A linear correlation between the relative rate and the TE for the iron(IV)-oxo mediated oxidation of p-substituted styrenes is established. A comparison of this correlation for the corresponding ruthenium(IV)-oxo mediated epoxidation reactions has revealed that the oxidation of aromatic alkenes mediated by **(1b)** proceeds via the rate-limiting formation of a benzylic radical intermediate in a nonconcerted process. The loss of stereospecificity (8-12 % ee) necessarily indicates the radicaloid character of the intermediate species formed during epoxidation, which allowed a limited amount of rotation through C-C bond prior to the epoxide formation.

4.2 Enantioselective C-H bond oxidation

The functionalization of nonactivated aliphatic C-H bonds is an incredibly dominant reaction due to its ability to convert these inert bonds, abundant in organic molecules, into functional groups fit for further chemical development. It constitutes one of the challenging reactions in the area of progressive synthetic organic chemistry due to the inert nature of the C-H bonds. The lack of reactivity derives from the fact that C and H atoms are held together by non-polarized, localized and strong bonds. Neither low-energy empty orbitals nor high-energy filled orbitals that could support a chemical reaction are available [98, 172].

Due to their inert character, the multitude of aliphatic C-H bonds in a molecule makes site-selective functionalization primarily difficult. These topics are more emphasized due to the high reactivity of the species capable of breaking these bonds is often incompatible with chemo- and site-selective transformations. A main group of reactions is represented by C-H bond oxidations that found oxidized functionality straight into aliphatic (sp^3) C-H bonds. The direct combination of an oxygenated functionality into a molecule is vigorous from a synthesis cost point of view, the transformation of these groups into the selection of functional groups can reveal advance and more competent synthetic pathways [173, 174]. Previously, it was reported by our research group that Fe(II) complexes with chiral pentadentate aminopyridine ligands can give relatively stable high valent iron(IV)-oxo species with different oxidants, for example, PhIO, *tert*-butyl hydroperoxide (TBHP), H_2O_2, and *meta*-chloro peroxybenzoic acid (*m*-CPBA), which are considered as potential candidates for stereoselective C-H oxidation reactions [102].

The catalytic activity including the enantioselective behaviour of enantiopure ligand containing $[Fe^{II}(asN4Py)(CH_3CN]^{2+}$ (-)-**(2b)** was investigated in the oxidation of ethylbenzene, using H_2O_2, *m*-CPBA, and TBHP as co-oxidants. In the absence of any metal catalyst, no oxidation products formation was observed.

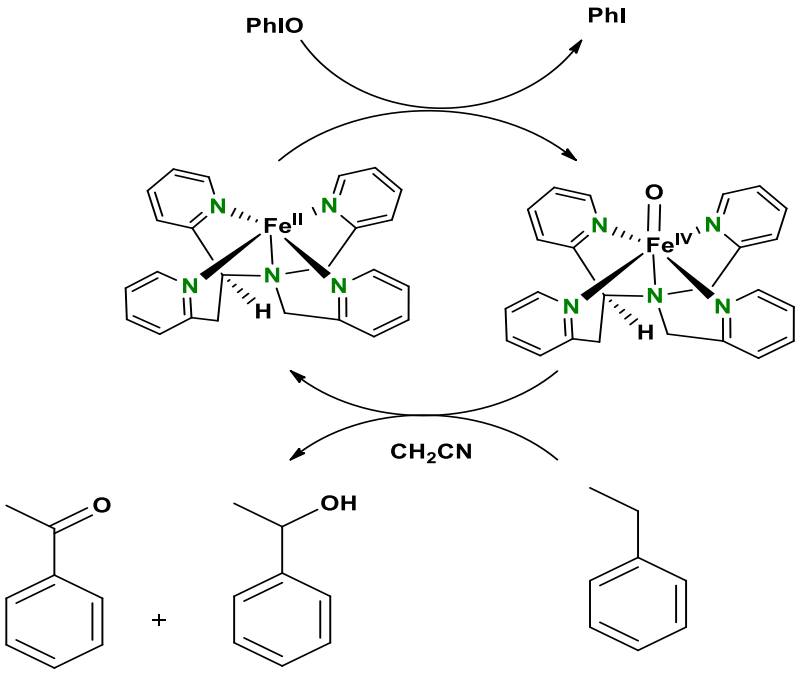

Scheme 8. Oxoiron(IV) mediated C-H oxidation in this study

Stoichiometric oxidation of ethylbenzene by [Fe^{IV}(asN4Py)(O)] (-)-(**2b**) in CH_3CN at 0 °C yielded 33 % enantiomeric excess (ee) of 1-phenylethanol after 90 minutes, and 25 % enantiomeric excess (ee) after 180 minutes under argon (Figure 17). Since the iron(IV)-oxo species was generated by PhIO in the presence of hydroxyl and *tert*-butoxy radicals and their non-selective reaction with the substrate in the stoichiometric reaction can be excluded. The moderate enantioselectivity and the lower enantiomeric excess value during the reaction can be explained by the epimerization of the long-lived substrate radical (rotation process through C-C bond of the radical species) before the rebound step (non-rebound mechanism, where $k_{ep} > k_{reb}$) [175]. Much lower value (14 % ee) was observed in the oxidation of methyl 1-tetralone-2-carboxylate.

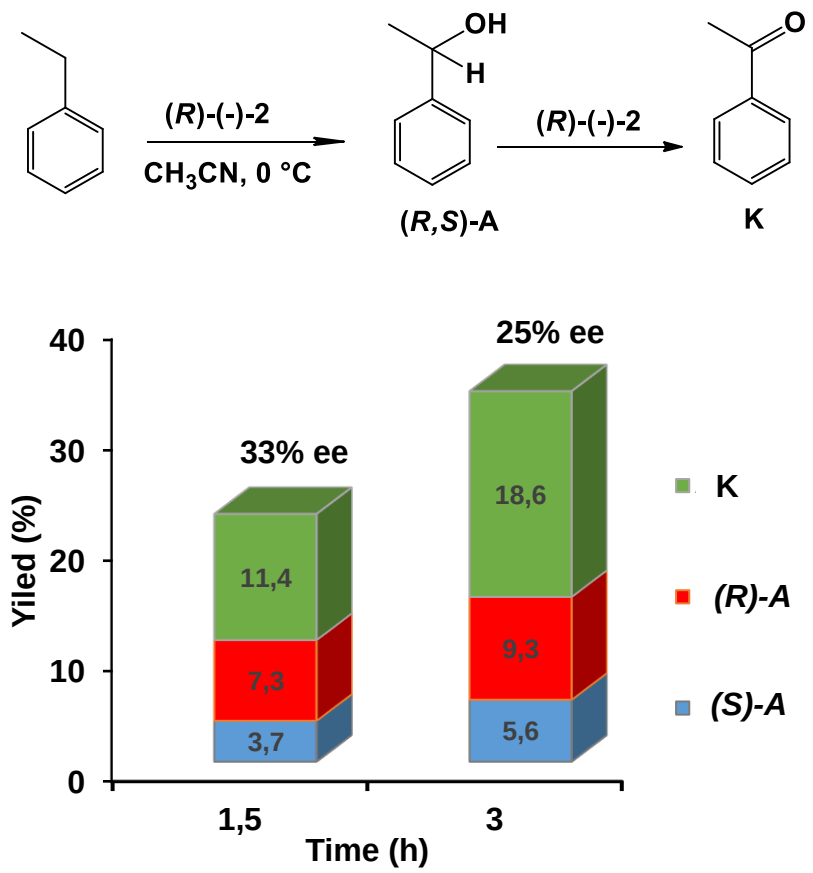

Figure 17. The yield of K/A ratio and the enantiomeric excess (ee) for the stoichiometric oxidation of ethylbenzene with (-)-(**2b**) in CH_3CN at 0 °C

Moderate yields and poor enantiomeric excess (ee), were expected for substrates with stronger C-H bonds, where the radical dissociation pathway can become prominent. The oxidation of ethylbenzene by the chiral iron(IV)-oxo intermediate achieves moderate enantioselectivities up to 33 % enantiomeric excess (ee), which can be explained by the epimerization of the long-lived substrate radical before the rebound step (non-rebound mechanism, where $k_{ep} > k_{reb}$). Much lower ee values (up to 14 %) have been observed for the catalytic oxidation of ethylbenzene, which can be explained by the parallel enantioselective metal-based, iron(IV)-oxo mediated and nonselective Fenton-type radical processes [176].

Efforts have been made to develop a highly efficient asymmetric catalyzed oxidation of strong C-H bond, mediated by chiral iron(IV)-oxo intermediate. Based on detailed mechanistic studies on stoichiometric benzyl alcohol (KIE of 31) and hydrocarbon (KIE of 38) oxidation that have been investigated with in situ generated high-valent iron(IV)-oxo complex, a plausible mechanism has been proposed for both systems, in which the oxidation of alcohols and hydrocarbons occurs in the same manner by HAT in the rate-determining step. Moderate yields and enantiomeric excess (ee), values can be expected for substrates with stronger C-H bonds, where the radical dissociation pathway can become prominent. In this study, we have also demonstrated that the enantioselectivity depends on the nature of the following step rebound versus non-rebound mechanisms (Scheme 9).

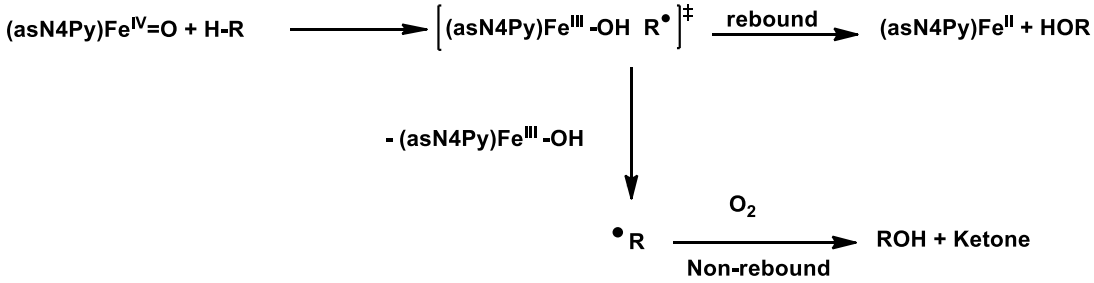

Scheme 9. Schematic illustration of possible mechanisms of the reaction pathways rebound versus non-rebound for $[Fe^{IV}(asN4Py)(O)]^{2+}$

In summary, efforts have been made to develop a highly efficient asymmetric catalyzed oxidation of various alkanes by introducing the chiral moiety to ligands as well as their detailed mechanistic aspects. Also demonstrated that the enantioselectivity depends on the nature of the following step rebound versus non-rebound mechanisms.

4.3 Catalytic reactivities of manganese-isoindoline complexes

The complexes of $[Mn^{II}(HL^3)(Cl)_2]$ (**3**), $[Mn^{II}(HL^4)(Cl)_2]$ (**4**), $[Mn^{II}(HL^5)(Cl)_2]$ (**5**), $[Mn^{II}(HL^6)(Cl)_2]$ (**6**), $[Mn^{II}(HL^7)(Cl)_2]$ (**7**) and $[Mn^{II}(HL^8)\text{-}(Cl)_2]$ (**8**), were synthesized and characterized by UV-Vis and FT-IR spectroscopy. A novel ligand such as 1,3-bis(2′-imidazolyl-imino)isoindoline (HL^5) and the complex were synthesized and characterized by using UV-Vis, FT-IR, NMR and CHN analysis. UV-Vis and FT-IR spectroscopy cannot provide detail information about complicated structures. However, for isoindoline complexes, some characteristics make their identification simple. The H is responsible for the anionic character, is greatly movable due to the aromaticity its possible positions are on one of the endocyclic amino group, or at the imino arms (Scheme 10).

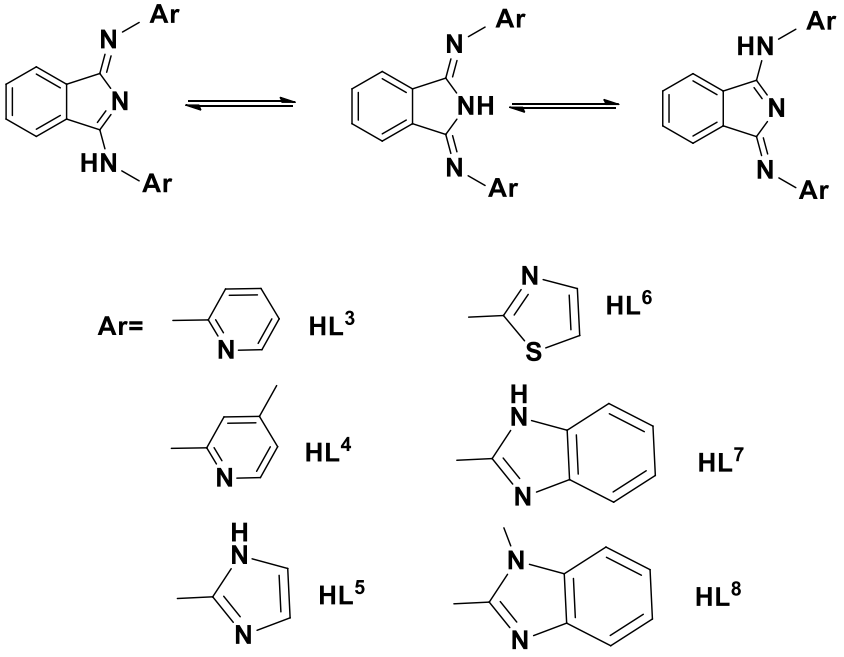

Scheme 10. Structure of the isoindoline-based on the ligands

In FT-IR spectra the nonspecific νC=N vibrations modes that are mostly influenced by this proton appear as two very strong bands in the 1600 cm^{-1} to 1660 cm^{-1} interval in the free ligands.

These bands are repressed if coordination happens by deprotonation. In this case, they shift below 1600 cm^{-1} losing intensity at the same time. In the case of non-deprotonated complexation, the strong vibrations above 1600 cm^{-1} remain visible and additionally other intense bands appear around 1550 cm^{-1}.

Table 15. UV-Vis spectroscopic data of isoindoline ligands and their complexes [124].

Ligands	π-π* bond of the free ligands λ_{max}/nm (log ε)	$[M(L)_2]$ λ_{max}/nm (log ε) in DMF Metal complexes	[M(L)] λ_{max}/nm (log ε) in DMF Metal complexes
HL^4	366 (4.24), 385 (4.29), 408 (4.11)	306 (4.53), 332 (4.45), 423 (4.73), 450 (4.65),	330 (4.19), 347 (4.21), 367 (4.28), 386 (4.37), 409 (4.14), 453 (3.32)
HL^6	374 (3.94), 396 (4.01), 420 (4.05), 448 (3.86), 485 (3.18)	348 (4.31) 360 (4.32), 432 (4.50), 454 (4.59) 448 (4.42)	373 (4.29), 396 (4.39), 419 (4.44), 448 (4.22)
HL^8	348 (4.33), 373 (4.39), 393 (4.38), 420 (4.33), 447 (4.35), 478 (4.11),	358 (4.54), 447 (4.59), 474 (4.65), 508 (4.47)	362 (3.94), 371 (4.02), 382 (4.00), 420 (3.91), 448 (3.94), 482 (3.75), 535 (2.93).

The electronic absorption spectrum of the ligands shows a multiple band pattern, the two imino moieties on the isoindole core have a strong impact on the planar structure of both ligands and its coordination complexes. The double bond between N and C atoms extends aromaticity and increases the rigidity of the system. The π-π* transitions are created by the extended π-bond system and they appear in the 360-500 nm region. Upon complex formation small (2-20 nm) red or blue shifts are observed. Lower energy bands are contributed to charge transfer transitions from metal ion to the ligand. The second key structural element is the endocyclic NH group. It is responsible for an anionic character observed with metal ions.

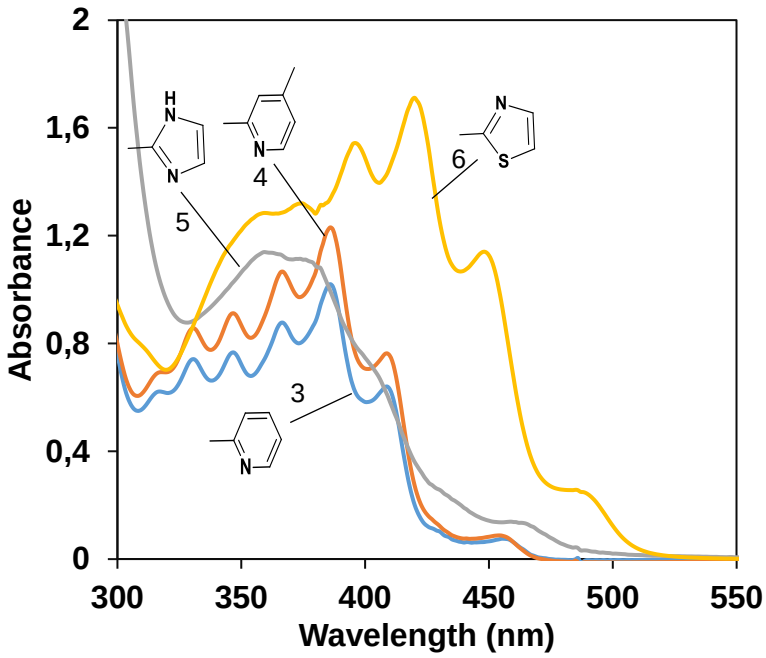

Figure 18. Electronic spectra of $[Mn^{II}(HL^{n})Cl_2]$ (HL = 1,3-bis(2'-Ar-imino)-isoindoline) complexes in DMF solution with nonannulated (Ar = pyridyl (n = 3), 4-methylpyridyl (n =4), imidazolyl (n = 5), thiazolyl (n = 6)), aromatic side chains

The electronic absorption spectrum of the manganese-isoindoline complexes (**3-8**), maximum absorption in the UV-vis spectra of $[Mn^{II}(HL^{3-8})Cl_2]$ that are found between 350 and 500 nm can be assigned to the π-π* transitions of the coordinated neutral ligands, except for the lowest energy bands in the range of 450-600 nm, which can be attributed to charge transfer transitions from the manganese(II) ion to a ligand π* orbital (LUMO, MLCT) (Figure 18). Deprotonation of the NH group of the isoindoline moiety could be reduced the difference in energy between occupied and unoccupied π-molecular orbitals of the ligand resulting in a redshift of π-π* transitions. In the absence of the significant (>40 nm), a bathochromic shift in the three lowest energy bands the anionic binding of the ligands can be excluded in all cases [3].

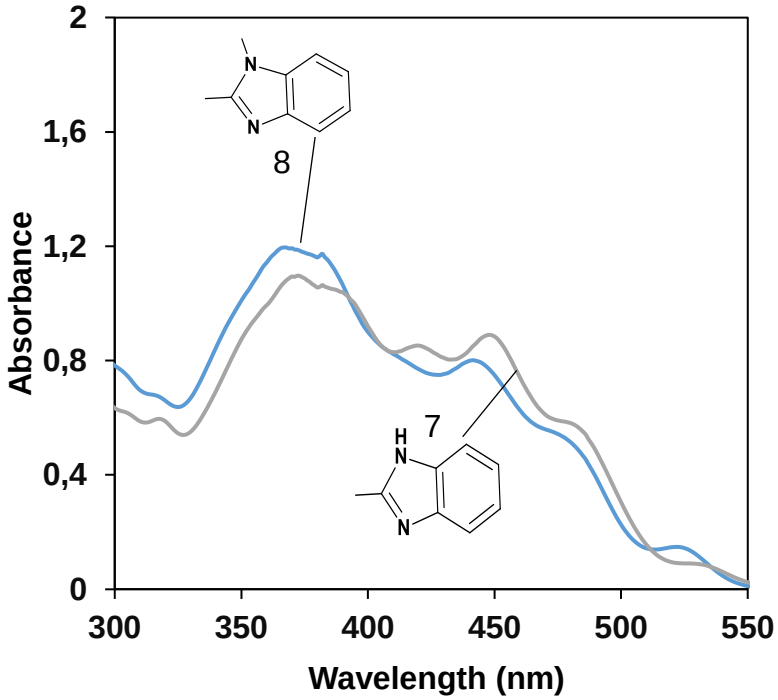

Figure 19. UV-Visible spectra for the manganese-isoindoline complexes (7-8)

The manganese(II) ion is bound to a neutral tridentate isoindoline ligand and two chloride anions, forming a distorted trigonal bipyramidal environment around the metal ion. Analytical data, the infrared and the electronic spectrum of the complexes are all consistent with the presence of a neutral nondeprotonated isoindoline ligand. Manganese complexes were dominated by the π-π* transitions of the neutral ligand indH. Deprotonation of the pyrrole nitrogen could be reduced the difference in energy between occupied and unoccupied π-MOs of the ligand and resulted in a redshift of π-π* transitions.

4.4 Electrochemistry

Electrochemical properties of the complexes **(3-8)** were obtained by taking cyclic voltammograms in *N*,*N*-dimethylformamide (DMF) solutions, using 0.1 M TBAP as supporting electrolyte under atmospheric conditions, between potentials 0.1 and 0.526 V vs. the Ag/AgCl reference electrode. All compounds show a reversible, one-electron redox wave in the plotted potential range (Figure 22), that is attributed to their Mn(III)/Mn(II) redox transition.

The $E°'_{1/2}$ against SCE were very similar to those reported. The [$\Delta E°_p = E°_{pa} - E°_{pc}$] the reduction of the Mn^{III} centre may induce chemical or stereochemical changes in the complex. This may be attributed to chloride exchange to solvent or the formation of an unsaturated coordination sphere due to the higher lability of the Mn^{II} species. Such phenomenon was reported earlier for chloride complexes of Mn^{III} bearing tridentate ligands [38]. Manganese complexes also show one quasi-reversible transition, but at significantly higher potential (Table 16).

Table 16. Redox potentials, E^o_{pa} and E^o_{pc} values of the manganese-isoindoline complexes

Catalyst	$E°_{pa}$ (mV)	$E°_{pc}$ (mV)	$E°_{1/2\ Mn^{III}/Mn^{II}}$ (mV)	Yield %	V_0 (10^{-3} Ms^{-1})	TOF (h^{-1} 10^3)
$[Mn^{II}(HL^3)Cl_2]$ (3)	977	866	921.5	32.6	0.569	19.41
$[Mn^{II}(HL^4)Cl_2]$ (4)	1026	870	948	36.6	0.682	23.27
$[Mn^{II}(HL^5)Cl_2]$ (5)	816	685	750	27.1	0.405	13.82
$[Mn^{II}(HL^6)Cl_2]$ (6)	625	576	600.5	21.8	0.352	12.01
$[Mn^{II}(HL^7)Cl_2]$ (7)	421	354	387.5	16.9	0.187	6.38
$[Mn^{II}(HL^8)Cl_2]$ (8)	455	395	425	15.13	0.204	6.96

The redox potentials listed in (Table 16) are comparable to other manganese complexes found in the literature [177], but they are significantly higher than those reported for cationic species [33]. This is an electrostatic effect that dominantly determines the redox potential for the metal centre through the overall charge of the complex molecule. The $E_{1/2}$ spans a 561 mV range from 388 mV (Ar = benzymidazolyl) to 948 mV (Ar = 4-methylpyridyl) vs. the SCE. Much narrower range (400 to 600 mV versus SCE) with lower potentials was observed for the recently studied $Mn^{II}(L)_2$ complexes. The quasi-reversible transition of (3-8). It can be concluded that the annulation of the imidazolyl group results in a shift (~400 mV) in the Mn^{III}/Mn^{II} potentials and stabilizes both the reduced and oxidized forms of the transition (Figure 20).

The d^4 Mn(III) will favour a geometric distortion from the octahedral structure, therefore the redox potential and peak separation of the Mn(III)/Mn(II) couple can be altered by controlling the geometry around the metal centre. Differences in geometric distortions have some effect on the $E°_{1/2}$ values [$E°_{1/2} = (E°_{pa} + E°_{pc})/2$], but the major determinant of redox potentials remains the donor-strength of the ligands.

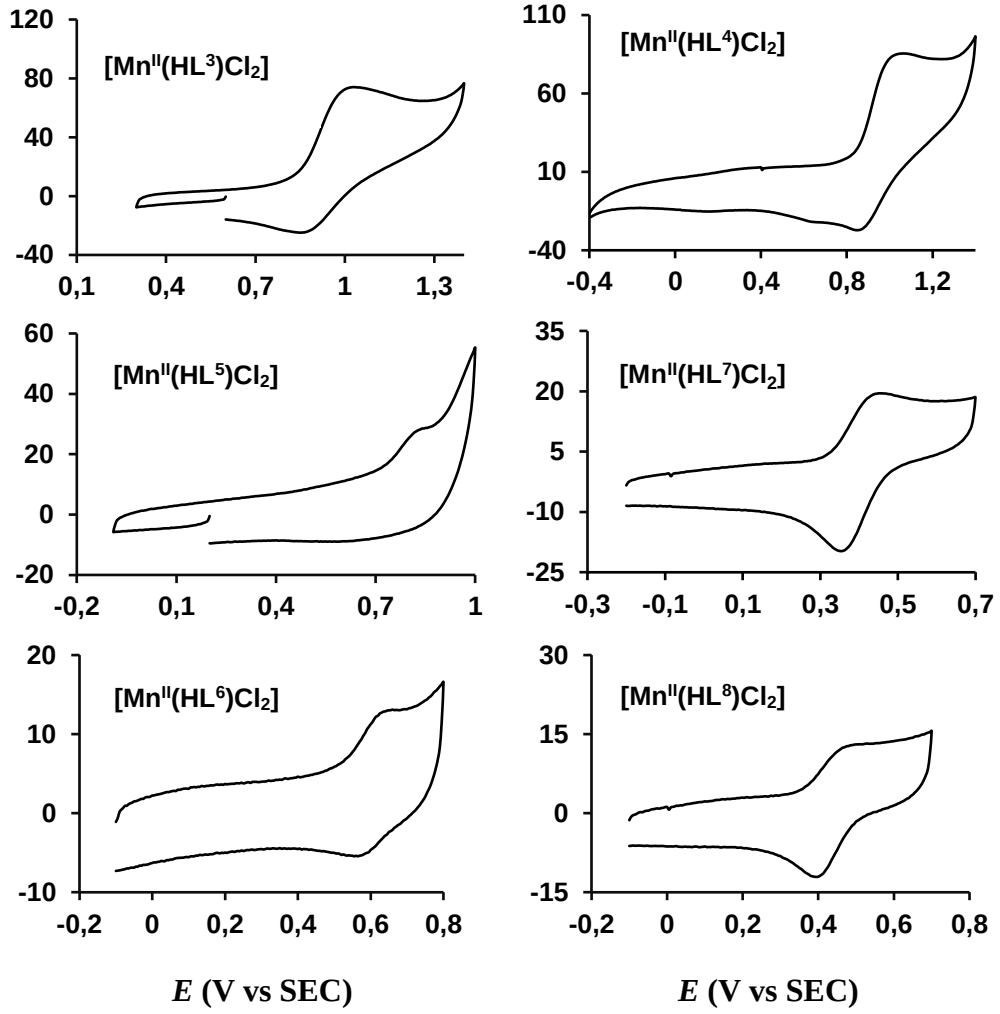

Figure 20. Cyclic voltammograms of 1mM $[Mn^{II}\{(Py)_2\text{-indH}\}(Cl)_2]$ derivatives in DMF with 0.1 M $(Bu_4N)ClO_4$; scan rate 100 mV^{s-1}, working electrode: glassy carbon electrode (GCE), auxiliary electrode: Pt wire, reference electrode: Ag/AgCl

Table 17. Electrochemical and spectroscopic data for $[Mn^{II}(HL^{3-8})Cl_2]$ complexes

Catalyst	$E°_{pa}$ (mV)	$E°_{pc}$ (mV)	$E°_{1/2\ Mn^{III}/Mn^{II}}$ (mV)	λ_{max} (π-π*) (nm)	V = (λ_{max}^{-1}) (10^4 cm^{-1})
$[Mn^{II}(HL^3)Cl_2]$ (3)	977	866	921.5	386	2.591
$[Mn^{II}(HL^4)Cl_2]$ (4)	1026	870	948	366	2.73
$[Mn^{II}(HL^5)Cl_2]$ (5)	816	685	750	391	2.56
$[Mn^{II}(HL^6)Cl_2]$ (6)	625	576	600.5	419	2.39
$[Mn^{II}(HL^7)Cl_2]$ (7)	421	354	387.5	455	2.20
$[Mn^{II}(HL^8)Cl_2]$ (8)	455	395	425	448	2.23

More importantly, a linear correlation was found between the energy of the π-π* (CT = charge transfer) absorption and (LMCT = ligand to metal charge transfer) band (λ_{max} and λ_{max}^{-1} =, respectively) and the oxidation potential, *E*pa of the manganese centre of the $[Mn^{II}(HL^{3-8})Cl_2]$ complexes (Figure 21 and 22), indicating that the observed shift in the π-π* and LMCT absorption bands can be assigned indirectly to the electronic effect of the ligands.

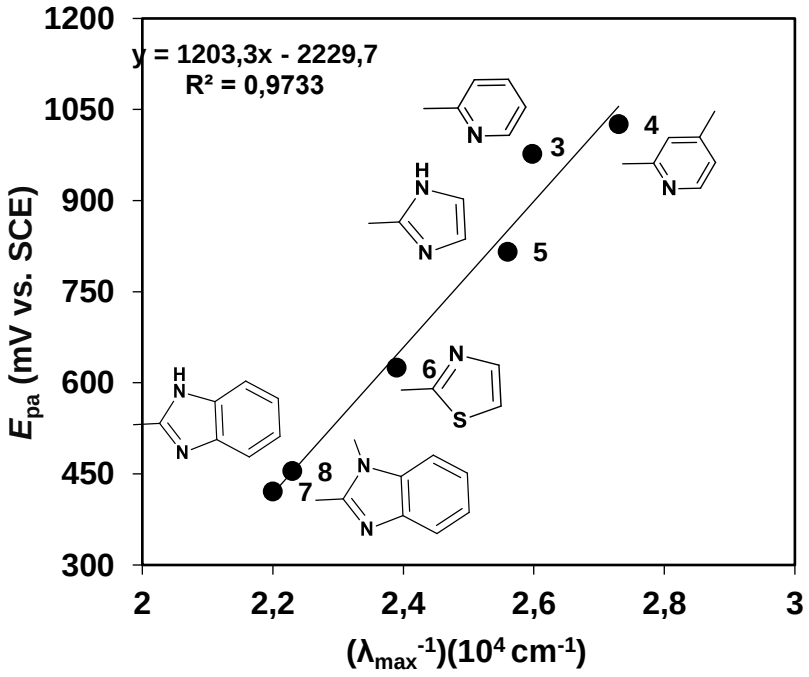

Figure 21. Linear correlation between the oxidation potential of the $[Mn^{II}(HL^{3-8})Cl_2]$ complexes and the energy of the π-π* absorption band

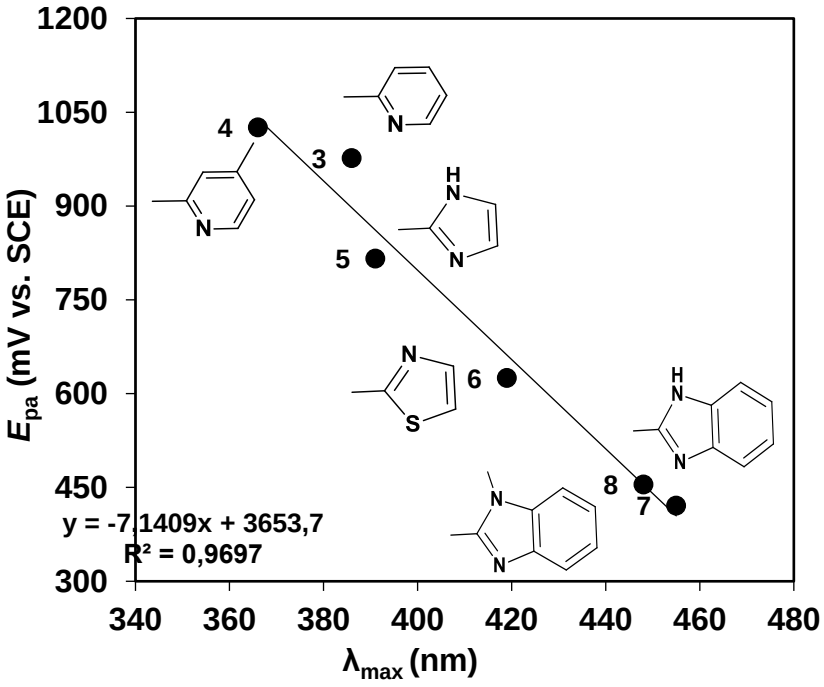

Figure 22. Linear correlation of the oxidation potential of the $[Mn^{II}(HL^{3-8})Cl_2]$ complexes and the energy of the LMCT absorption band

4.5 The catalase-like activity of the manganese-isoindoline complexes

Hydrogen peroxide undergoes decomposition in the presence of manganese-isoindoline complexes at room temperature in buffered aqueous experiments by Stadtman [33-34]. Catalase activity was carried out volumetrically via the measurements of dioxygen evolution at 21˚C in bicarbonate buffers at pH 9.6. The initial reaction rate (V_0) can be defined as ($-d[H_2O_2]/dt = 2(d[O_2]/dt$).

The manganese-isoindoline catalyzed oxidation reactions H_2O_2 could be significantly enhanced through increasing the total carbonate concentration in the reaction mixture. The total carbonate concentration was varied between (0.05 - 0.5 M) [$NaHCO_3$], (Figure 23). The initial rate of the reaction **(V_0)** is a linear function of the bicarbonate concentration, suggesting that 1 equivalent of HCO_3^- is coordinated to the manganese centre during the formation of the catalytically active complex. The first-order dependence with respect to the concentration of bicarbonate is shown in (Figure 24)

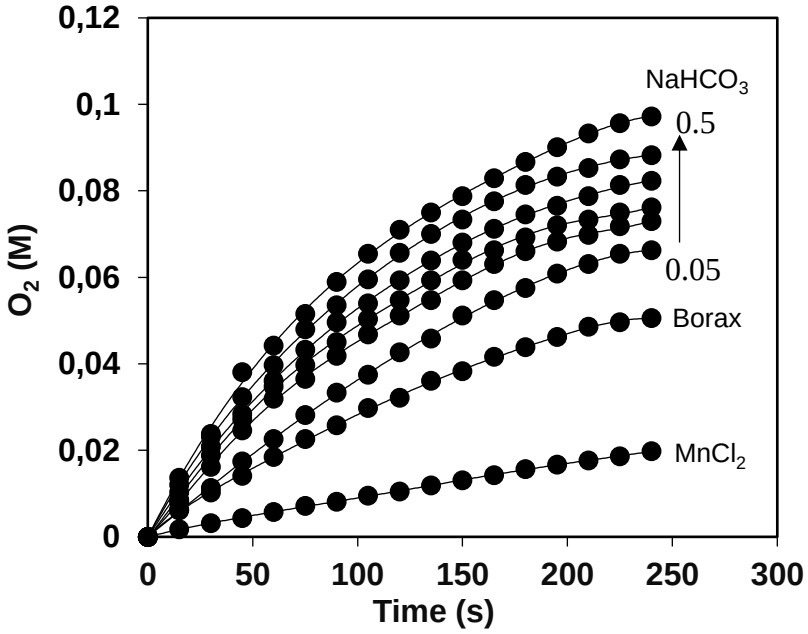

Figure 23. Kinetic analysis for the hydrogen peroxide degradation catalyzed by $MnCl_2$ and $[Mn^{II}(HL^3)Cl_2]$ (**3**) in bicarbonate buffer pH = 9.6 $[Mn^{II}\{(Py)_2\text{-indH}\}(Cl)_2]_0 = 2.11\times10^{-3}$ M, $[H_2O_2]_0 = 4.47\times10^{-1}$ M, at 21 ºC

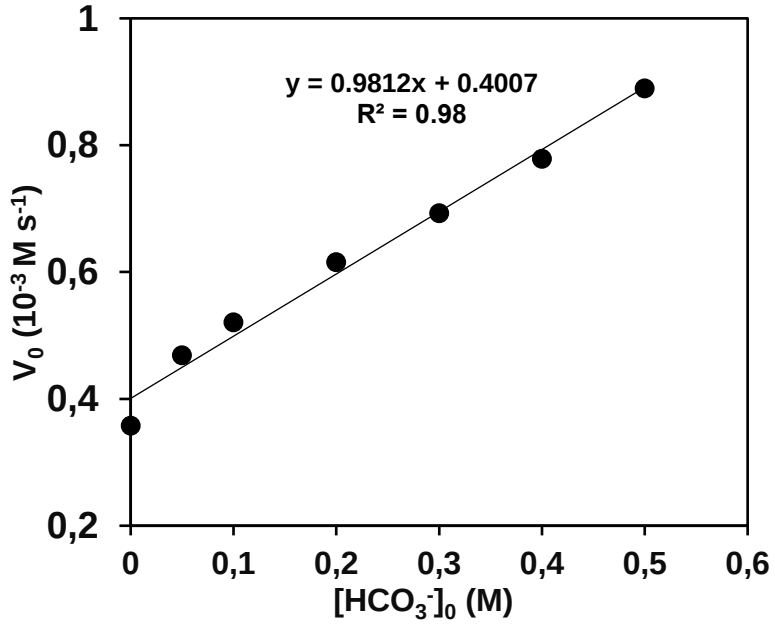

Figure 24. Correlation between V_0 with $NaHCO_3$ by $[Mn^{II}\{(Py)_2\text{-indH}\}(Cl)_2]$, they were performed at pH 9.6 for all complexes.

The catalase activity for the $[Mn^{II}(HL^{3-8})Cl_2]$ complexes and demonstrates significant differences based on the number of H_2O_2 molecules TON = (turnover number) disproportionate by one molecule of the complex after 4 minutes (240 s). The turnover frequency TOF = (mol H_2O_2 / mol catalyst / h) values, which present the ratios of initial rates ($-d[H_2O_2]/dt$) and concentrations of catalysts, are given in table 16. It was found that complex $[Mn^{II}(HL^{4})Cl_2]$ with nonannulated 4-methylpyridyl side chains is the most efficient catalyst with the fastest rate observed at 0.68×10^{-3} Ms^{-1} and approximately 6.5 (TOF) molecules of H_2O_2 broken down per second at the fastest rate of activity (V_0), while complex $[Mn^{II}(HL^{7})Cl_2]$ with annulated benzimidazolyl side chains is the less efficient catalase mimic when compared to complex (**4)**, with the fastest rate of 0.187×10^{-3} Ms^{-1} and the TOF of 1.77 s^{-1} for H_2O_2, based on these results the lower activity may be due to the annulated aromatic side chains within the ligand system which may prevent access of H_2O_2 to the manganese centre (steric effect), or the unfavourable redox and Lewis aciditic properties of the catalyst. (Figure 25).

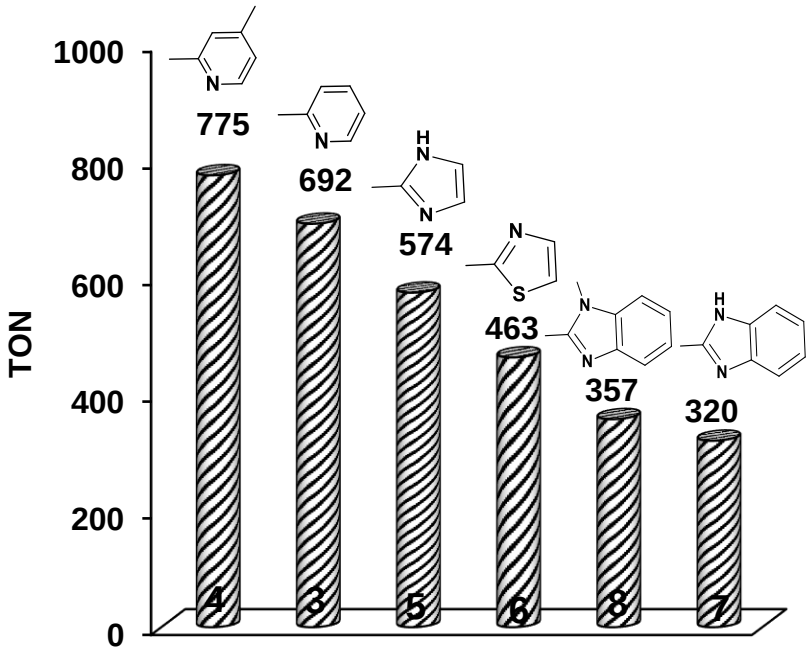

Figure 25. Comparison of the catalase-like activity of $[Mn^{II}(HLn)Cl_2]$ (3-8) $[Mn^{II}]_0 = 2.11\times10^{-3}$ M, $[H_2O_2]_0 = 4.47\times10^{-1}$ M

The progress of the reaction was followed by gas-volumetrically and monitoring the evolution of dioxygen, investigate of buffer solution for $NaHCO_3$ and borax, observed that significantly enhanced through increasing the total carbonate concentration in the reaction mixture due to that evolved higher dioxygen (Figure 26).

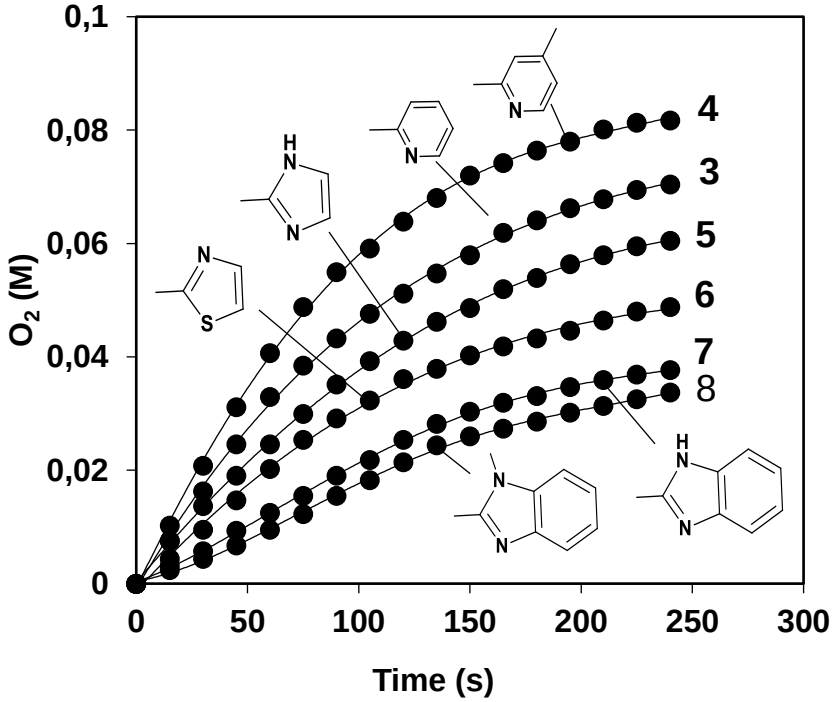

Figure 26. Time traces for the reaction of $[Mn^{II}(HL^{3-8})Cl_2]$ (**3-8**) complexes with H_2O_2 in the presence of bicarbonate, complexes (3-8), $[Mn]_0 = 2.11x10^{-4}$ M, $[H_2O_2] = 4.47\ x10^{-1}$ M, at 21 ºC in 20 cm^3 aqueous buffer solution pH 9.6

The redox potential of the catalysts can be measured under the same conditions; it can be used as excellent reactivity descriptor. By the use of these data, we have got a piece of clear evidence that the activity (V_0) increases almost linearly with the redox potential (E_{pa} for Mn^{III}/Mn^{II}) of the catalyst (Figure 27). This finding also suggests that the redox potential of the catalysts acts as the driving force of the reaction. The higher the redox potentials of Mn^{III}/Mn^{II} redox couple the higher is the catalase-like activity, $\log V_0$. $[Mn^{II}(HL^{3-4})Cl_2]$ **(3-4)** complexes with pyridyl side chains.

The metal sites are electron-deficient are faster in catalyzing H_2O_2 disproportionation than electron-rich derivatives $[Mn^{II}(HL^{5-8})Cl_2]$ **(5-8)** with more Lewis basic benzimidazolyl side chains The redox potential values of Mn^{III}/Mn^{II} redox couple describe the propensity of the manganese(II) complexes to react with the nucleophilic HO_2^- and/or HCO_4^- where the more electron-deficient metal center has a much higher affinity for HO_2^- and/or HCO_4^- binding.

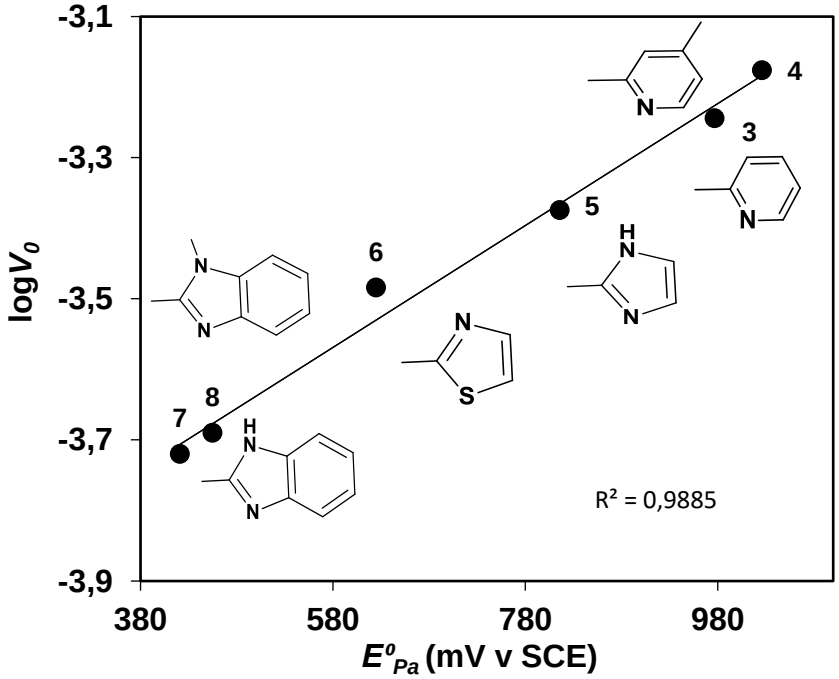

Figure 27. Dependence of the reaction rate on the oxidation potential E^o_{pa} (mV vs SCE)

4.6 Oxidation of morin

In order to evaluate the bleaching potential of $[Mn^{II}(HL^{3-8})Cl_2]$, complexes, we have investigated the oxidation of morin, which can be considered as a good model compound for bleaching stain. Oxidative degradation of morin by H_2O_2 under catalytically relevant experimental conditions, kinetic studies were performed for solutions in which the carbonate containing water solution, experiments were carried out at 25 ˚C with 1.6 M catalyst, (10 mM) H_2O_2 and (0.16 mM) morin and the oxidation of morin was followed as the decrease in absorbance at 410 nm.

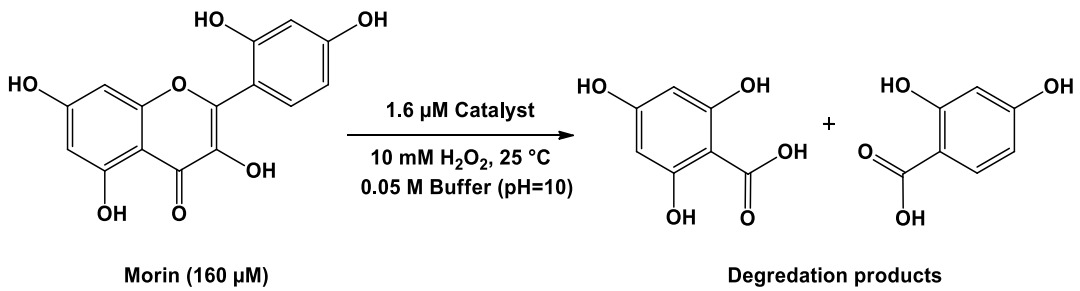

Scheme 13. Structure of 2′,3,4′,5,7-pentahydroxyflavone (morin) and the applied reaction condition in the catalytic oxidations reaction

The results were presented in (Figure 28), shows that the observed rate constant initially increased with increasing the complex concentration. The plot shows a linear dependence on the initial concentration over the studied concentration range of the complex, so base on this results reaction rate is first order with respect [Mn^{II}].

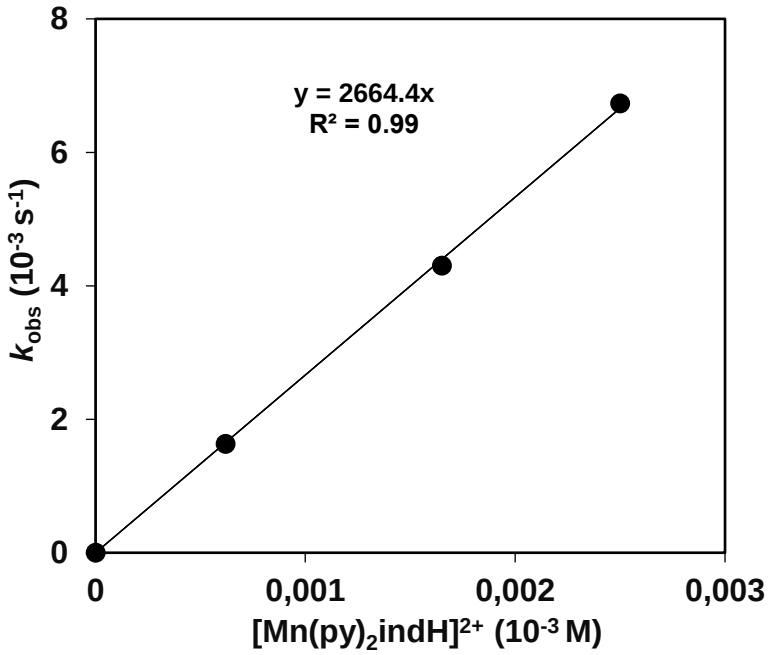

Figure 28. Dependence of the first-order rate constant (k_{obs}) for morin oxidation on the [Mn^{II}{$(Py)_2$-indH}$(Cl)_2$] **(3)**, $[morin]_0 = 1.6\times10^{-4}$ M, $[H_2O_2]_0 = 1\times10^{-2}$ M, pH 10 at 25 °C

The effect of H_2O_2 on the oxidation reaction course was studied by varying its initial concentration over a wide range, between 2.5 to 10 mM. At higher H_2O_2 concentrations (10 mM) a fast oxidation reaction occurs followed by rapid consumption of H_2O_2. This prompted us to study the H_2O_2 concentration effect on the catalytic oxidation of the dye at different concentrations (Table S9, Figure 29),

The plot shows that the observed rate constant initially increased with increasing the $[H_2O_2]$ concentration, a linear dependence on the initial concentration over the studied concentration range of H_2O_2, based on this results reaction rate is first order with respect $[H_2O_2]$.

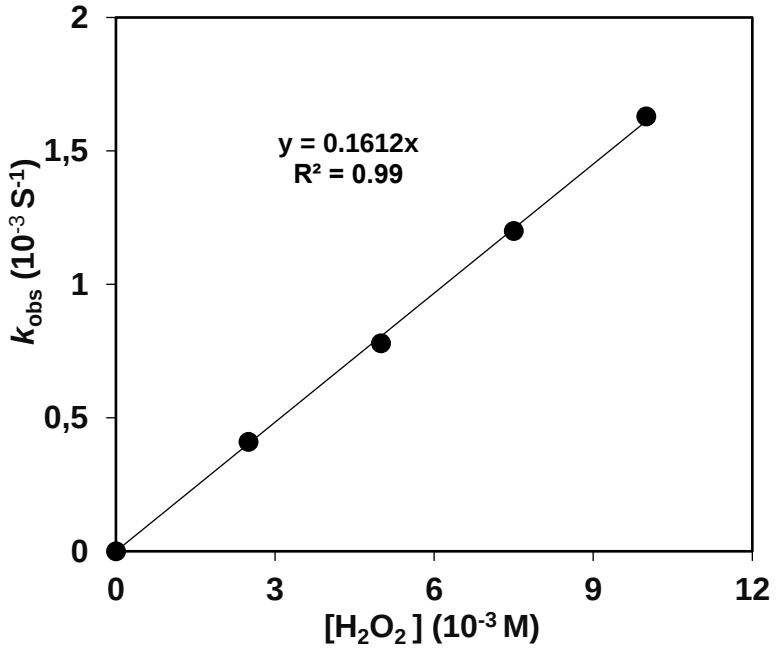

Figure 29. Hydrogen peroxide concentration dependence of k_{obs}, $[Morin]_0$ = 1.6×10^{-4} M, $[Mn^{II}\{(Py)_2\text{-indH}\}(Cl)_2]_0 = 6.2\times10^{-7}$ M, pH 10 at 25 °C

To evaluate the effect of the morin concentration on the $[Mn^{II}\{(Py)_2\text{-indH}\}(Cl)_2]$ complex catalyzed oxidative degradation of morin by H_2O_2 under catalytically relevant experimental conditions, we observed that the rate constant not increased with increasing the [morin] concentration (Table S9).

The effect of the carbonate concentration on the oxidative degradation of morin was studied at pH 10. According to research studied [38], as well as the results described above, establish that the bicarbonate concentration plays an important role in the overall oxidation reaction. The $[Mn^{II}\{(Py)_2\text{-indH}\}(Cl)_2]$ catalyzed oxidative degradation of morin by using H_2O_2 as an oxidizing agent could be significantly enhanced in all cases through increasing the total carbonate concentration in the reaction mixture (Figure 30).

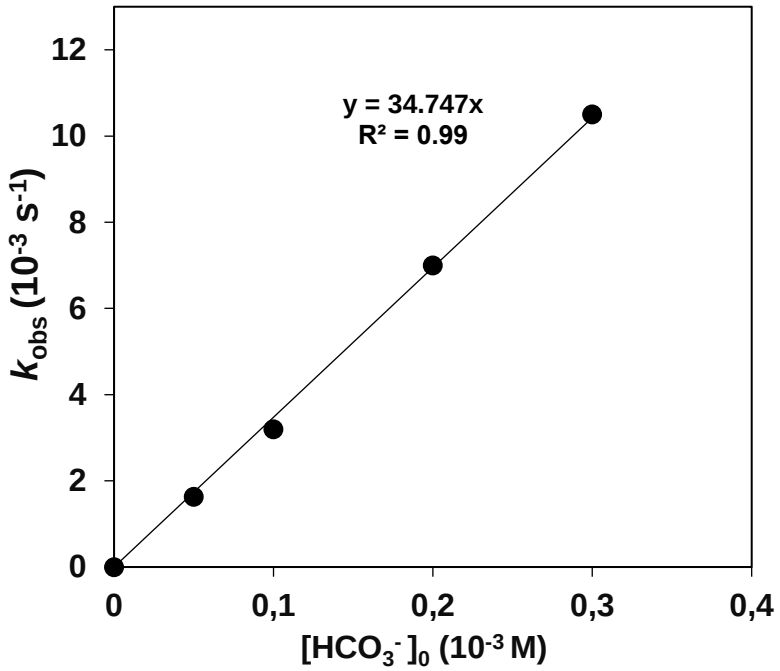

Figure 30. Hydrogen carbonate concentration dependence of k_{obs}, $[Morin]_0$ = 1.6×10^{-4} M, $[Mn^{II}\{(Py)_2\text{-indH}\}(Cl)_2]_0 = 6.2\times10^{-7}$ M, $[H_2O_2]_0 = 1\times10^{-2}$ M, pH 10 at 25°C

From the detailed of kinetic measurements, the rate of morin decomposition is described by the relationship $-d[morin]/dt = V = k_{ox}$ [**3-8**]$[H_2O_2][HCO_3^-][morin]$, where $k_{ox} = 7.79 \times 10^6$ $M^{-3}s^{-1}$ for (**4**) and 0.675×10^6 $M^{-3}s^{-1}$ for **(7)** (Table 18). The catalytic activity of the 4-methylpyridyl containing manganese complex (**4**) was at least 10-12 times higher than that of $[Mn^{II}(HL^7)Cl_2]$ (**7**) with benzimidazolyl side chains.

At low substrate concentration the reaction is first-order on all reactants. It is worth noting that the bicarbonate concentration similarly the previous results plays an important role in the bleaching process, Base on the results of previous kinetic studies, may suggest both the formation of high valent $Mn^{IV}(O)$ species in Route 1 (Scheme 12) and carbonate radical in Fenton-type chemistry in Route 2 (Scheme 12), as key catalytic intermediates which may lead to the dismutation of H_2O_2. We believe that bicarbonate ions act upon the redox potential of a Mn(II) complex.

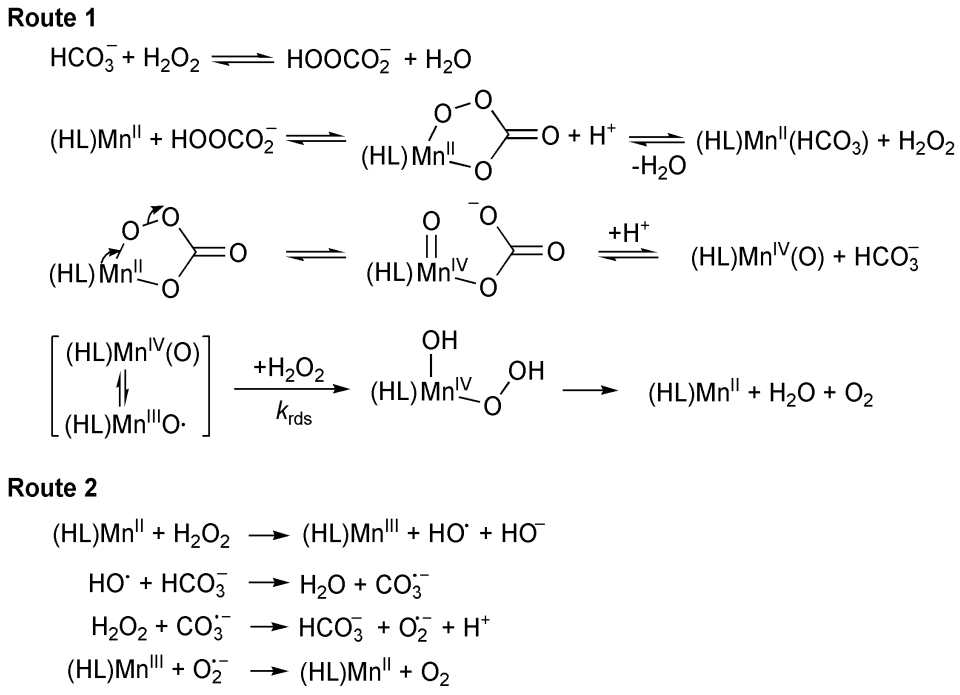

Scheme 12. Proposed mechanisms for dismutation of H_2O_2 by $[Mn^{II}(HL^{3\text{-}8})Cl_2]$

4.7 Bleaching test for the manganese-isoindoline complexes

The oxidation of morin can be monitored by measuring the time-resolved absorbance at 410 nm by UV-Vis spectroscopy. Without any catalyst, the oxidative degradation of morin with H_2O_2 at pH 10 is negligible among the conditions of the experiment. The typical spectral changes in the presence of a catalyst are demonstrated for $[Mn^{II}\{(Py)_2\text{-indH}\}(Cl)_2]$ (figure 31).

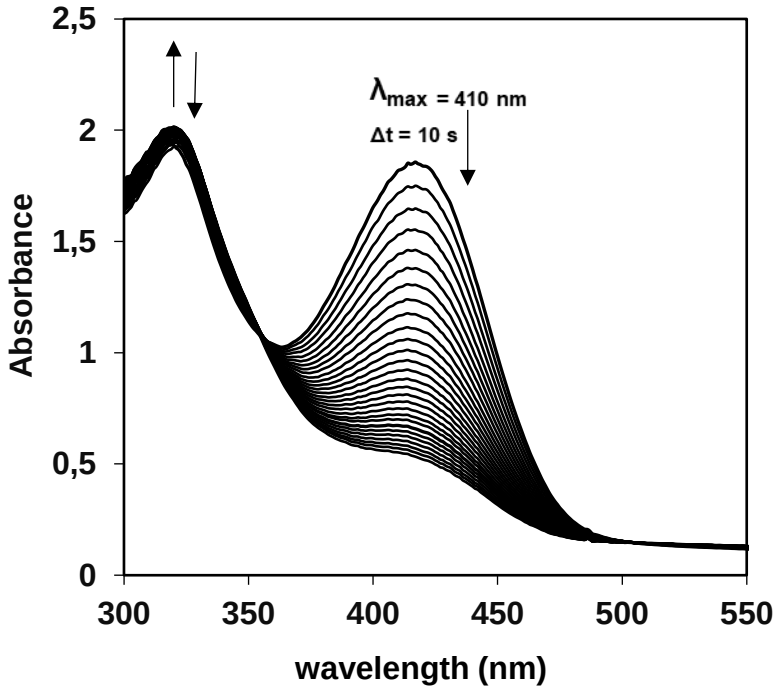

Figure 31. Time-dependent UV-Vis spectra of $[morin]_0 = 1.6\times10^{-4}$ M solution of at pH 10 in the presence of $[H_2O_2]_0$ = 10 mM, $[Mn^{II}\{(Py)_2\text{-indH}\}(Cl)_2]_0$ = 1.6 μM

In this case, the reaction was completed and the spectral changes mark two stages of the reaction, in the initial stage the band at 321 nm increases along with the decrease of the 410 nm band. The isosbestic point at 355 nm shows that only a single reaction product is formed. After the first period, the band at 321 nm also starts to decrease indicating further oxidation of the initial product. Assignment of the 321 nm absorption maximum analysis of further products has been done earlier. In focus only on the rate of morin oxidation into a single product.

After measuring the antioxidant activity of the complexes, it seemed reasonable to check the pro-oxidant capabilities. For this reaction, we investigated the oxidative degradation of morin by hydrogen peroxide, in the presence of the manganese-isoindoline complexes **(3-8)**. The best activity was observed for $[Mn^{II}(HL^2)Cl_2]$ (**4**) where the bleaching of morin was completed within 5 minutes with approximately 20 catalytic cycles per minute (figure 32).

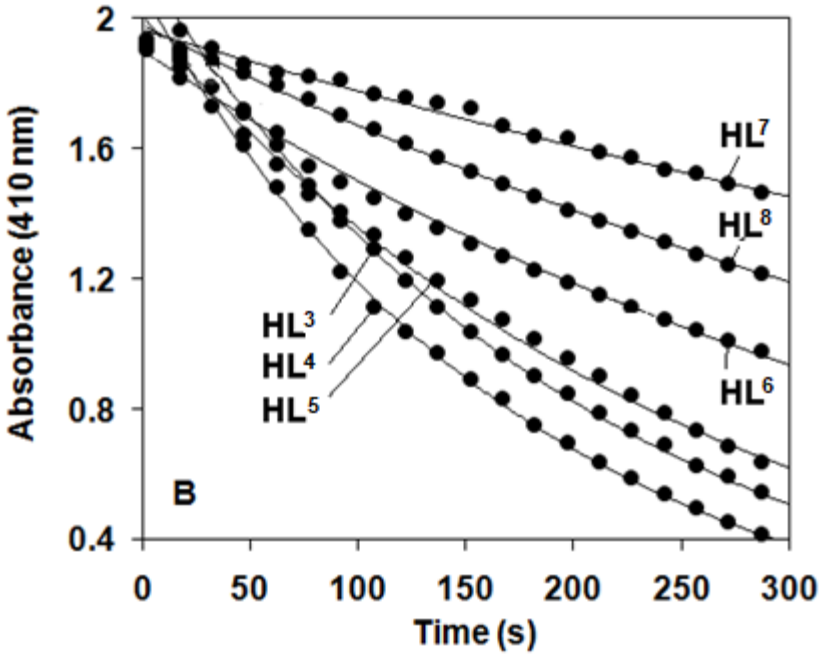

Figure 32. Degradation of morin by hydrogen peroxide in the presence of the Mn(II) complexes (3-6), of $[morin]_0$ = 1.6×10^{-4} M solution of at pH 10 in the presence of $[H_2O_2]_0$ = 10 mM, $[Mn^{II}\{(Py)_2\text{-indH}\}(Cl)_2]_0$ = 1.6 μM

Table 18. Summary of kinetic data for the catalytic oxidation of morin with $[Mn(HL^{3\text{-}8})Cl_2]$ (**3-8**) in bicarbonate buffer at pH 10 and 25 ˚C

Catalyst	$E°_{pa}$ (mV)	$E°_{pc}$ (mV)	$E°_{1/2\ Mn^{III}/Mn^{II}}$ (mV)	k_{obs} (10^{-3} s^{-1})	k_{ox} (10^{6} M^{-3} s^{-1})
$[Mn^{II}(HL^3)\ Cl_2]$ (3)	977	866	921.5	4.2±0.12	5.2±0.16
$[Mn^{II}(HL^4)\ Cl_2]$ (4)	1026	870	948	6.2±0.15	7.8±0.2
$[Mn^{II}(HL^5)\ Cl_2]$ (5)	816	685	750	1.7±0.08	1.71±0.11
$[Mn^{II}(HL^6)\ Cl_2]$ (6)	625	576	600.5	1.3±0.02	1.4±0.03
$[Mn^{II}(HL^7)\ Cl_2]$ (7)	421	354	387.5	0.45±0.01	0.67±0.02
$[Mn^{II}(HL^8)\ Cl_2]$ (8)	455	395	425	0.78±0.02	0.97±0.03

The complexes show reversible redox transitions involving Mn(II) and Mn(III) redox states. As the catalysis of the dismutation of hydrogen peroxide is a redox process the potential and reversibility of the Mn(III)/Mn(II) couple is a key parameter.

The activity of the isoindolin complexes increases significantly in the order of $[Mn(HL^7)Cl_2]$ (**7**) < $[Mn(HL^8)Cl_2]$ (**8**) < $[Mn(HL^6)Cl_2]$ (**6**) < $[Mn(HL^5)Cl_2]$ (**5**) < $[Mn(HL^3)Cl_2]$ (**3**) < $[Mn(HL^4)Cl_2]$ (**4**). Hence, by changing the more Lewis basic five-membered benzimidazolyl rings to six-membered pyridyl pendant arms, the catalytic activity can be remarkably enhanced. The manganese-isoindoline complexes (**3**-**8**) are shown a linear correlation between log(k_{obs}) with E^o_{pa} (mV vs SCE) (Figure 33).

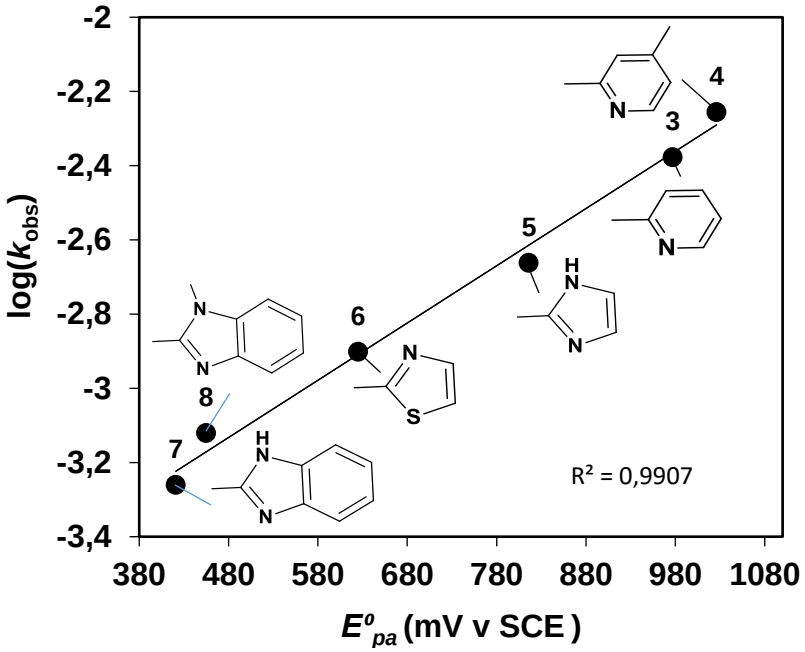

Figure 33. Dependence of the first-order rate constant (k_{obs}) for morin oxidation on the oxidation potential (E_{pa}) of the $[Mn^{II}(HL^{4-8})Cl_2]$ complexes in bicarbonate buffer (pH 10). Conditions: $[Complexes\ 3\text{-}8]_0 = 1.6 \times 10^{-6}$ M, $[morin]_0 = 0.16 \times 10^{-3}$ M, $[H_2O_2]_0 = 0.010$ M at 25 °C

4.8 Morin oxidation under air condition

To investigate the effect of the catalyst concentration on the manganese-isoindoline catalyzed oxidative degradation of morin by air condition under catalytically relevant experimental conditions, kinetic studies were performed for solutions in which the carbonate containing water solution with complex of $[Mn^{II}\{(Py)_2\text{-}indH\}(Cl)_2]$ was added in the presence of air atmosphere and (0.16 mM) morin solution at 25 °C.

Table 19. Redox potentials, $E°_{pa}$ and E^{o}_{pc} values of the manganese complexes

Catalyst	$E°_{pa}$ (mV)	$E°_{pc}$ (mV)	$E°_{1/2\ Mn^{III}/Mn^{II}}$ (mV)	k_0 (10^{-4} s^{-1})
$[Mn^{(II)}(HL^3)\ Cl_2]$ (3)	977	866	921.5	2.569±0.006
$[Mn^{(II)}(HL^4)\ Cl_2]$ (4)	1026	870	948	3.925±0.004
$[Mn^{(II)}(HL^5)\ Cl_2]$ (5)	816	685	750	1.728±0.012
$[Mn^{(II)}(HL^6)\ Cl_2]$ (6)	625	576	600.5	1.103±0.014
$[Mn^{(II)}(HL^7)\ Cl_2]$ (7)	421	354	387.5	0.399±0.002
$[Mn^{(II)}(HL^8)\ Cl_2]$ (8)	455	395	425	0.541±0.003

The reaction was completed and the spectral changes show the stage of the reaction, in the initial stage the band at 327 nm increases along with the decrease of the 407 nm band. Continuously when morin starts to gradate at 407 nm the formation rate of product increases (figure 34).

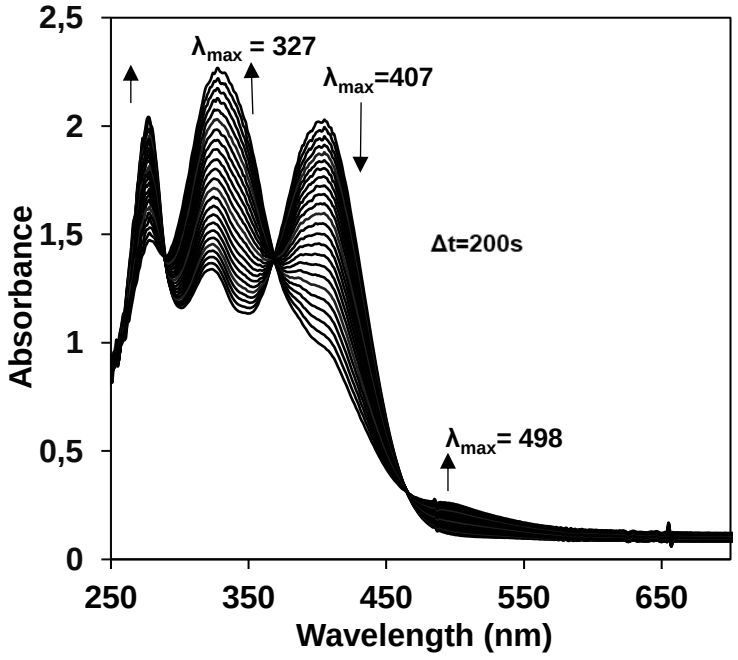

Figure 34. Time dependent UV-visble spectra of $[morin]_0 = 1.6\times10^{-4}$ M solution of at pH 10 in the presence of air condition, $[Mn^{II}\{(Py)_2\text{-indH}\}(Cl)_2]_0 = 1.6$ μM

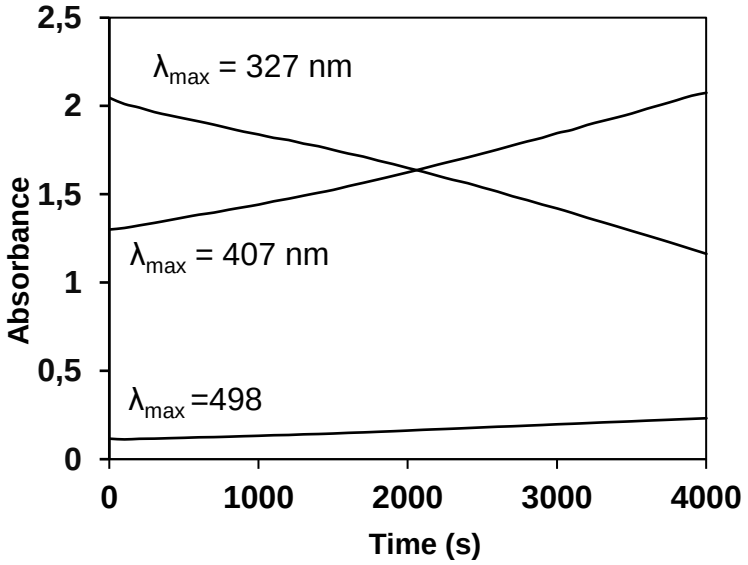

Figure 35. Kinetic traces of complexation and oxidation of morin $[morin]_0$ = 1.6×10^{-4} M solution of at pH 10 in the presence of air condition, $[Mn^{II}\{(Py)_2\text{-}indH\}(Cl)_2]_0$ = 1.6 μM

The linear correlation between $\log(k_0)$ and $E^o_{1/2}$ (mV vs SCE) for the manganese-isoindoline complexes was shown in (Figure 36).

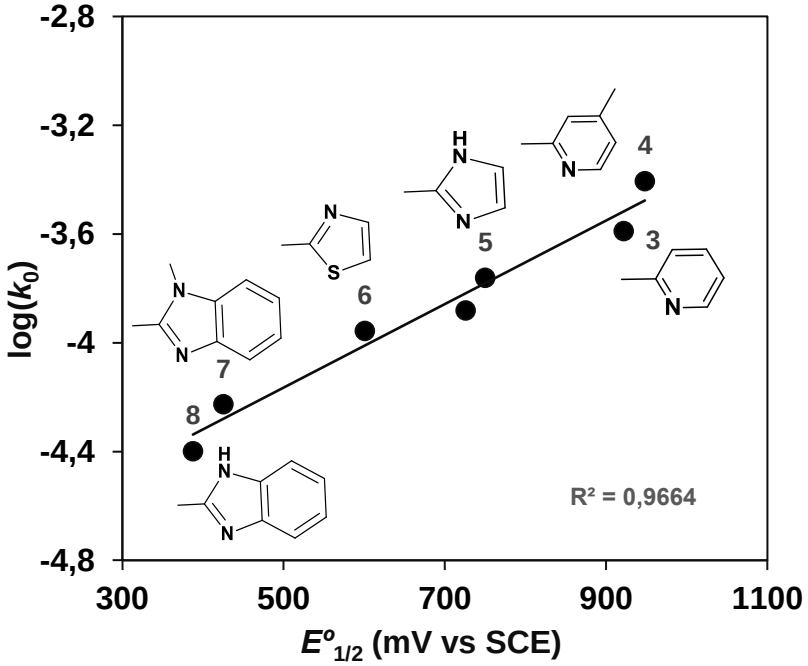

Figure 36. Established linear correlation between $\log(k_0)$ and $E^o_{1/2}$ (mV vs SCE) for the manganese-isoindoline complexes

In summary, Efforts have been made to work out highly efficient and highly selective manganese-based catalytic system for the disproportionation reaction of H_2O_2 as synthetic catalase mimics and for the oxidation of morin as oxidative bleaching performances. Manganese-isoindoline complexes such as, $[Mn^{II}(HL^3)Cl_2]$ (3), $[Mn^{II}(HL^4)Cl_2]$ (4), $[Mn^{II}(HL^5)Cl_2]$ (5), $[Mn^{II}(HL^6)Cl_2]$ (6), $[Mn^{II}(HL^7)Cl_2]$ (7) and $[Mn^{II}(HL^8)Cl_2]$ (8), synthesized and characterized by various electro-chemical and spectroscopic methods. After that, investigated the effect of the ligand modification by varying the aryl substituent on the bis-iminoisoindoline moiety with emphasis on the redox potential. We observed that the higher the redox potentials of Mn^{III}/Mn^{II} redox couple the higher is the catalase-like and bleaching activity. It is also worth to note that the bicarbonate concentration plays an important role in both the catalase-like reaction and bleaching process, probably during the formation of the proposed catalytically active $Mn^{IV}(O)$ species.

4.9 Catalytic oxidation of flavanone

The catalytic activities of the manganese-isoindoline complexes $[Mn^{II}(HL^3)Cl_2]$ (3), $[Mn^{II}(HL^4)Cl_2]$ (4), $[Mn^{II}(HL^5)Cl_2]$ (5), $[Mn^{II}(HL^6)Cl_2]$ (6), $[Mn^{II}(HL^7)Cl_2]$ (7) and $[Mn^{II}(HL^8)Cl_2]$ (8) were studied in the oxidation of flavanone, utilizing *m*-CPBA as co-oxidant. The oxidation reactions were carried out under standard catalytic conditions (5:300:500 ratios for catalyst: oxidant: substrate) in acetonitrile at 25 ºC. The excess amount of the substrate was used to minimize over oxidation of the product to get evidence for the formation of possible intermediates. It took less than 10 min to get about 20-35% yields based on oxidant for the Mn(II)-catalyzed reactions. These reactions were also examined on varying the period time between 10-30 minutes, where we observed the flavone yield attained a peak after 10 minutes of reaction and remained the same even after 30 minutes, and much smaller yield (2.1%) was obtained for the blank $Mn^{II}(ClO_4)_2$ salt. The Mn(II)-catalyzed reactions of flavanone produced flavones (F) as expected major product in all cases with the minor product of 1,3-diphenylpropane-1,3-dione (D) which was identified by GC-MS/MS (Scheme 14).

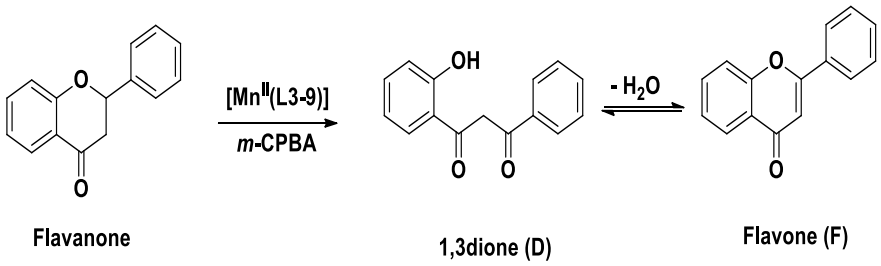

Scheme 14. Oxidation of flavanone to flavones by *m*-CPBA

The investigation of the flavanone oxidation in the presence of various co-oxidants such as, *m*-CPBA, TBHP and H_2O_2, then comparing the value of TOF revealed that the TBHP and H_2O_2 (Table S11, Figure 37), are much lower value of TOF may be due to unstable intermediate, therefore, cannot trap intermediate form for Mn^{II}.

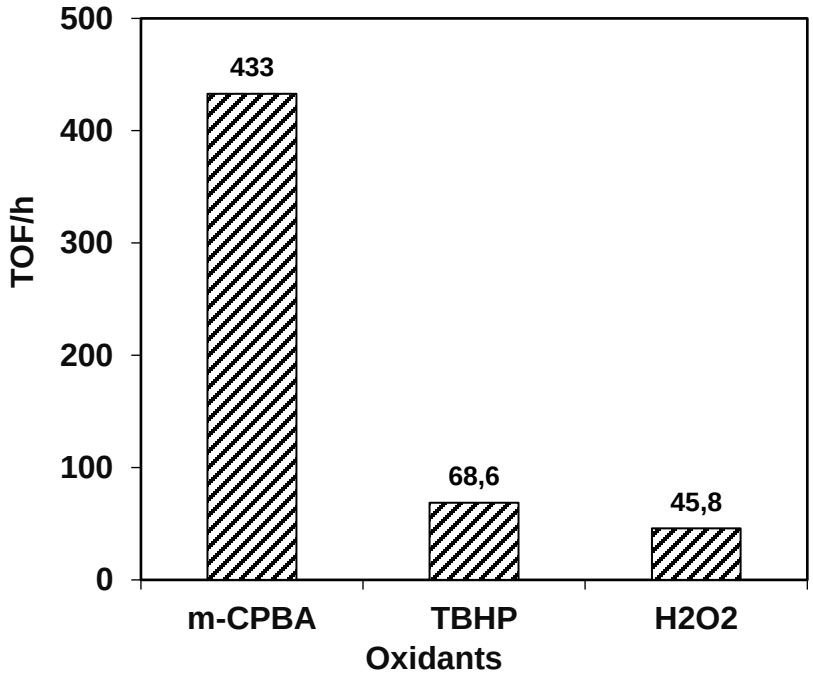

Figure 37. Oxidation of flavanone with various co-oxidant catalase by $[Mn^{II}\{(Py)_2\text{-}indH\}(Cl)_2]$, $[Mn^{II}]_0$ = 5 mM, $[S]_0$ = 300 mM, $[Oxidant]_0$ = 500 mM, in acetonitrile at 25 °C

The turnover frequency is calculated from the ratio of the amount of the reacted flavanone to the amount of the catalyst divided by time of the reaction. The TOF values were significantly increased by increasing the concentration of the oxidant *m*-CPBA. Significantly higher yield (36 %; TOF/h for F = 433, TOF/h for D = 126) was observed for complex $[Mn^{II}\{(Py)_2\text{-indH}\}(Cl)_2]$, (Figure 37). The ligand structure influenced the catalytic activities of these complexes, the complexes values indicate that the relative reactivities of manganese(II) complexes are in the order of $HL^3 > HL^4 > HL^5 > HL^6 > HL^7 > HL^8$ based on reactivity (Table S10, Figure 38).

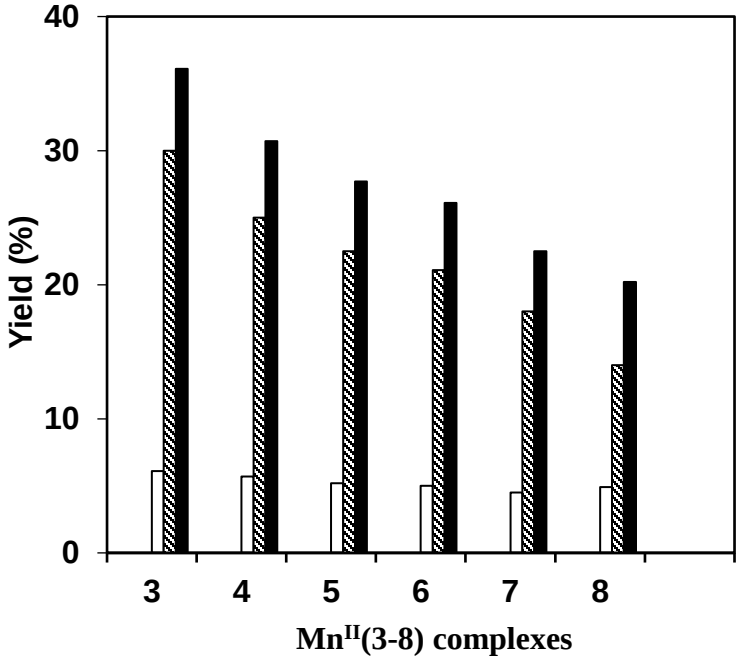

Figure 38. Catalytic oxidation of flavanone by the manganese-isoindoline complexes (3-8), (black column) total yield, (line column) yield of flavones (F) and (white column) yield of 1,3-dione (D). $[Mn^{II}]_0$ = 5 mM, $[S]_0$ = 300 mM, $[Oxidant]_0$ = 500 mM, in acetonitrile at 25 °C by *m*-CPBA

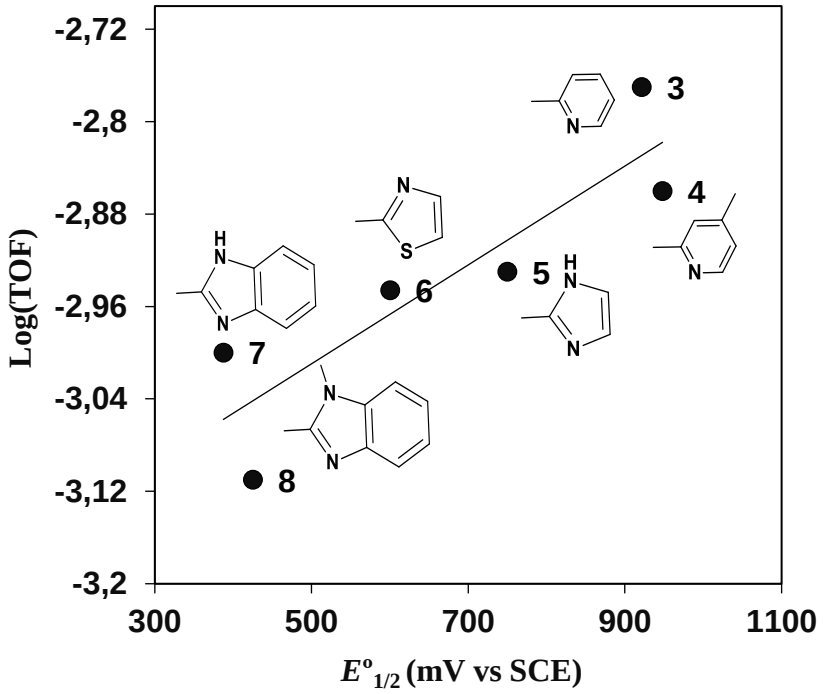

Figure 39. Correlation between log(TOF) and $E^o_{1/2}$ (mV vs SCE) for the manganese-isoindoline complexes, (Table S13)

It is important to mention that in the presence of water, the yield of flavones decreases and the amount of 1,3-dione (D) increased (Table S9, Figure 40), this can be attributed to an equilibrium step during the flavone formation (Scheme 14). An increase in the yield of flavone was observed when the amount of catalyst was increased. In the absence of catalyst in the blank experiment, no flavone formation was detected under the same conditions.

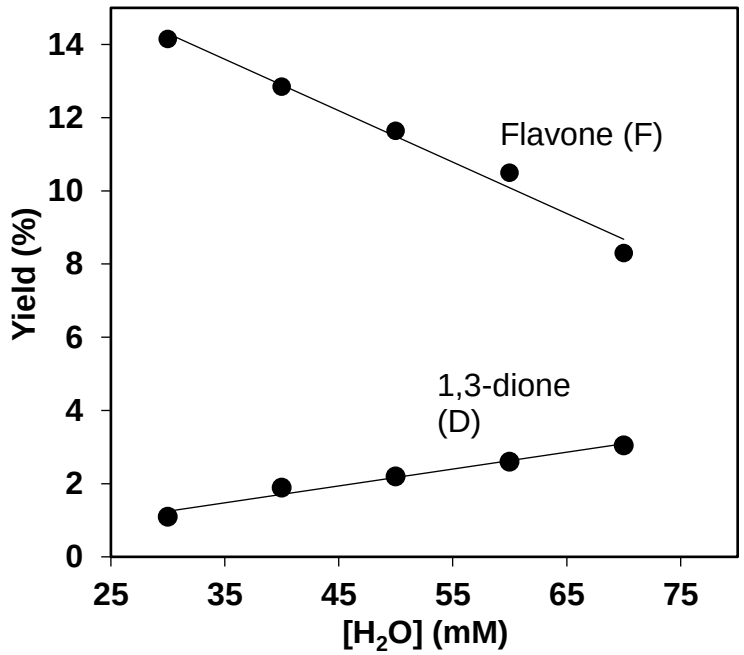

Figure 40. Effect of [H_2O] on the yield of flavones (F) and 1,3-dione (D)

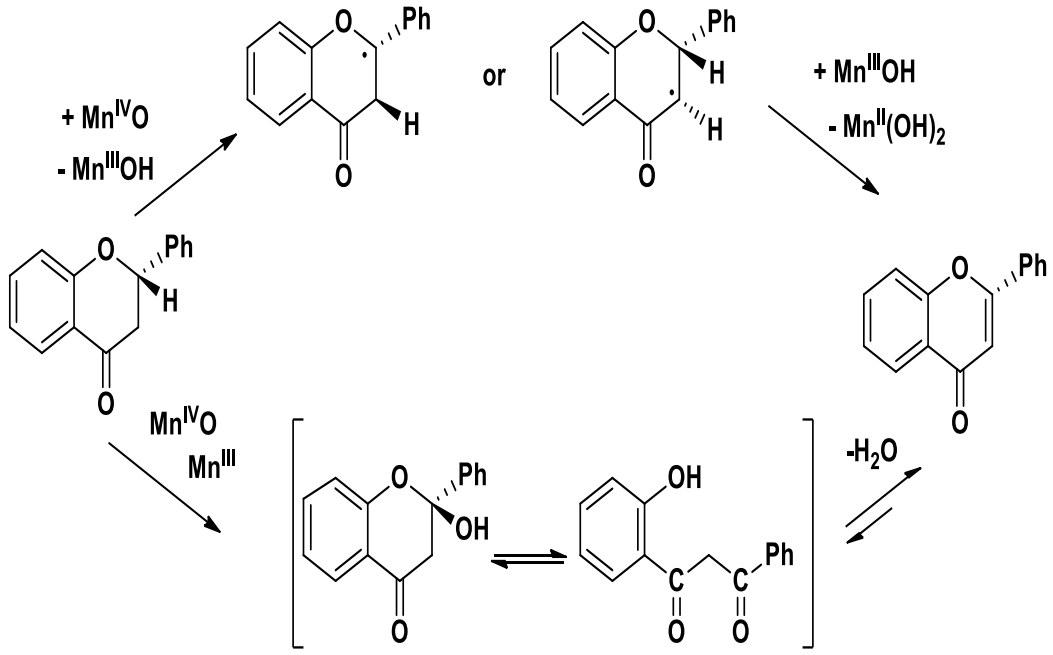

Scheme 15. The metal based mechanism proposed for oxidation flavanone by *m*-CPBA

4.10 Catalytic oxidation of *N,N*-dimethylanilines under air

Reactions were carried out under standard catalytic conditions (1: 300: 300 for the catalyst: DMA: co-oxidant) in acetonitrile at room temperature under air (Ar). Co-oxidants were added by syringe, and the excess of DMA was used to minimize the over oxidized products. The catalytic activity and selectivity of complex and the Mn(II) salt appeared to be dependent on the co-oxidants used for oxidation. The $Mn^{II}(ClO_4)_2$ salt together with *m*-CPBA oxidizes DMA to MA and MFA, and a turnover number (TON) of 1.94 MA and 0.86 MFA was obtained with an overall yield of 2.78 %. The almost identical result has been observed by the use of PAA as co-oxidant (1.6 and 0.6 TON, respectively), When TBHP, PhIO and H_2O_2 were used as co-oxidants significantly lower activities were observed (TON 0.70, 0.56 and 0.41 respectively). The higher reactivity of peracids compared to H_2O_2, PhIO and TBHP may be explained by the in situ formed $[Mn_3O(OAc)_3]^+$ and $[Mn_3O(mCBA)_3]^+$ complexes with remarkably much higher catalytic activities compared to the parent $Mn^{II}(ClO_4)_2$ salt (Figure 44).

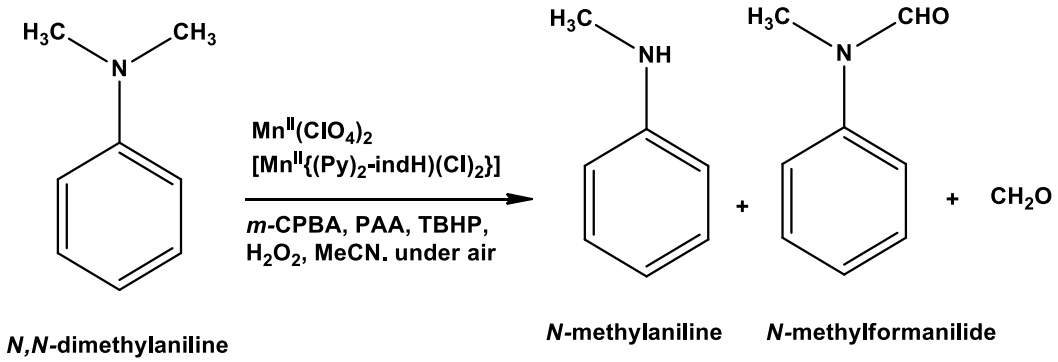

Scheme 16. Catalytic oxidation of *N,N*-dimethylaniline (DMA) $[Mn^{II}\{(Py)_2\text{-}indH\}(Cl)_2]$ and $Mn(ClO_4)_2$ salt under air system

The catalytic activity of $[Mn^{II}\{(Py)_2\text{-}indH\}(Cl)_2]$ was also examined including the same co-oxidants, and conditions used above, facilitating direct comparison with results obtained with the parent Mn(II) salt. In (Table S11and S12, Figure 41) show that there is an increase in the overall yield.

The oxidants employed are H_2O_2, PhIO, TBHP, *m*-CPBA, and PAA (from 0.41 to 47 %), albeit with moderate product selectivity. The order of efficacy for the co-oxidants was found to be *m*-CPBA > PAA > TBHP > PhIO > H_2O_2 in the presence of the Mn(II) catalyst, which can be explained by the different mechanism of the Mn(IV)-oxo formation and the presence or absence of hydroxyl (tert-butoxy) radicals.

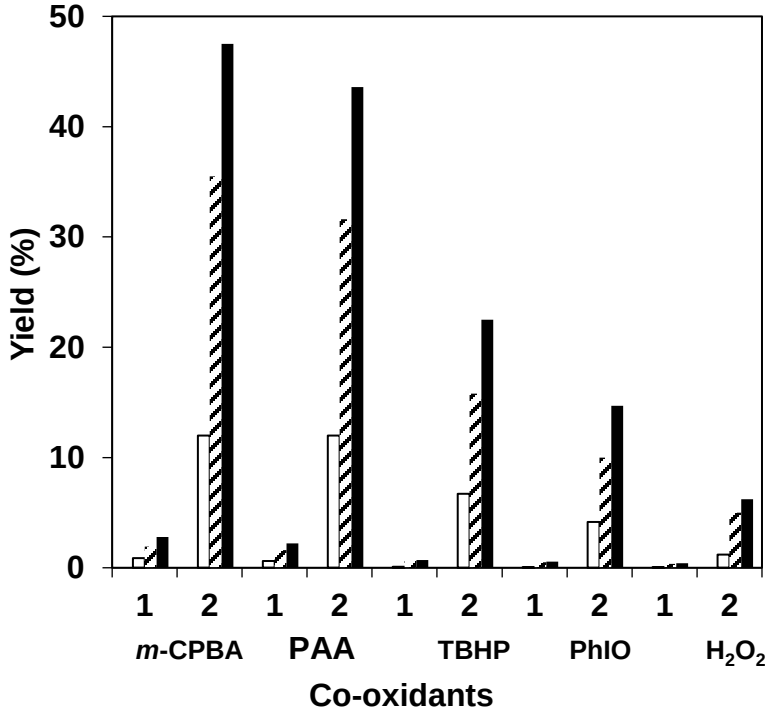

Figure 41. Comparison of the product formation of $Mn^{II}(ClO_4)_2$ and $[Mn^{II}\{(Py)_2\text{-indH}\}(Cl)_2]_0$ = 3 mM, $[S]_0$ = 300 mM), $[Ox]_0$ = 300 mM, oxidation of *N*,*N*-dimethylaniline to *N*-methylaniline (line column), *N*-methylformanilide (white column), total yield (black column) in CH_3CN at 30°C

Derivatives of *N*,*N*-dimethylanilines were observed to produce corresponding secondary anilines where anilines with electron-donating groups on the phenyl ring gave better yields and selectivity than those with electron-withdrawing groups, suggesting a metal-based oxidant with electrophilic character (Figure 42). It can also be seen that the product composition (MA/MFA ratio) being remarkably influenced by the electron density on the substrate, especially in the 1/ *m*-CPBA system.

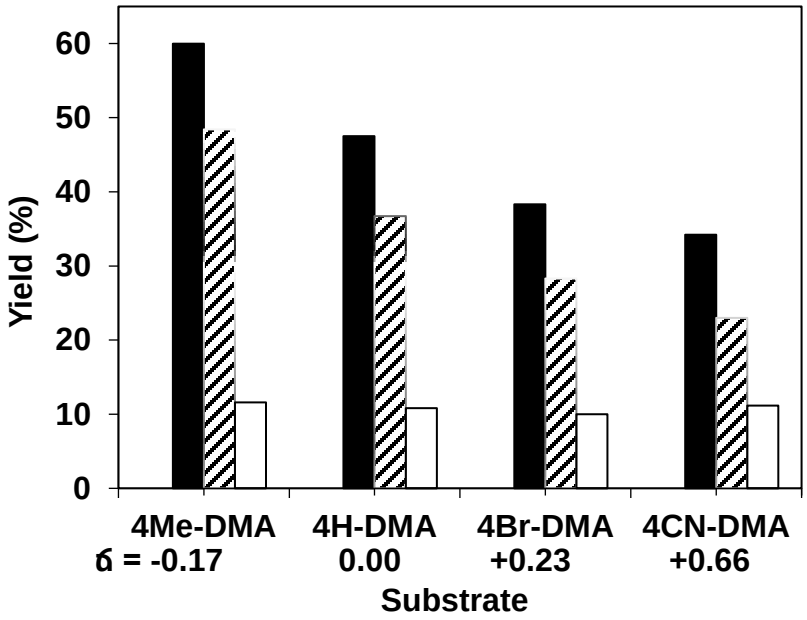

Figure 42. Comparison of the product formation in the oxidation of *N*,*N*-dimethyl-anilines, $[Mn^{II}]_0$ = 3 mM, $[S]_0$ = 300 mM, $[Ox]_0$ = 300 mM, *N*,*N*-methylaniline (line column), *N*-methylformanilide (white column) and total yield (black column) derivatives with *m*-CPBA in CH_3CN at 30 °C (Table S13)

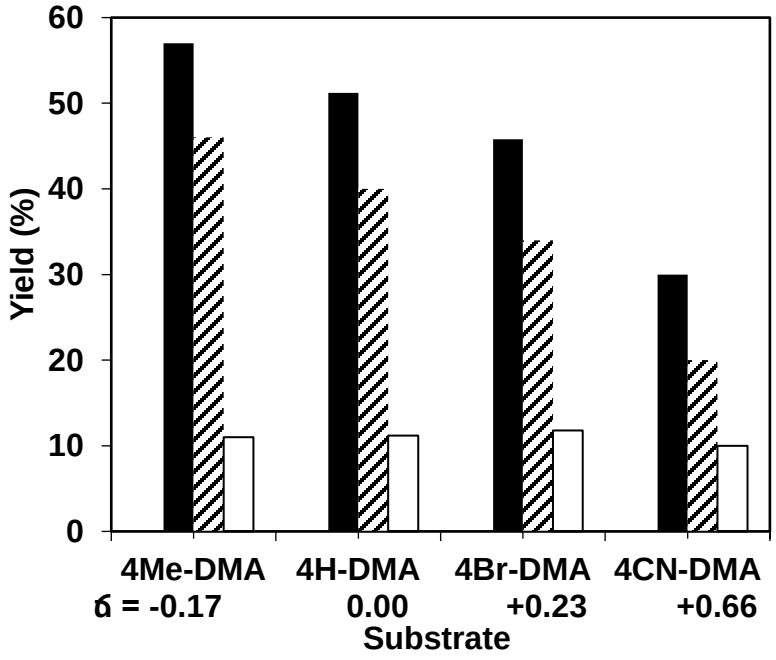

Figure 44. Comparison of the product formation in the oxidation of *N*,*N*-dimethyl-anilines, $[Mn^{II}]_0$ = 3 mM, $[S]_0$ = 300 mM, $[Ox]_0$ = 300 Mm, (Table S13). *N*,*N*-methylaniline (line column), *N*-methylformanilide (white column) and total yield (black column) derivatives with *m*-CPBA in CH_3CN at 30 °C

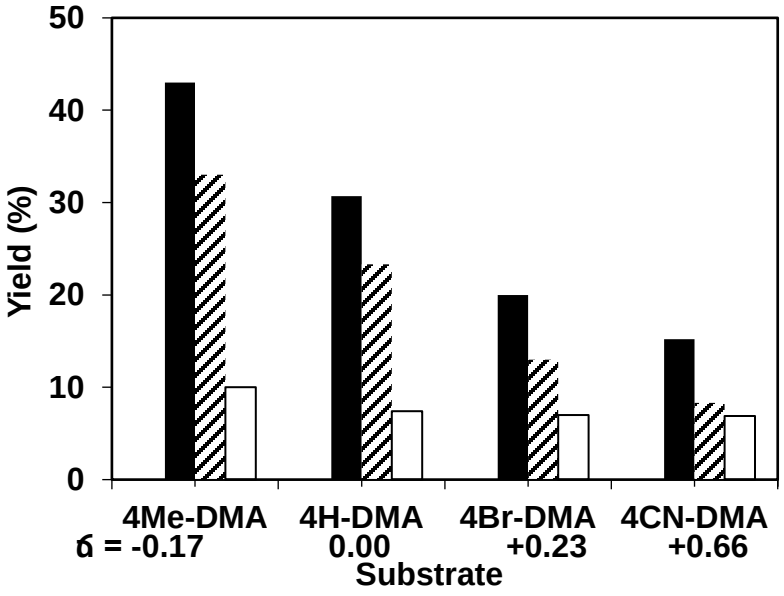

Figure 44. Comparison of the product formation in the oxidation of *p*-substituted *N,N*-dimethylanilines, $[Mn^{II}]_0$ = 3 mM, $[S]_0$ = 300 mM, $[Ox]_0$ = 300 mM, substituted *N,N*-dimethylanilines to *N*-methyl aniline (line column), *N*-methylformanilide (white column) and total yield (black column) derivatives with TBHP in CH_3CN at 30 °C (Table S13)

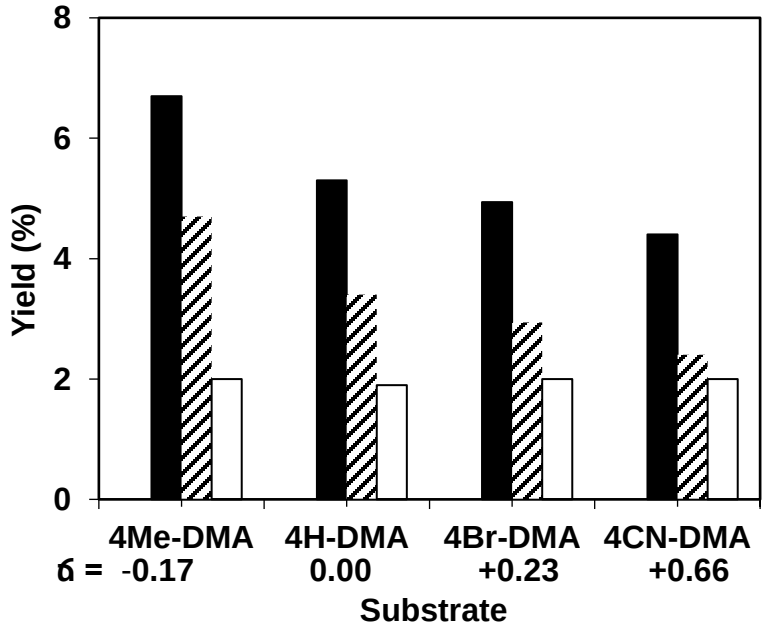

Figure 45. Comparison of the product formation in the oxidation of *p*-substituted *N,N*-dimethylanilines, $[Mn^{II}]_0$ = 3 mM, $[S]_0$ = 300 mM, $[Ox]_0$ = 300 mM, of substituted *N,N*-dimethylanilines to *N*-methyl aniline (line column), *N*-methylformanilide (white column) and total yield (black column) derivatives with H_2O_2 in CH_3CN at 30 °C (Table S13)

4.11 Catalytic oxidation of *N,N*-dimethylanilines under argon

Reactions were carried out under standard catalytic conditions in acetonitrile at 30 °C under an argon atmosphere (Scheme 17). Co-oxidants were added by syringe, and the excess of DMA was used to minimize the over oxidized products. The catalytic oxidation of *N,N*-dimethylaniline (DMA) with *meta*-chloro perbenzoic acid (*m*-CPBA), peracetic acid (PAA), hydrogen peroxide (H_2O_2), *tert*-butyl hydroperoxide (TBHP), and iodosobenzene (PhIO), by nonheme $[Mn^{II}(asN4Py)(CH_3CN)](CF_3SO_3)_2$ under air and argon atmosphere were also investigated.

The main products observed under air atmosphere were *N*-methylaniline (MA) and *N*-methylformanilide (MFA) while the argon atmosphere yielded *N*-methylaniline (MA) as a predominant product (Figure 46).

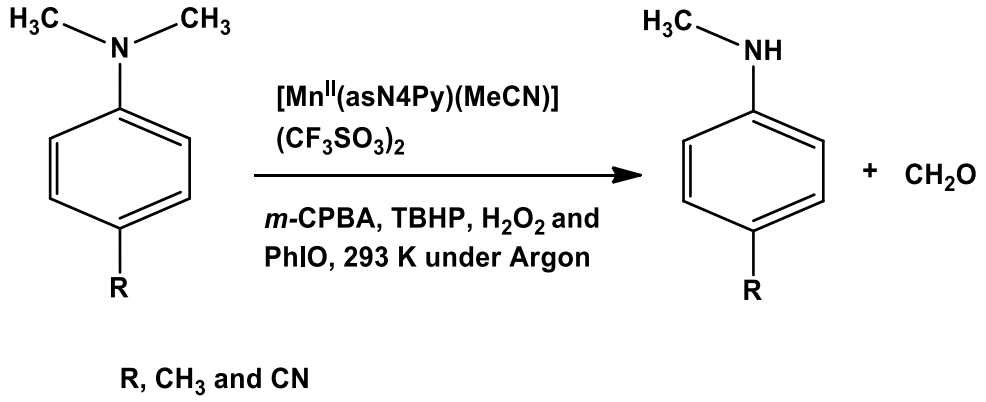

Scheme 17. Catalytic oxidation of *N,N*-dimethylaniline (DMA) by $[Mn^{II}(asN4Py)(CH_3CN)](CF_3SO_3)_2$ under argon atmosphere

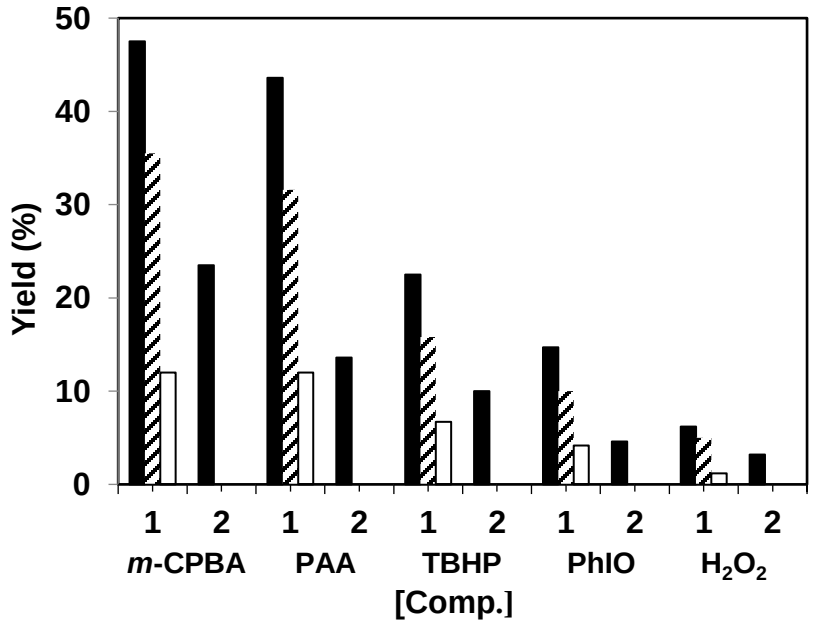

Figure 46. Comparison of the product formation the $[[Mn^{II}(asN4Py)(CH_3CN)](CF_3SO_3)_2]_0$ = 3 mM, $[S]_0$ = 300 mM, $[Ox]_0$ = 300 mM, oxidation of *N*,*N*-dimethyl-aniline to *N*-methyl aniline (line column), *N*-methylformanilide (white column) and (black column) total yield various co-oxidants in CH_3CN at 30 °C, under argon (Table S14 and 15)

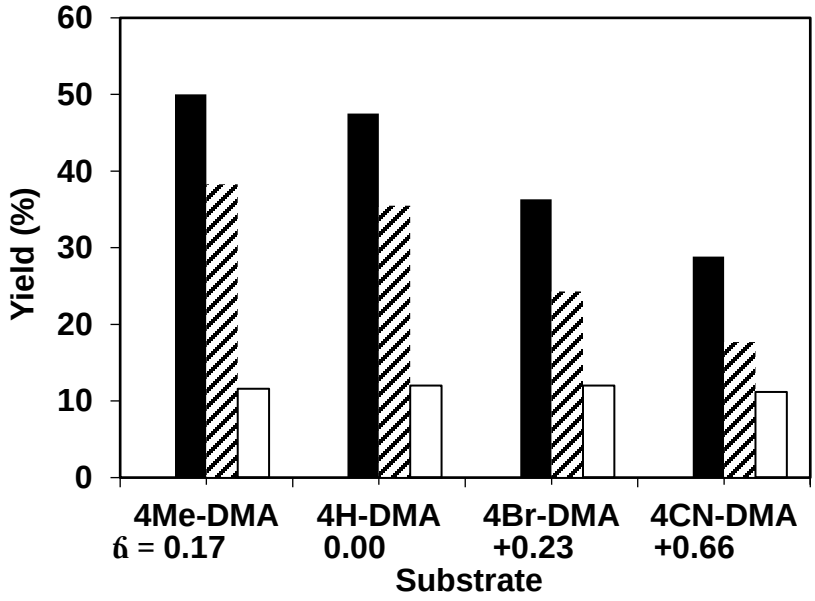

Figure 47. Comparison of the product formation in the oxidation of *p*-substituted *N*, *N*-dimethylanilines, $[[Mn^{II}(asN4Py)(CH_3CN)](CF_3SO_3)_2]_0$ = 3 mM, $[S]_0$ = 300 mM, $[Ox]_0$ = 300 mM oxidation of substituted *N*,*N*-dimethylanilines to *N*-methyl aniline (line column), *N*-methylformanilide (white column) and (black column) total yield derivatives with *m*-CPBA in CH_3CN at 30 °C under air (Table S15)

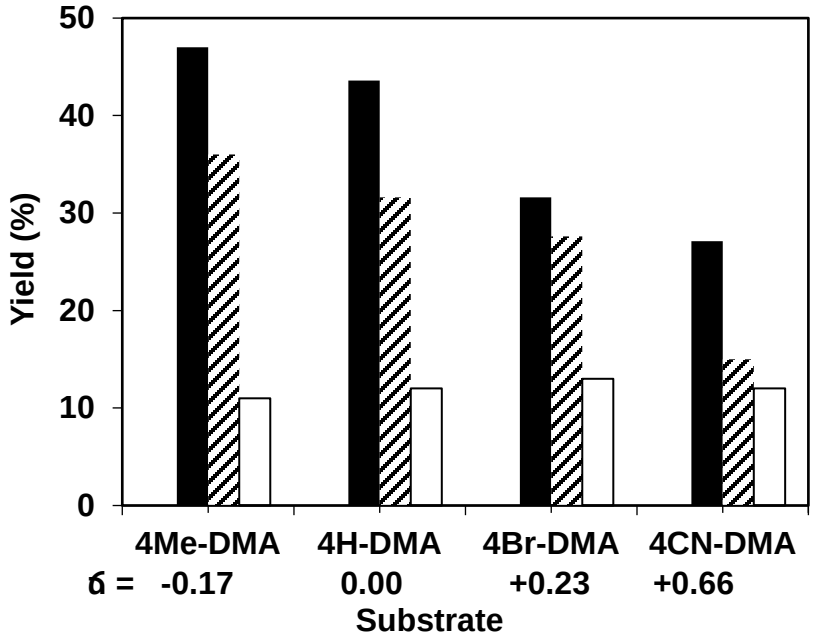

Figure 48. Comparison of the product formation in the oxidation of *p*-substituted *N*,*N*-dimethylanilines, $[[Mn^{II}(asN4Py)(CH_3CN)](CF_3SO_3)_2]_0$ = 3 mM, $[S]_0$ = 300 mM, $[Ox]_0$ = 300 mM, oxidation of substituted *N*, *N*-dimethylanilines to *N*-methyl aniline (line column), *N*-methylformanilide (white column) and (black column) total yield derivatives with PAA in CH_3CN at 30 °C under air (Table S13).

Efforts have been made to work out efficient and selective manganese-isoindoline (**3-8**) complexes catalyzed *N*-demethylation reactions were carried out under standard catalytic conditions (1: 300: 300 for the catalyst: DMA: co-oxidant) in acetonitrile at 30 °C under air (Ar). Co-oxidants were added by syringe, and the excess of DMA was used to minimize the over oxidized products. The catalytic activity and selectivity for complexes **(3-8)** are shown in (Table S19, figure 49). Good correlation was established between Log (TOF) with $E^o_{1/2}$ (mV vs SCE) for the Mn^{II} complexes (3-8) (figure 50).

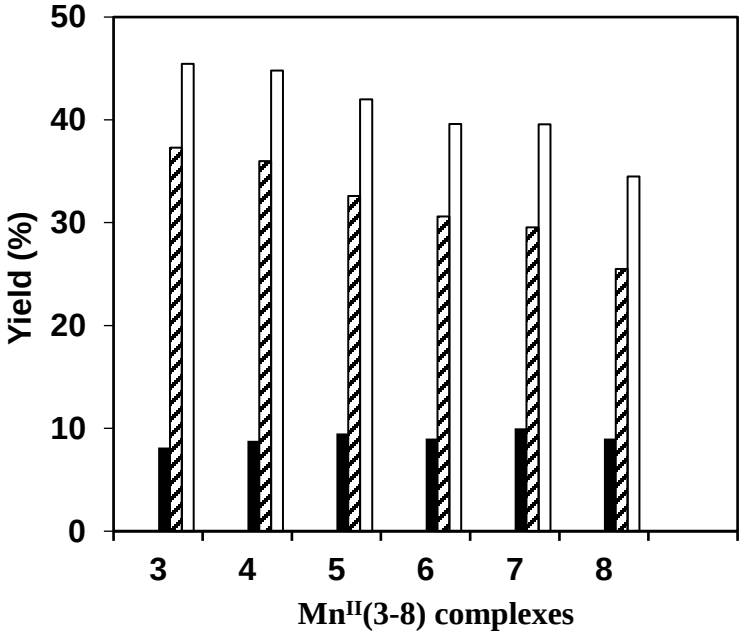

Figure 49. Comparison of the product formation in the manganese catalyzed $[Mn^{II}]_0$ = 3 mM, $[S]_0$ = 300 mM, $[Ox]_0$ = 300 mM, $[Mn(py)_2\text{-ind}]^{2+}$**,** *N*-methyl aniline (line column), *N*-methylformanilide (black column) and total yield (white column) with *m*-CPBA co-oxidants in CH_3CN (Table S19).

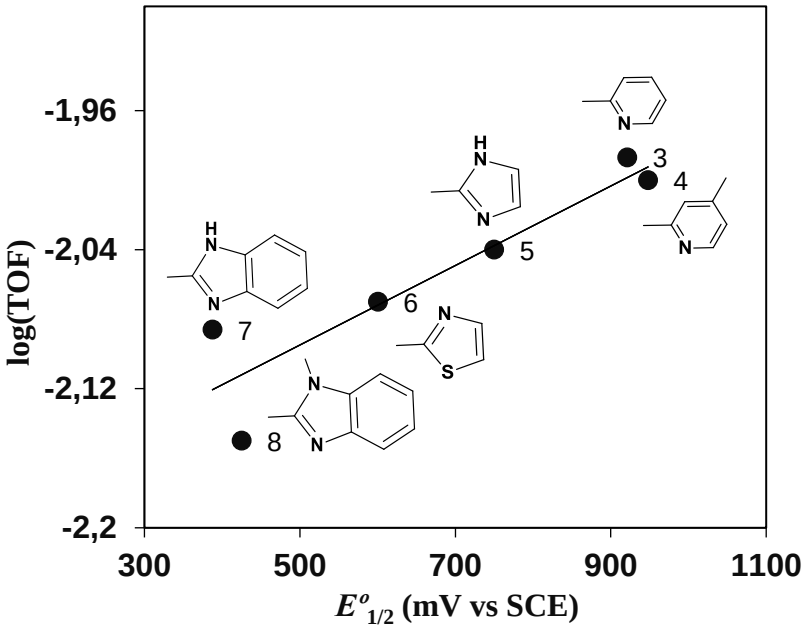

Figure 50. Established linear correlation between yield with $E^o_{1/2}$ (mV vs SCE) for the Mn^{II} complexes (3-8)

Based on previous catalytic results above, it can be expected that the *N*-demethylation reaction is sensitive to the nature of the substituent in the phenyl ring of DMAs. Upon using *p*-substituted DMA derivatives with electron-donating groups the rate of the reactions was increased remarkably. The good correlation was established between MA/MAF and $E°_{ox}$, and $E°\sigma_p$ with co-oxidant of *m*-CPBA and PAA, (Figure 51 and 52, Table S17).

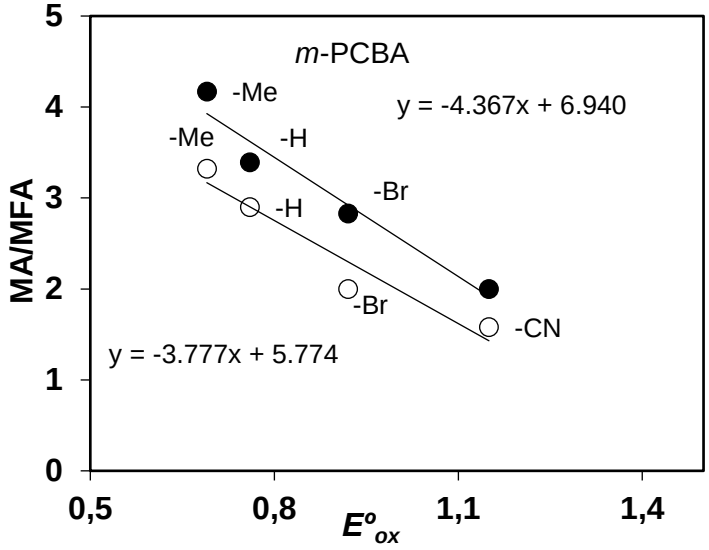

Figure 51. The plot of MA to MFA ratio against the $\boldsymbol{E}^{\circ}_{ox}$ of *p*-substituted DMAs $[Mn^{II}(asN4Py)(CH_3CN)](CF_3SO_3)_2$ (○) and $[Mn^{II}\{(Py)_2\text{-indH}\}(Cl)_2]$ (●)

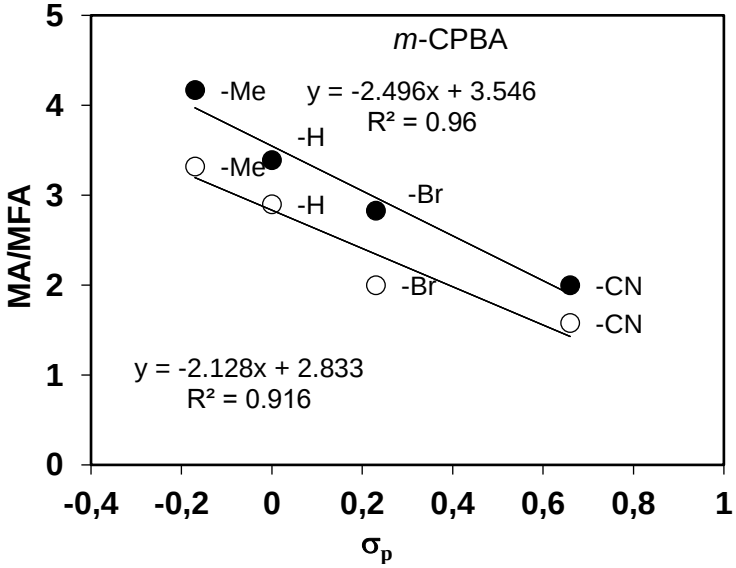

Figure 52. The plot of MA to MFA ratio against the σ_p of *p*-substituted DMAs$[Mn^{II}(asN4Py)(CH_3CN)](CF_3SO_3)_2$ (○) and $[Mn^{II}\{(Py)_2\text{-indH}\}(Cl)_2]$ (●)

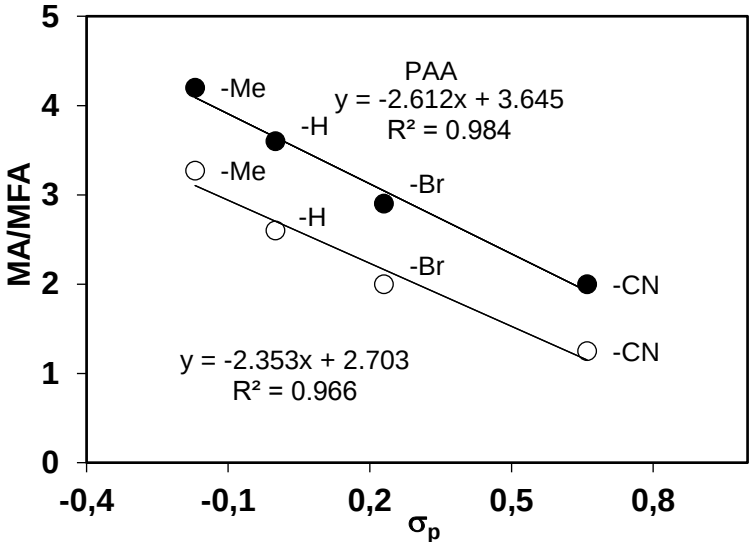

Figure 53. Reactions of $[Mn^{II}(asN4Py)(CH_3CN)](CF_3SO_3)_2$ (O) and $[Mn^{II}\{(Py)_2\text{-}indH\}(Cl)_2]$ (●) with DMAs by the use of PAA in CH_3CN at 30 °C. The plot of MA to MFA ratio against the σ_p of *p*-substituted DMAs (Table S18).

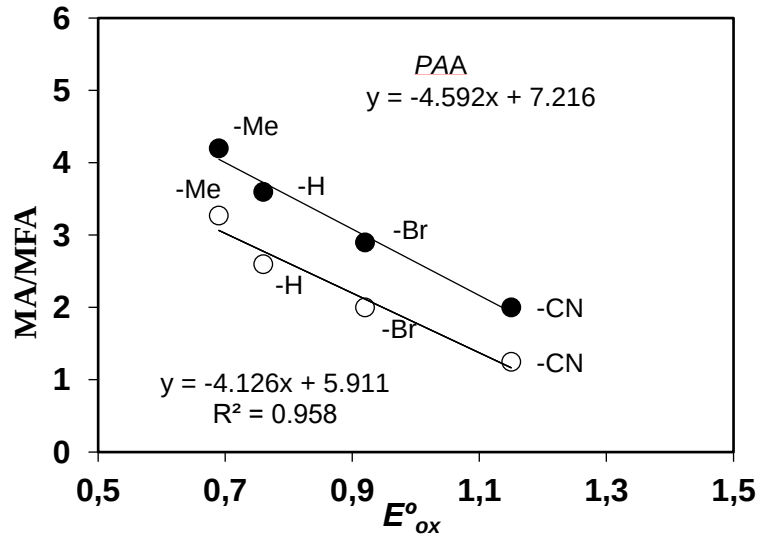

Figure 54. Reactions of $[Mn^{II}(asN4Py)(CH_3CN)](CF_3SO_3)_2$ (O) and $[Mn(py)_2\text{-}indH]^{2+}$ (●) with DMAs by the use of PAA in CH_3CN at 30 °C, Plot of MA to MFA ratio against the $\boldsymbol{E}^{\circ}_{ox}$ of *p*-substituted DMAs (Table S18).

The complex of $[Mn^{II}(asN4Py)(CH_3CN)](CF_3SO_3)_2$ was used to trap intermediate of $Mn^{IV}O$ and proposed mechanism for the reaction, pentdentate more stable compared to tridentate $[Mn(py)_2indH]^{2+}$

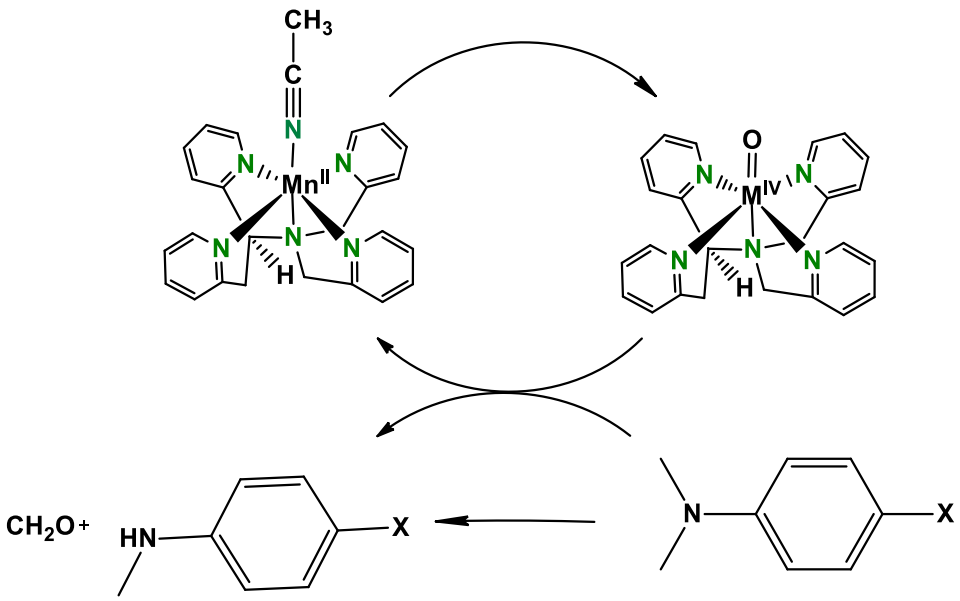

Scheme 18. Reactions of $[Mn^{II}(asN4Py)(CH_3CN)](CF_3SO_3)_2$ with DMAs by the use of *m*-CPBA in CH_3CN at 30 °C

The UV-Vis in the presence of DMA under the standard catalytic conditions (complex/ experiments *m*-CPBA/DMA = 1: 100: 100) have confirmed the formation of $Mn^{IV}O$ species, the intermediate species undergoes a decay which is affected by the substrate DMA (Figure 55), $[(asN4Py)Mn^{IV}(O)]^{2+}$ the intermediate $DMA^{\bullet}$ resulting from an electron-transfer process, the addition of a p-Me-DMA to a deaerated CF_3CH_2OH–MeCN (1:1 v/v) solution of complex resulted in the immediate generation of a transient absorption band at λ_{max} = 460 nm (Figure 55).

The absorption band was identical to that of the p-Me-DMA^+, given by the reaction of the *p*-Me-DMA absorption band of *p*-Me-DMA^+ appears, accompanied by a decrease in the absorption band at 994 nm due to electron-transfer from *p*-Me-DMA to complex proceeds via fast electron-transfer from DMA to $[(asN4Py)Mn^{IV}(O)]^{2+}$ to produce p-Me-DMA^+, followed by slower proton transfer from p-Me-DMA^+ to $[(Bn\text{-}TPEN)Mn^{III}(O)]^+$ [178] and the new intense absorption in the range of 650 nm indicates a complexation and charge-transfer (CT) type interaction between the oxidant and the substrate, albeit their nature is not known.

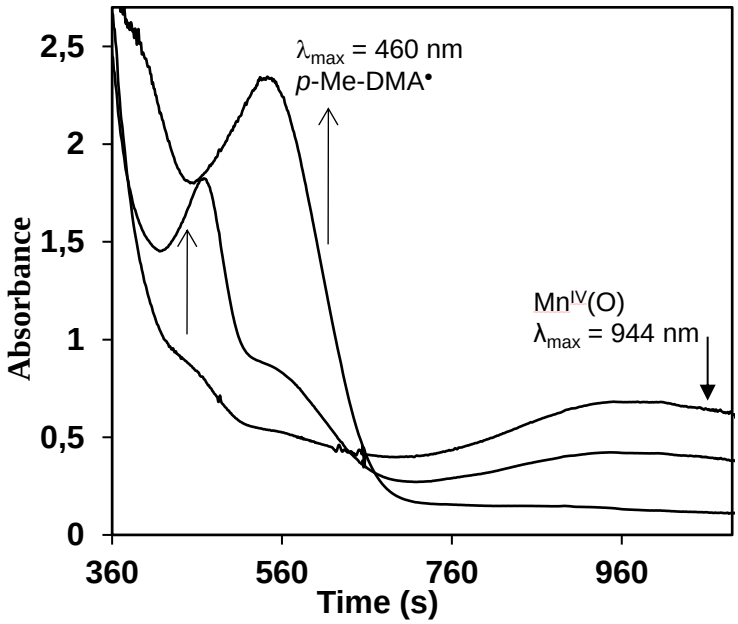

Figure 55. The UV-Vis spectral changes in the reaction of $[[Mn^{II}(asN4Py)(CH_3CN)](CF_3SO_3)_2]_0 = 1\times10^{-4}$ M, and $[p\text{-Me-DMA}]_0 = 3\times10^{-3}$ M, in CF_3CH_2OH-MeCN (1:1 v/v) at 283 K

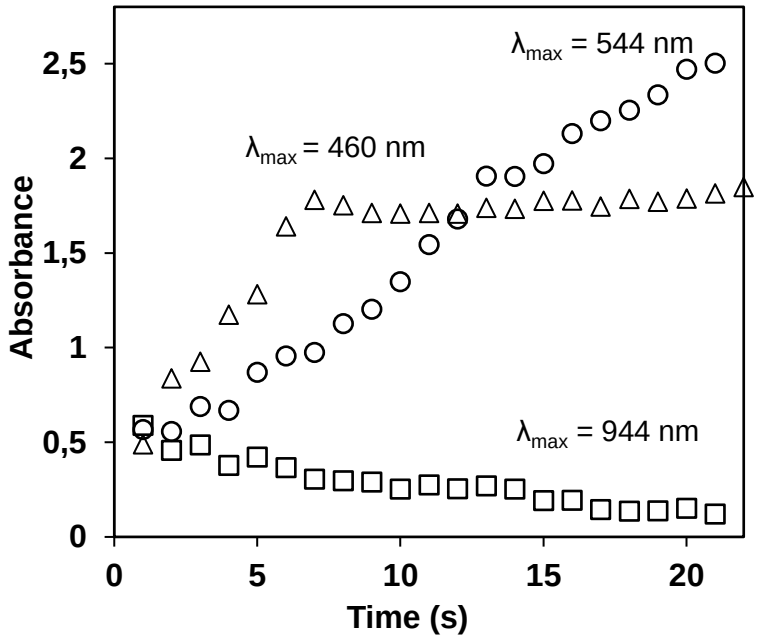

Figure 56. The time course of the decay of *p*-Me-DMA• monitored at 944 nm. $[[Mn^{II}(asN4Py)(CH_3CN)](CF_3SO_3)_2]_0 = 1\times10^{-4}$ M, and $[p\text{-Me-DMA}]_0 = 3\times10^{-3}$ M, in CF_3CH_2OH-MeCN (1:1 v/v) at 283 K

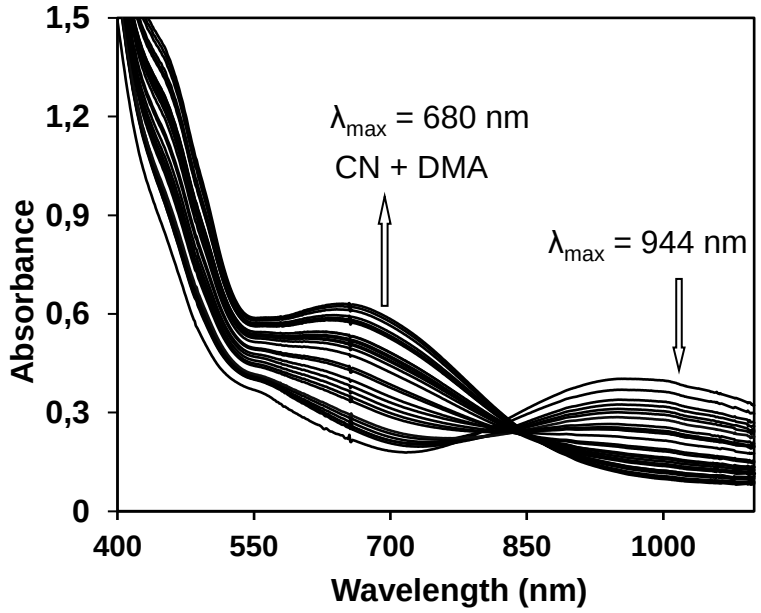

Figure 57. The UV-Vis spectral changes in the reaction of $[[Mn^{II}(asN4Py)(CH_3CN)](CF_3SO_3)_2]_0 = 1\times10^{-4}$ M, and $[p\text{-CN-DMA}]_0 = 3\times10^{-3}$ M in CF_3CH_2OH-MeCN (1:1 v/v) at 283K

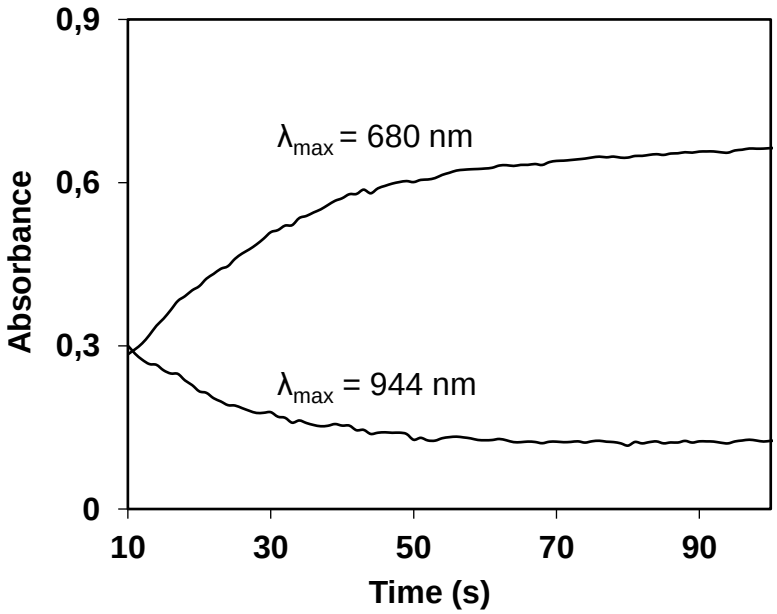

Figure 58. Time profiles of the absorbance of *p*-CN-DMA at 680 nm and $[(asN4Py)Mn^{IV}(O)]^{2+}$ at 1040 nm

Efforts have been made to work out efficient and selective Mn^{II} catalyzed *N*-demethylation reactions by the use of various co-oxidants such as PhIO, *m*-CPBA, PAA, TBHP and H_2O_2, as well as their detailed mechanistic aspects. Based on experimental observations derived from the catalytic experiments the following mechanisms can be proposed (Scheme 19). In the peracid and PhIO based systems, the formation of manganese(IV)-oxo can be explained by direct oxygen atom transfer from the co-oxidant to the Mn(II) precursor: Mn^{II} + PhIO (*m*-CPBA) = $Mn^{IV}O$ + PhI (*m*-CPBA). In the former, a clearly metal-based process only the mangane(IV)-oxo is responsible for the *N*-methylation reaction via ET-PT mechanism with a rate-determining PT step (Path a in scheme 19), but in the latter case, the reaction can be explained by the parallel selective metal-based and non-selective radical processes (Path a + b in Scheme 19) [179].

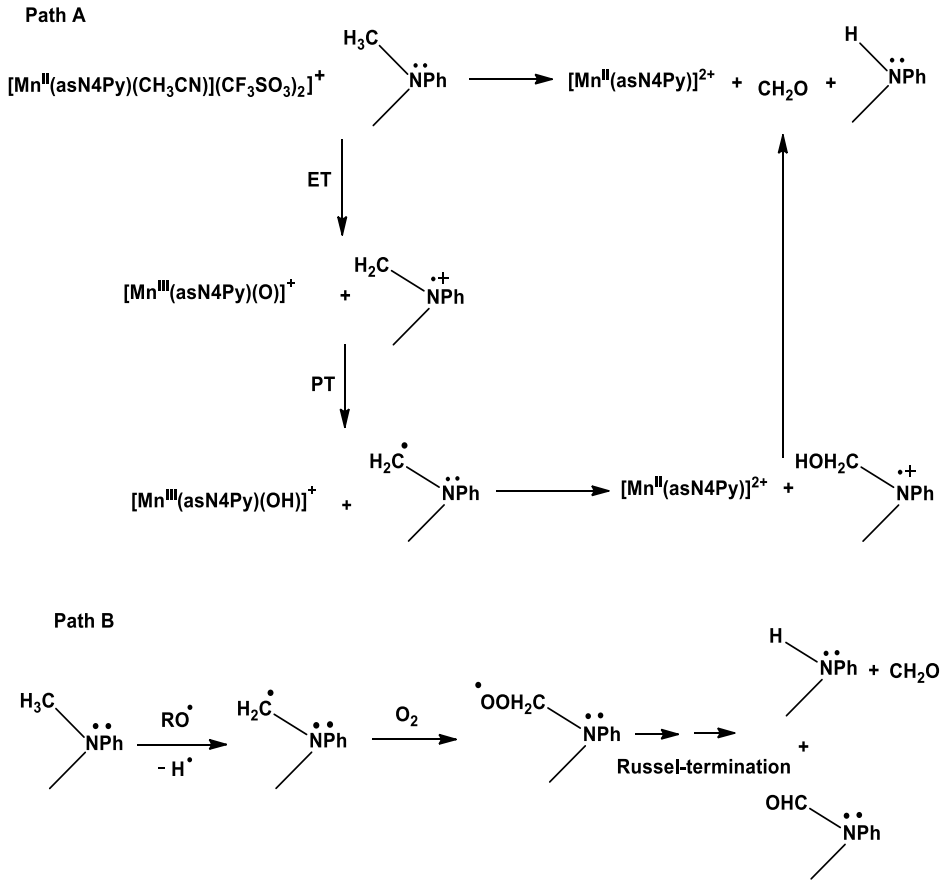

Scheme 19. Proposed (ET-PT) mechanism in the Mn^{II} Catalyzed *N*-demethylation reaction

Non-heme Mn(II) complexes, $[Mn^{II}(HL^3)\ Cl_2]$ (3), $[Mn^{II}(asN_4Py)(CH_3CN)](ClO_4)_2$ and $Mn(ClO_4)_2$ salt has been shown to catalyze the oxidation of *N*,*N*-dimethylaniline (DMA). The order of efficacy for the co-oxidants was found to be *m*-CPBA > PAA > TBHP > PhIO > H_2O_2 in the presence of the Mn(II) catalyst, the main products observed under air atmosphere were *N*-methylaniline (MA) and *N*-methyl-formanilide (MFA) while the argon atmosphere yielded *N*-methylaniline (MA) as predominant product, which can be explained by the different mechanism of the Mn(IV)-oxo formation and the presence or absence of hydroxyl (tert-butoxy) radicals. Mechanisms were proposed based on experimental observations derived from the catalytic experiments.

5 Summary

The reaction of high-valent oxygen intermediates in mononuclear non-heme iron (NHFe) enzymes is a challenging task because of their transient nature and practical difficulties in trapping them. Such stable synthetic analogues of the iron(IV)-oxo intermediates have proven to be valuable in studying the geometric and electronic structures of the iron(IV)-oxo unit and how it is activated to perform H-atom abstraction in the initial step of most mechanistic pathways. The $[Fe^{II}(asN4Py)]$-$(CF_3SO_3)_2$ complex has been an active and selective catalyst for the oxidation of cis-cyclooctene and substituted styrene derivatives at room temperature to give epoxides as the main products, The oxidation of styrene yielded 65% epoxide and 12% benzaldehyde, and cis-cyclooctene oxidation produced 75% cyclooctene oxide and 7% cyclooct-2-enone.

Activation parameters of *cis*-cyclooctene oxidation, ΔH = 38 kJ mol^{-1}, ΔS = -180 J mol^{-1} K^{-1} (at 298 K), and styrene, ΔH = 70.6 kJ mol^{-1}, ΔS = -76 J mol^{-1} K^{-1} at 298 K The activation enthalpy of 71 kJ mol^{-1} for the $[Fe^{IV}(asN4Py)(O)]^{2+}$ mediated epoxidation of styrene is roughly the same with that presented for $[Fe^{IV}(N3S2)(O)]^{2+}$ linear correlation between the relative rate and the TE for the iron(IV)-oxo mediated oxidation of *p*-substituted styrenes is established.

Stoichiometric oxidation of 4-chlorostyrene and styrene by (-)-$Fe^{IV}(asN4Py)$-$(O)]^{2+}$ (**2b**) gave a 12% of 4-chlorostyrene oxide and 8% enantiomeric excess of styrene oxide, even though the asymmetric induction is not impressive when compared with other published studies. Because of the selectivity loss, the concerted [2+1] and [2+2] cycloaddition mechanisms can be excluded (A and B). The moderate enantioselectivities for the oxidation of styrene derivatives (8-12% ee) can be elucidated by the rotation/collapse processes through C-C bond of the radicalized species prior to the epoxide ring closure. Catalytic oxidation of ethylbenzene by $[Fe^{IV}(asN4Py)(O)]^{2+}$ in CH_3CN at 0 °C, yielded 33 % enantiomeric excess (ee) of 1-phenylethanol after 90 minutes, and 25 % enantiomeric excess after 180 minutes under argon atmosphere.

The oxidation of ethylbenzene by the chiral iron(IV)-oxo intermediate achieves moderate enantioselectivities have been observed for the catalytic oxidation of ethylbenzene, which can be explained by the parallel enantioselective metal-based, iron(IV)-oxo mediated and nonselective Fenton-type radical processes. Efforts have been made to develop a highly efficient asymmetric catalyzed oxidation of various alkanes by introducing the chiral moiety to ligands as well as their detailed mechanistic aspects.

Manganese-isoindoline complexes such as, $[Mn^{II}(HL^{3})Cl_2]$ (3), $[Mn^{II}(HL^{4})Cl_2]$ (4), $[Mn^{II}(HL^{5})Cl_2]$ (5), $[Mn^{II}(HL^{6})Cl_2]$ (6), $[Mn^{II}(HL^{7})Cl_2]$ (7) and $[Mn^{II}(HL^{8})Cl_2]$ (8) Synthesized and characterized by various electrochemical and spectroscopic methods. Efforts have been made to work out highly efficient and highly selective manganese-based catalytic system for the disproportionation reaction of H_2O_2 as synthetic catalase mimics and the oxidation of morin as oxidative bleaching performances. After that, investigated the effect of the ligand modification by varying the aryl substituent on the bis-iminoisoindoline moiety with emphasis on the redox potential. We observed that the higher the redox potentials of Mn^{III}/Mn^{II} redox couple the higher is the catalase-like and bleaching activity. It is also worth to note that the bicarbonate concentration plays an important role in both the catalase-like reaction and bleaching process, probably during the formation of the proposed catalytically active $Mn^{IV}(O)$ species.

Non-heme Mn(II) complexes, $[Mn^{II}(HL^{3})Cl_2]$ (**3**), $[Mn^{II}(asN_4Py)(CH_3CN)](ClO_4)_2$ and $Mn^{II}(ClO_4)_2$ salt have been shown to catalyze the oxidation of *N*,*N*-dimethylaniline (DMA) with H_2O_2, *tert*-butyl hydroperoxide (TBHP), peracetic acid (PAA), *meta*-chloro peroxybenzoic acid (*m*-CPBA) and PhIO, resulting *N*-methylaniline (MA) as the predominant product with *N*-methylformanilide (MFA) as a result of a free-radical chain process.

Where the product composition (MA/MFA) remarkably influenced by the electron density on the substrate, especially in the $[Mn^{II}\{(Py)_2\text{-indH}\}(Cl)_2]$/*m*-CPBA system, and by the co-oxidants used. No formation of MFA occurred when the oxidation of DMA was carried out in the presence of $Mn^{II}(asN_4Py)(CH_3CN)](ClO_4)_2$ with PhIO as co-oxidants under argon atmosphere.

Based on the spectral investigation (UV/Vis) of reaction systems above, manganese(IV)-oxo intermediate, $[Mn^{IV}(asN4Py)(O)]^{2+}$ has been suggested to be the key active species of the *N*-dealkylation reaction in all catalytic systems. The manganese(IV)-oxo species in the presence of DMA, λ_{max}, 944 nm, and the new intense absorption in the range of 460 nm indicate a complexation and charge-transfer (CT) type interactions between the oxidant and substrate.

6 Experimental part

Instrumentation

The UV-visible spectra were recorded on an Agilent 8453 diode-array spectrophotometer using quartz cells.

IR spectra were recorded using a Thermo Nicolet Avatar 330 FT-IR instrument (Thermo Nicolet Corporation, Madison), samples were prepared in the form of KBr pellets.

GC analyses were performed on an Agilent 6850 gas chromatograph equipped with a flame ionization detector and a 30 m SUPELCO BETA DEX□225 columns.

The NMR spectrum was recorded on a Bruker Avance 400 spectrometer (Bruker Biospin AG, Fällanden, Switzerland).

GC-MS analyses were carried out on Shimadzu QP2010SE equipped with a secondary electron multiplier detector with conversion dynode and a 30 m HP5MS column.

Microanalyses elemental analysis was done by the Microanalytical Service of the University of Pannonia.

Analytical and physical measurements

Infrared spectra were recorded on an Avatar 330 FT-IR Thermo Nicolet instrument using samples mulled in KBr pellets. UV–vis spectra were recorded on an Agilent 8453 diode -array spectrophotometer using quartz cells. Microanalyses were done by the Microanalytical Service of the University of Pannonia. Cyclic voltammograms (CV) were taken on a Volta Lab 10 potentiostat with Volta Master 4 software for data process. The electrodes were as follows: glassy carbon (working), Pt wire (auxiliary), and Ag/AgCl with 3M KCl (reference). The potentials E^{0} Mn/Mn vs. Saturated Calomel Electrode (SCE) was also determined experimentally to be 100 ± 5 mV. All manipulations were performed under a pure argon atmosphere using standard Schlenk-type inert-gas techniques. Solvents used for the reactions were purified by literature methods and stored under argon.

The starting materials for the ligand are commercially available and they were purchased from Sigma Aldrich. $[Fe^{II}(asN4Py)(CH_3CN)](ClO_4)_2$ and asN4Py (asN4Py = *N*,*N*-bis(2-pyridylmethyl)-1,2-di(2-pyridyl)ethylamine) were prepared as previously described [102, 180].

The ligands 1,3-bis(2′-pyridylimino)isoindoline (HL^3), 1,3-bis(4′-methyl-2′-pyridylimino)isoindoline (HL^4), 1,3-bis(2′-imidazolylimino)isoindoline (HL^5), 1,3-bis(2′-tiazolylimino)isoindoline (HL^6), 1,3-bis(2′-benzimidazolylimino)isoindoline (HL^7), and 1,3-bis(N-methylbenzimidazolylimino)isoindoline (HL^8), and the complexes Mn^{II} (3-8) were synthesized according to published procedures [127, 154].

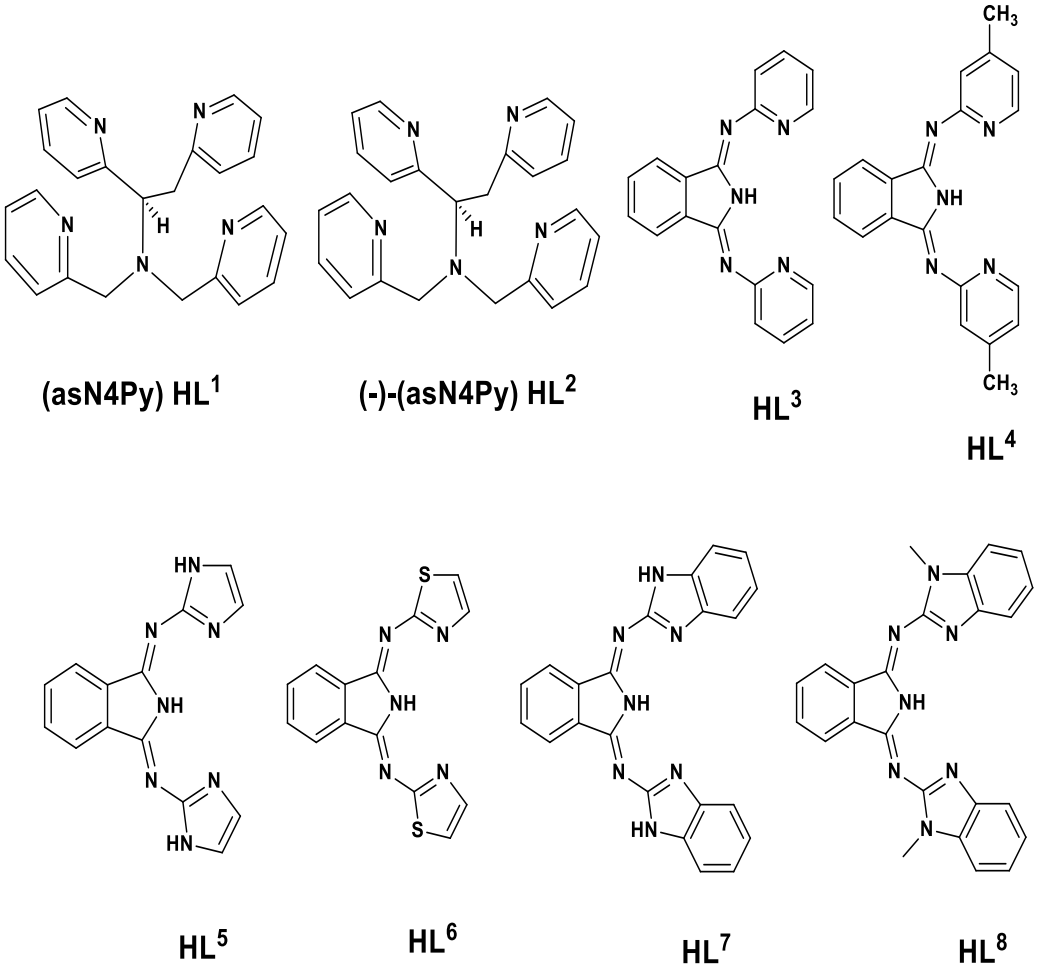

Scheme 1. Ligands were synthesized according to the published procedure

Synthesis of [Mn^{II}{(4-Me-Py)$_2$-indH}$(Cl)_2$]

A solution of (0.59 gm, 3 mmol) of $MnCl_2.4H_2O$ in 10 ml of methanol was added to a solution of (0.95 gm, 3 mmol) (N-Me-bim)$_2$-indH in 10 ml acetonitrile then the yellow suspension was refluxed for 6 hours, then the solvent removed by evaporation and the crude product was washed with cold methanol. UV-vis [dmf] [λ_{max}, nm logε/dm^3 mol^{-1} cm^{-1}], 227 (4.26), 296 (4.22), 330 (4.19), 347 (4.21), 367 (4.28), 386 (4.37), 409 (4.14), 453 (3.32). FT-IR bands (KBr pellet cm^{-1}): 3444 w, 3239 w, 3039 w, 2953 w, 2847 w, 1654 w, 1634 s, 1597 m, 1517 m, 1491 s, 1356 w, 1209 m, 1066 m, 939 m, 829 w, 719 m, 453 m. Anal Calcd for $C_{20}H_{17}C_{l2}MnN_5$: C, 53.00; H, 3.78; N, 15.45. Found: C, 53.02; H, 3.80; N, 15.48.

Synthesis of (im)$_2$-indH

A mixture of 10.81 mmoles (1.57 g) of 1,3-diiminoisoindoline and 22.70 mmoles (3.00 g) of 2-amino-imidazole sulfate in 25 ml of 1-butanol with sodium carbonate. The solution was heated with stirring at reflux for 20 hours. The reaction mixture was cooled, filtered, and the solid part obtained was washed with distilled water and cold methanol. The crude product was recrystallized from methanol to yield 0.919 g (30 %) of brownish-red crystals. UV-vis [dmf], [λ_{max}, nm logε/dm^3 mol^{-1} cm^{-1}], 199 (4.93), 244 (4.73), 330 (4.32). FT-IR bands (KBr pellet cm^{-1}), 3289 w, 3215 w, 3156 w, 3107 w, 2872 w, 1642 s, 1567 s, 1499 m, 1452 m, 1382 w, 1324 w, 1274 s, 1160 m, 1033 m, 753 m, 689 m, 641 m, 574 w, 517 w. Anal Calcd for $C_{40}H_{37}F_6FeN_6O_{10}S_2$: C, 48.25; H, 3.75; N, 8.45. Found: C, 48.22; H, 3.72; N, 8.47. ^{1}H-NMR (DMSO-d$_6$), δ (ppm): 5.75 (s, 1 H); 7.10 (m, 4H); 7.70 (m, 2H); 7.90 (m, 2H); 12.50 (s, 2H). ^{13}C-NMR (DMSO-d$_6$), δ (ppm): 121.9 (2C); 123.5; 130.3; 131.9; 132.3; 134; 134.5; 136.3; 149.2 (2C); 150.2 (2C); 167.5.

Synthesis of [Mn^{II}{$(im)_2$-indH}$(Cl)_2$]

A solution of 0.14 g (0.72 mmol) of $MnCl_2$ $4H_2O$ in 2.5 cm^3 CH_3OH was added to a suspension of 0.20 g (0.72 mmol) $(im)_2$-indH in 2.5 cm^3 CH_3CN and the brown suspension was refluxed for 6 hours. The solvent was removed by evaporation and the crude product was washed with cold CH_3OH and diethyl ether, and then dried under vacuum (0.16 g, 53%). UV-vis [dmf], [λ_{max}, nm logε/dm^3 mol^{-1} cm^{-1}], 289 (3.73), 361 (4.13), 402 (3.95), 431 (3.54), 460 (3.30). FT-IR bands (KBr pellet cm^{-1}): 3382 w, 3253 w, 3100 w, 2920 w, 2847 w, 1657 s, 1614 s, 1469 m, 1361 w, 1311 w, 1254 w, 1092 m, 1048 m, 780 m, 709 m, 694 m, 530 w. Anal Calcd for $C_{14}H_{11}Cl_2MnN_7$: C, 41.71; H, 2.75; N, 24.32. Found: C, 41.66; H, 2.72; N, 24.35.

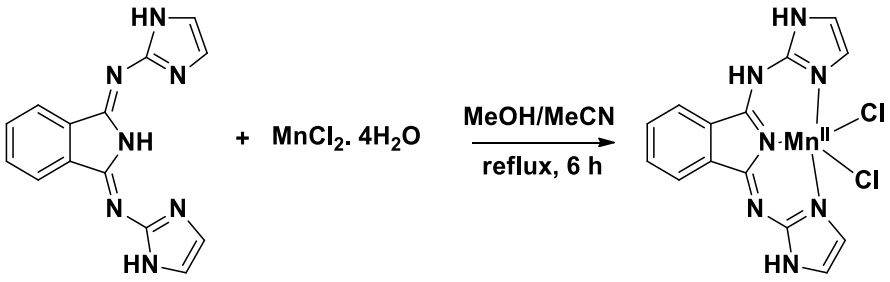

Chemical Formula: $C_{14}H_{11}N_7$
Molecular Weight: 277.29

Chemical Formula: $C_{14}H_{11}Cl_2MnN_7$
Molecular Weight: 403.13

Synthesis of [Mn^{II}{$(N\text{-}Me\text{-}bim)_2$-indH}$(Cl)_2$]

A solution of (0.59 gm, 3 mmol) of $MnCl_2.4H_2O$ in 10 ml of methanol was added to a suspension of (1.13 gm, 2.12 mmol) $(N\text{-}Me\text{-}bim)_2$-indH in 10 ml acetonitrile then refluxed for 6 hours, then the solvent removed by evaporation and the crude product was washed with cold methanol. UV-vis [dmf], [λ_{max}, nm logε/dm^3 mol^{-1} cm^{-1}]: 362 (3.94), 371 (4.02), 382 (4.00), 420 (3.91), 448 (3.94), 482 (3.75), 535 (2.93). Ft-IR bands (KBr pellet cm^{-1}): 3427 w, 3043 w, 2925 w, 1629 s, 1613 s, 1552 s, 1499 m, 1475 m, 1290 m, 1180 m, 1090 m, 1066 m, 735 s, 706 m, 543 w. Anal Calcd for $C_{24}H_{19}C_{l2}MnN_7$: C, 54.26; H, 3.60; N, 18.45. Found: C, 54.24; H, 3.57; N, 18.43.

Synthesis of [Mn^{II}{$(tia)_2$-indH}$(Cl)_2$]

A solution of (0.24 gm, 1.215 mmol) of $MnCl_2.4H_2O$ in 10 ml of methanol add to suspension of (0.378 gm, 1.215 mmol) $(tia)_2$-indH in 10 ml acetonitrile then refluxed for 6 hours, then solvent removed by evaporation and crude product was washed with cold methanol. UV-vis [dmf], [λ_{max}, nm logε/dm^3 mol^{-1} cm^{-1}]: 287 (4.22), 373 (4.29), 396 (4.39), 419 (4.44), 448 (4.22). FT-IR bands (KBr pellet cm^{-1}): 3423 w, 3199 w, 3105 w, 3084 w, 1622 s, 1504 s, 1364 m, 1291 m, 1213 m, 1123 m, 1099 m, 1052 m, 874 m, 772 m, 702 m, 624 w, 526 w. Anal Calcd for $C_{14}H_9C_{l2}$ MnN_5S_2: C, 38.46; H, 2.07; N, 16.02. Found: C, 38.45; H, 2.05; N, 16.03.

Catalase-like activity

All reactions were carried out at 21 ºC in a reactor containing a stirring bar under air. The stoichiometry of the reaction was measured by simultaneous determination of the amount of O_2 and H_2O_2 concentrations. The evolved dioxygen was measured volumetrically. In a typical experiment, aqueous solutions carbonate buffer at pH 9.6 (20 cm^3), was added to the complex (0.211 mmol) and the flask was closed with a rubber septum, hydrogen peroxide (0.447 mol) was injected through the septum with a syringe. The reactor was connected to a graduated burette filled with oil and dioxygen evolution was measured volumetrically at time intervals of 15 (s). Observed initial rates were expressed by taking the volume of the solution (20 cm^3) into account and calculated from the maximum slope of the curve describing the evolution of O_2 versus time.

Degradations of morin by co-oxidant of H_2O_2

Catalytic runs of morin oxidation in the presence of the complexes were performed in 2 ml optical quartz cells. The reactions were carried out in a carbonate buffer at pH 10. A freshly prepared morin solution in DMF was diluted with buffer to result in morin solutions with a concentration of 0.16 mM for all experiments. To this mixture, the desired amount of catalyst solution was added.

The required amount of H_2O_2 solution was added to start the catalytic oxidation of morin. The temperature was kept at 25 ± 1 °C during the 10min reaction time. The reaction was followed by detecting the change in the absorption maximum of morin at 410 nm.

Degradations of morin by air

Catalytic runs of morin oxidation in the presence of the complexes were performed in 2 ml optical quartz cells. The reactions were carried out in a carbonate buffer at pH 10. A freshly prepared morin solution in DMF was diluted with buffer to result in morin solutions with a concentration of 0.16 mM for all experiments. To this mixture, 1.6 μM of the catalyst was added to a solution. The temperature was kept at 25 ± 1 °C during the 10 min reaction time. The reaction was followed by detecting the change in the absorption maximum of morin at 407 nm.

Description of the Fe(IV) intermediate formation with PhIO $[Fe^{II}(asN4Py)Me\text{-}CN](ClO_4)_2$, complex ($2.00\times10^{-3}$ M) was dissolved in acetonitrile (1.5 mL), then iodosobenzene (4.00×10^{-3} M) added to the solution. The mixture was stirred for 50 minutes then the excess of iodosobenzene removed by filtration. Styrene (2.0×10^{-2} M) was added to the solution finally, reaction monitored by UV-vis spectrophotometer at 705 nm (λ_{max} = 400 M^{-1} cm^{-1}). The Fe^{IV}=O intermediates formed by PhIO show identical spectroscopic properties.

Stoichiometric oxidations

$[Fe^{II}(asN4Py)(CH_3CN)](ClO_4)_2$ **(1a)** complex (1.50×10^{-3} M) was dissolved in acetonitrile (1.5 mL), and then iodosobenzene (2.25×10^{-3} M) was added to the solution. The mixture was stirred for 40 minutes then the excess of iodosobenzene removed by filtration. Substrate (0.3 – 1.5 M) was added to the solution and the reaction was monitored with UV-vis spectrophotometer at 705 nm (ε = 400 M^{-1} cm^{-1}), the product analysis of the resulting solution was performed by GC and GC/MS:

Products are: cyclooctene oxide (75%); m/z (%) = 126 (2) [M^+], 98 (37), 93 (16), 83 (37), 77 (8), 67 (53), 55 (76), 41 (100), and cyclooct-2-enone (7%); m/z (%) = 124 (8) [M^+], 95 (10), 81 (100), 80 (67), 68 (48), 53 (52), 39 (70), and styrene oxide (65%): m/z (%) = 120 (31) [M^+], 91 (100), 77 (9), and benzaldehyde (12%); m/z (%) = 107 (5), 106 (72) [M^+], 77 (100), 74(11), 51 (60) for styrene oxidation.

Description of the asymmetric stoichiometric oxidation reaction

(-)-[Fe^{II}(asN4Py)]$^{2+}$ complex (6.45×10^{-3} M) was dissolved in acetonitrile (1.0 mL), then iodosobenzene (1.29×10^{-2} M) was added to the solution. The mixture was stirred for 50 minutes then the excess of iodosobenzene was removed by filtration. Styrene (4-Cl-styrene) (3.23×10^{1} M) was added to the solution and the mixture was stirred at 25 °C for 10 hours.

The products were identified by GC and the yield of styrene oxide (benzaldehyde) were calculated based on the amount of iron(IV)-oxo using bromobenzene as an internal standard in the reactions. Enantiomeric excess (ee %) was determined with GC analysis on chiral CHIRASIL-L-VAL column: ([R] - [S]) / ([R] + [S]).

Description of the asymmetric Stoichiometric oxidation of ethylbenzene by [Fe^{IV}(-)(asN4Py)(O)] complex (5.9×10^{-3} M) was dissolved in acetonitrile (1.0 mL), then iodosobenzene (1.18×10^{-2} M) was added to the solution. The mixture was stirred for 50 minutes then the excess iodosobenzene was removed by filtration. Ethylbenzene (6.45×10^{-1} M) was added to the solution and the mixture was stirred at 0 °C for 1.5 and 3 hours. The products were identified after 90 minutes by GC and the yield of 33% enantiomeric excess (ee) of main product 1-phenyl ethanol with the minor product of acetophenone and after 180 minutes 25% ee phenyl ethanol with minor product acetophenone under argon system. The yield of the products were calculated based on the amount of iron(IV)-oxo, bromobenzene used as an internal standard in the reactions, enantiomeric excess was determined with GC analysis on chiral columns (-dex, -dex): ([R] - [S]) / ([R] + [S]).

Reaction conditions for oxidation of flavanone

In a typical reaction, 2 ml of 500 mM, *m*-CPBA solution in CH_3CN was delivered by a syringe pump in the air or under argon to a stirred inside a vial. The final concentrations of the reagents were 5 mM, iron catalyst, 500 mM, *m*-CPBA, and 100 mM flavanone. After syringe pump addition (5 min the solution was stirred for 10 minutes and a known amount of PhBr (0.315 mmol) was added as an internal standard. The iron complex was removed by passing the reaction mixture through a silica column followed by elution with ethyl acetate. The products (1,3-dione (D) and a flavone) were identified by GC/MS and confirmed by comparison with authentic samples, flavone is commercially available and it was purchased from Sigma-Aldrich. GC-MS spectrum of flavone (F): *m/z*: 222 (100 %), 194 (44,4 %), 120 (81,4 %), 92 (55,6 %). 1,3-dione (D): m/z: 240 (15,1 %), 223 (8,3 %), 121 (25,2 %), 120 (7,3 %), 106 (7,2 %), 105 (100 %), 77 (30 %), 69 (6.0 %), 65 (9,3 %), 51 (4,5 %), 39 (8,3 %).

Description of the catalytic oxidation of *N*, *N*-dimethylaniline under air

In a typical reaction, 1 mL of H_2O_2 (diluted from 35% solution), *m*-CPBA (77%), PAA (Diluted from 38-40% solution) or TBHP (diluted from 70% solution) solution in CH_3CN was delivered by syringe pump in air to a stirred solution (2 mL) of catalyst $[Mn^{II}\{(Py)_2\text{-indH}\}(Cl)_2]$, $[Mn^{II}(asN4Py)(CH_3CN)](ClO_4)_2$ or $Mn(ClO_4)_2$ salt, and *p*-substituted DMAs. DMA substrate inside a vial. The final concentrations were 3 mM catalyst, 300 mM co-oxidant, and 300 mM substrate. The PhIO was added as a solid into the CH_3CN solution containing 100 µl of H_2O due to the poor solubility of PhIO, the yields were determined by comparison with dependable compounds using bromobenzene as an internal standard in the reactions. The products were identified by GC, GC/MS analysis, *N*-methylaniline (MA), Base Peak m/z 106 (100 %), 79.10 (31.31 %), 77 (51.66 %), 65 (24.13 %), 51 (42.05 %), 50 (21.68 %), 39 (33.25 %), 38 (12.04 %). And *N*-methylformanilide (MFA), m/z 136 (42.9 %), 106 (100 %), 77 (65.97 %), 66 (31.38 %), 65 (24.13 %), 51 (38.15 %), 39 (35.77 %).

Description of the catalytic oxidation of *N,N*-dimethylaniline under argon

In a typical reaction, 1 mL of H_2O_2 (diluted from 35% solution), *m*-CPBA (77%), PAA (diluted from 38-40% solution) or TBHP (diluted from 70% solution) solution in CH_3CN was delivered by syringe pump under argon to a stirred solution (2 mL) of the catalyst $[Mn^{II}(asN4Py)(CH_3CN)](ClO_4)_2$, and *p*-substituted MAs (Me-DMA, Br-DMA and CN-DMA), substrate inside a vial. The final concentrations were 3 mM catalyst, 300 mM co-oxidant, and 300 mM substrate. The PhIO was added as a solid into the CH_3CN solution containing 100 µl, of H_2O due to the poor solubility of PhIO, and their yields were determined by comparison with authentic compounds using bromobenzene as an internal standard in the reactions. The product was identified by GC/MS analysis, *N*-methylaniline (MA), Base Peak m/z 106 (100 %), 79.10 (31.31 %), 77 (51.66 %), 65 (24.13 %), 51 (42.05 %), 50 (21.68 %), 39 (33.25 %), 38 (12.04 %).

7 References

[1] I. G. Denisov, T. M. Makris, S. G. Sligar, and I. Schlichting, *Chem. Rev.,* **105** (2005) 2253-2278.

[2] M. Costas, M. P. Mehn, M. P. Jensen, and L. Que, *Chem. Rev.,* **104** (2004) 939-986.

[3] T. Matthew, *Acc. Chem. Res,* **40** (2007) 618-625.

[4] K. Sénéchal-David, C. Buron, N. Ségaud, J. N. Rebilly, A. Dos Santos, J. Farjon, R. Guillot, C. Herrero, T. Inceoglu, and F. Banse, *Chem. Eur. J.,* **25** (2019) 12405-12411.

[5] M. Costas, *Coord. Chem. Rev,* **255** (2011) 2912-2932.

[6] P. Liu, Y. Liu, E. L.-M. Wong, S. Xiang, and C.-M. Che, *Chem. Sci,* **2** (2011) 2187-2195.

[7] E. I. Solomon, T. C. Brunold, M. I. Davis, J. N. Kemsley, S.-K. Lee, N. Lehnert, F. Neese, A. J. Skulan, Y.-S. Yang, and J. Zhou, *Chem. Rev,* **100** (2000) 235-350.

[8] L. Que Jr and W. B. Tolman, *Nat. Chem. Biol.,* **455** (2008) 333-340.

[9] P. C. Bruijnincx, G. van Koten, and R. J. K. Gebbink, *Chem. Soc. Rev.,* **37** (2008) 2716-2744.

[10] E. I. Solomon, D. W. Randall, and T. Glaser, *Coord. Chem. Rev.,* **200** (2000) 595-632.

[11] G. B. Marin, G. S. Yablonsky, and D. Constales, *Kinetics of chemical reactions: Decoding complexity*: Wiley-VCH, (2019).

[12] B. Cornils, W. A. Herrmann, M. Beller, and R. Paciello, *Applied Homogeneous Catalysis with Organometallic Compounds: A Comprehensive Handbook in Four Volumes*: John Wiley & Sons, (2017).

[13] G. Rothenberg, *Catalysis: Concepts and Green Applications. Wiely*: VCH Weinheim, Germany:, (2008).

[14] R. Davydov, T. M. Makris, V. Kofman, D. E. Werst, S. G. Sligar, and B. M. Hoffman, *J. Am. Chem. Soc.,* **123** (2001) 1403-1415.

[15] R. Davydov, T. M. Makris, V. Kofman, D. E. Werst, S. G. Sligar, and B. M. Hoffman, *J. Am. Chem. Soc.,* **123** (2001) 1403-1415.

[16] T. S. Dowers, D. A. Rock, D. A. Rock, and J. P. Jones, *J. Am. Chem. Soc.,* **126** (2004) 8868-8869.

[17] S. Sahu and D. P. Goldberg, *J. Am. Chem. Soc.,* **138** (2016) 11410-11428.

[18] E. G. Kovaleva and J. D. Lipscomb, *Nat. Chem. Biol.,* **4** (2008) 186-193.

[19] W. Nam, *Dioxygen activation by metalloenzymes and models*: ACS Publications, (2007).

[20] S. O. Kim, C. V. Sastri, M. S. Seo, J. Kim, and W. Nam, *J. Am. Chem. Soc.,* **127** (2005) 4178-4179.

[21] H. Eklund, U. Uhlin, M. Färnegårdh, D. T. Logan, and P. Nordlund, *Prog. Biophy. Mol. Bio.,* **77** (2001) 177-268.

[22] W. Minor, J. Steczko, B. Stec, Z. Otwinowski, J. T. Bolin, R. Walter, and B. Axelrod, *Biochemistry,* **35** (1996) 10687-10701.

[23] C. Krebs, D. Galonic Fujimori, C. T. Walsh, and J. M. Bollinger Jr, *Acc. Chem. Res.,* **40** (2007) 484-492.

[24] X. Huang, T. Zhuang, P. A. Kates, H. Gao, X. Chen, and J. T. Groves, *J. Am. Chem. Soc.,* **139** (2017) 15407-15413.

[25] A. b. A. Shteinman, *Russ. Chem. Rev.,* **77** (2008) 945-966.

[26] C. A. Grapperhaus, B. Mienert, E. Bill, T. Weyhermüller, and K. Wieghardt, *Inorg. Chem.,* **39** (2000) 5306-5317.

[27] X. Shan and L. Que Jr, *J. Inorg. Biochem.*, **100** (2006) 421-433.
[28] S. V. Kryatov, E. V. Rybak-Akimova, and S. Schindler, *Chem. Rev.*, **105** (2005) 2175-2226.
[29] J. Rohde, *Science*, **299** (2003) 1037-1039.
[30] C. V. Sastri, M. J. Park, T. Ohta, T. A. Jackson, A. Stubna, M. S. Seo, J. Lee, J. Kim, T. Kitagawa, and E. Münck, *J. Am. Chem. Soc.*, **127** (2005) 12494-12495.
[31] A. Decker, J.-U. Rohde, L. Que, and E. I. Solomon, *J. Am. Chem. Soc.*, **126** (2004) 5378-5379.
[32] W. Nam, *Acc. Chem.*, **40** (2007) 522-531.
[33] L. Que Jr, *Acc. Chem.*, **40** (2007) 493-500.
[34] K. Nehru, M. S. Seo, J. Kim, and W. Nam, *Inorg. Chem.*, **46** (2007) 293-298.
[35] J. Bautz, P. Comba, C. Lopez de Laorden, M. Menzel, and G. Rajaraman, *Angew. Chem. Int. Ed.*, **46** (2007) 8067-8070.
[36] J. Kaizer, E. J. Klinker, N. Y. Oh, J.-U. Rohde, W. J. Song, A. Stubna, J. Kim, E. Münck, W. Nam, and L. Que, *J. Am. Chem. Soc.*, **126** (2004) 472-473.
[37] E. J. Klinker, J. Kaizer, W. W. Brennessel, N. L. Woodrum, C. J. Cramer, and L. Que Jr, *Angew. Chem. Int. Ed.*, **44** (2005) 3690-3694.
[38] C. B. Bell III, S. D. Wong, Y. Xiao, E. J. Klinker, A. L. Tenderholt, M. C. Smith, J. U. Rohde, L. Que Jr, S. P. Cramer, and E. I. Solomon, *Angew. Chem., Int. Ed.*, **47** (2008) 9071-9074.
[39] K. Ray, S. M. Lee, and L. Que Jr, *Inorganica Chim. Acta.*, **361** (2008) 1066-1069.
[40] Y. M. Lee, S. N. Dhuri, S. C. Sawant, J. Cho, M. Kubo, T. Ogura, S. Fukuzumi, and W. Nam, *Angew. Chem. Int. Ed.*, **48** (2009) 1803-1806.
[41] H. Kotani, T. Suenobu, Y.-M. Lee, W. Nam, and S. Fukuzumi, *J. Am. Chem. Soc.*, **133** (2011) 3249-3251.
[42] J. Bautz, M. R. Bukowski, M. Kerscher, A. Stubna, P. Comba, A. Lienke, E. Münck, and L. Que Jr, *Angew. Chem., Int. Ed.*, **45** (2006) 5681-5684.
[43] M. R. Bukowski, P. Comba, A. Lienke, C. Limberg, C. Lopez de Laorden, R. Mas-Ballesté, M. Merz, and L. Que Jr, *Angew. Chem., Int. Ed.*, **45** (2006) 3446-3449.
[44] P. Comba, S. Fukuzumi, H. Kotani, and S. Wunderlich, *Angew. Chem., Int. Ed.*, **49** (2010) 2622-2625.
[45] A. R. McDonald and L. Que Jr, *Coord. Chem. Rev.*, **257** (2013) 414-428.
[46] S. P. de Visser, J.-U. Rohde, Y.-M. Lee, J. Cho, and W. Nam, *Coord. Chem. Rev.*, **257** (2013) 381-393.
[47] K. P. Bryliakov and E. P. Talsi, *Coord. Chem. Rev.*, **276** (2014) 73-96.
[48] M. H. Lim, J.-U. Rohde, A. Stubna, M. R. Bukowski, M. Costas, R. Y. Ho, E. Münck, W. Nam, and L. Que, *Proc. Natl. Acad. Sci.*, **100** (2003) 3665-3670.
[49] M. S. Seo, N. H. Kim, K.-B. Cho, J. E. So, S. K. Park, M. Clémancey, R. Garcia-Serres, J.-M. Latour, S. Shaik, and W. Nam, *Chem. Sci.*, **2** (2011) 1039-1045.
[50] J. England, M. Martinho, E. R. Farquhar, J. R. Frisch, E. L. Bominaar, E. Münck, and L. Que Jr, *Angew. Chem. Chem. Int.*, **48** (2009) 3622-3626.
[51] D. C. Lacy, R. Gupta, K. L. Stone, J. Greaves, J. W. Ziller, M. P. Hendrich, and A. Borovik, *J. Am. Chem. Soc.*, **132** (2010) 12188-12190.
[52] G. Olivo, O. Lanzalunga, and S. Di Stefano, *Adv. Synth. Catal.*, **358** (2016) 843-863.
[53] S. Sahu and D. P. Goldberg, *J. Am. Chem. Soc.*, **138** (2016) 11410-11428.
[54] L. Que, *J. Biol. Inorg. Chem.*, **22** (2017) 171-173.

[55] M. Guo, T. Corona, K. Ray, and W. Nam, *ACS Cent. Sci.*, **5** (2018) 13-28.
[56] W. Nam, *Acc. Chem. Res.*, **48** (2015) 2415-2423.
[57] M. Puri and L. Que Jr, *Acc. Chem. Res.*, **48** (2015) 2443-2452.
[58] X. Engelmann, I. Monte-Pérez, and K. Ray, *Angew. Chem. Int. Ed.*, **55** (2016) 7632-7649.
[59] F. T. De Oliveira, A. Chanda, D. Banerjee, X. Shan, S. Mondal, L. Que, E. L. Bominaar, E. Münck, and T. J. Collins, *Science*, **315** (2007) 835-838.
[60] A. J. McGown, W. D. Kerber, H. Fujii, and D. P. Goldberg, *J. Am. Chem. Soc.*, **131** (2009) 8040-8048.
[61] P. R. Ortiz de Montellano, *Chem. Rev.*, **110** (2009) 932-948.
[62] C. A. Grapperhaus, B. Mienert, E. Bill, T. Weyhermüller, and K. Wieghardt, *Inorg Chem.*, **39** (2000) 5306-5317.
[63] J.-U. Rohde, M. R. Bukowski, and L. Que Jr, *Curr. Opin. Chem. Biol.*, **7** (2003) 674-682.
[64] J. Kaizer, M. Costas, and L. Que Jr, *Angew. Chem. Int. Ed.*, **42** (2003) 3671-3673.
[65] M. J. Collins, K. Ray, and L. Que, *Inorg. Chem.*, **45** (2006) 8009-8011.
[66] F. Li, K. M. Van Heuvelen, K. K. Meier, E. Münck, and L. Que Jr, *J. Am. Chem. Soc.*, **135** (2013) 10198-10201.
[67] M. J. Park, J. Lee, Y. Suh, J. Kim, and W. Nam, *J. Am. Chem. Soc.*, **128** (2006) 2630-2634.
[68] S. Hong, H. So, H. Yoon, K.-B. Cho, Y.-M. Lee, S. Fukuzumi, and W. Nam, *Dalton Trans.*, **42** (2013) 7842-7845.
[69] S. A. Wilson, J. Chen, S. Hong, Y.-M. Lee, M. Clémancey, R. Garcia-Serres, T. Nomura, T. Ogura, J.-M. Latour, and B. Hedman, *J. Am. Chem. Soc.*, **134** (2012) 11791-11806.
[70] O. Pestovsky, S. Stoian, E. L. Bominaar, X. Shan, E. Münck, L. Que Jr, and A. Bakac, *Angew. Chem., Int. Ed.*, **44** (2005) 6871-6874.
[71] J. P. Bigi, W. H. Harman, B. Lassalle-Kaiser, D. M. Robles, T. A. Stich, J. Yano, R. D. Britt, and C. J. Chang, *J. Am. Chem. Soc.*, **134** (2012) 1536-1542.
[72] J. U. Rohde and L. Que Jr, *Angew. Chem. Int. Ed.*, **44** (2005) 2255-2258.
[73] T. A. Jackson, J.-U. Rohde, M. S. Seo, C. V. Sastri, R. DeHont, A. Stubna, T. Ohta, T. Kitagawa, E. Münck, and W. Nam, *J. Am. Chem. Soc.*, **130** (2008) 12394-12407.
[74] A. Thibon, J. England, M. Martinho, V. G. Young Jr, J. R. Frisch, R. Guillot, J. J. Girerd, E. Münck, L. Que Jr, and F. Banse, *Angew. Chem. Int. Ed.*, **47** (2008) 7064-7067.
[75] A. R. McDonald, M. R. Bukowski, E. R. Farquhar, T. A. Jackson, K. D. Koehntop, M. S. Seo, R. F. De Hont, A. Stubna, J. A. Halfen, and E. Münck, *J. Am. Chem. Soc.*, **132** (2010) 17118-17129.
[76] W. Ye, D. M. Ho, S. Friedle, T. D. Palluccio, and E. V. Rybak-Akimova, *Inorg. Chem.*, **51** (2012) 5006-5021.
[77] Y. Suh, M. S. Seo, K. M. Kim, Y. S. Kim, H. G. Jang, T. Tosha, T. Kitagawa, J. Kim, and W. Nam, *Eur. J. Inorg. Chem.*, **100** (2006) 627-633.
[78] M. Martinho, F. Banse, J.-F. Bartoli, T. A. Mattioli, P. Battioni, O. Horner, S. Bourcier, and J.-J. Girerd, *Inorg. Chem.*, **44** (2005) 9592-9596.
[79] V. Balland, M. F. Charlot, F. Banse, J. J. Girerd, T. A. Mattioli, E. Bill, J. F. Bartoli, P. Battioni, and D. Mansuy, *Eur. J. Inorg. Chem.*, **2004** (2004) 301-308.

[80] J. M. Bollinger Jr, J. C. Price, L. M. Hoffart, E. W. Barr, and C. Krebs, *Eur. J. Inorg. Chem.,* **2005** (2005) 4245-4254.
[81] J. C. Price, E. W. Barr, B. Tirupati, J. M. Bollinger, and C. Krebs, *Biochemistry,* **42** (2003) 7497-7508.
[82] C. V. Sastri, M. S. Seo, M. J. Park, K. M. Kim, and W. Nam, *Chem. Comm.,* (2005) 1405-1407.
[83] D. Lakk-Bogáth, G. Speier, and J. Kaizer, *New J Chem.,* **39** (2015) 8245-8248.
[84] N. Y. Oh, Y. Suh, M. J. Park, M. S. Seo, J. Kim, and W. Nam, *Angew. Chem. Int. Ed.,* **44** (2005) 4235-4239.
[85] B. I. Meena, D. Lakk-Bogáth, B. Kripli, G. Speier, and J. Kaizer, *Polyhedron,* **151** (2018) 141-145.
[86] J. Annaraj, S. Kim, M. S. Seo, Y.-M. Lee, Y. Kim, S.-J. Kim, Y. S. Choi, H. G. Jang, and W. Nam, *Inorganic Chim. Acta.,* **362** (2009) 1031-1034.
[87] A. N. Biswas, M. Puri, K. K. Meier, W. N. Oloo, G. T. Rohde, E. L. Bominaar, E. Münck, and L. Que Jr, *J. Am. Chem. Soc.,* **137** (2015) 2428-2431.
[88] C.-M. Che and V. W.-W. Yam, *High-valent complexes of ruthenium and osmium* in *Adv. Inorg. Chem.,* 39, ed: Elsevier, (1992), 233-325.
[89] W.-C. Cheng, W.-Y. Yu, K.-K. Cheung, and C.-M. Che, *J. Am. Chem. Soc.,* (1994) 1063-1064.
[90] D. Chatterjee, *Inorganica Chim. Acta.,* **361** (2008) 2177-2182.
[91] K. Chen and J. Que, Lawrence, *Angew. Chem. Int.,* **38** (1999) 2227-2229.
[92] J. Y. Ryu, J. Kim, M. Costas, K. Chen, W. Nam, and L. Que Jr, *Chem. Comm.,* (2002) 1288-1289.
[93] W. Nam, R. Ho, and J. S. Valentine, *J. Am. Chem. Soc.,* **113** (1991) 7052-7054.
[94] K. Chen, M. Costas, J. Kim, A. K. Tipton, and L. Que, *J. Am. Chem. Soc.,* **124** (2002) 3026-3035.
[95] S. Tanase, C. Foltz, R. de Gelder, R. Hage, E. Bouwman, and J. Reedijk, *J. Mol. Catal. A.,* **225** (2005) 161-167.
[96] S. Mukhopadhyay, S. K. Mandal, S. Bhaduri, and W. H. Armstrong, *Chem. Rev.,* **104** (2004) 3981-4026.
[97] C. Zheng and S. You, *Chem. Rev.,* **111** (2011) 1215-1297
[98] W. Zhang, F. Wang, S. D. McCann, D. Wang, P. Chen, S. S. Stahl, and G. Liu, *Science,* **353** (2016) 1014-1018.
[99] O. A. Andersen, A. J. Stokka, T. Flatmark, and E. Hough, *J. Mol. Biol.,* **333** (2003) 747-757.
[100] S. Rana, A. Dey, and D. Maiti, *Chem. Comm.,* **51** (2015) 14469-14472.
[101] S. Sinnecker, N. Svensen, E. W. Barr, S. Ye, J. M. Bollinger Jr, F. Neese, and C. Krebs, *J. Am. Chem. Soc.,* **129** (2007) 6168-6179.
[102] D. Lakk-Bogáth, R. Csonka, G. Speier, M. Réglier, A. J. Simaan, and J. Kaizer, *Inorg. Chem.,* **55** (2016) 10090-10093.
[103] N. A. Law, M. T. Caudle, and V. L. Pecoraro, *Manganese redox enzymes and model systems: properties, structures, and reactivity* in *Adv. Inorg. Chem.* 46, ed: Elsevier, (1998), 305-440.
[104] A. J. Wu, J. E. Penner-Hahn, and V. L. Pecoraro, *Chem. Rev.,* **104** (2004) 903-938.
[105] S. Iwata and J. Barber, *Curr. Opin. Struct. Biol.,* **14** (2004) 447-453.

[106] K. N. Ferreira, T. M. Iverson, K. Maghlaoui, J. Barber, and S. Iwata, *Science,* **303** (2004) 1831-1838.
[107] L. Hörnsten, C. Su, A. E. Osbourn, U. Hellman, and E. H. Oliw, *Eur. J. Biochem.,* **269** (2002) 2690-2697.
[108] H. Li, B. Zheng, and K.-W. Huang, *Coord. Chem. Rev.,* **293** (2015) 116-138.
[109] H. A. Younus, N. Ahmad, W. Su, and F. Verpoort, *Coord. Chem. Rev.,* **276** (2014) 112-152.
[110] G. Van Koten and D. Milstein, *Organometallic pincer chemistry*: Springer, (2012).
[111] R. Csonka, G. Speier, and J. Kaizer, *RSC Adv.,* **5** (2015) 18401-18419.
[112] A. L. Müller, H. Wadepohl, and L. H. Gade, *Organometallics,* **34** (2015) 2810-2818.
[113] J. S. Pap, J. Kaizer, M. Giorgi, and G. Speier, *Inorg. Chem. Commun.,* **13** (2010) 1069-1073.
[114] J. Kaizer, G. Baráth, R. Csonka, G. Speier, L. Korecz, A. Rockenbauer, and L. Párkányi, *J. Inorg. Biochem.,* **102** (2008) 773-780.
[115] J. Kaizer, T. Csay, P. Kővári, G. Speier, and L. Párkányi, *J. Mol. Catal. A.,* **280** (2008) 203-209.
[116] M. Szávuly, R. Csonka, G. Speier, R. Barabás, M. Giorgi, and J. Kaizer, *J. Mol. Catal. A.,* **392** (2014) 120-126.
[117] H.-M. Wen, Y.-H. Wu, Y. Fan, L.-Y. Zhang, C.-N. Chen, and Z.-N. Chen, *Inorg. Chem.,* **49** (2010) 2210-2221.
[118] D.-B. Zhang, J.-Y. Wang, H.-M. Wen, and Z.-N. Chen, *Organometallics,* **33** (2014) 4738-4746.
[119] B. Siggelkow, M. B. Meder, C. H. Galka, and L. H. Gade, *Eur. J. Inorg. Chem.,* **2004** (2004) 3424-3435.
[120] M. B. Meder, B. A. Siggelkow, and L. H. Gade, *Z. Anorg. Allg. Chem.,* **630** (2004) 1962-1968.
[121] D. C. Sauer, H. Wadepohl, and L. H. Gade, *Inorg. Chem.,* **51** (2012) 12948-12958.
[122] I.-S. Tamgho, J. T. Engle, and C. J. Ziegler, *Tetrahedron Lett.,* **54** (2013) 6114-6117.
[123] B. Kim, C. Yalaz, and D. Pan, *Tetrahedron Lett.,* **53** (2012) 4134-4137.
[124] R. Csonka, G. Speier, and J. Kaizer, *RSC Adv.,* **5** (2015) 18401-18419.
[125] J. Kaizer, G. Baráth, G. Speier, M. Réglier, and M. Giorgi, *Inorg. Chem. Commun.,* **10** (2007) 292-294.
[126] J. Kaizer, T. Csay, P. Kővári, G. Speier, and L. Párkányi, *J. Mol. Catal. A.,* **280** (2008) 203-209.
[127] B. Kripli, G. Baráth, É. Balogh-Hergovich, M. Giorgi, A. J. Simaan, L. Párkányi, J. S. Pap, J. Kaizer, and G. Speier, *Inorg. Chem. Commun.,* **14** (2011) 205-209.
[128] J. Kaizer, B. Kripli, G. Speier, and L. Párkányi, *Polyhedron,* **28** (2009) 933-936.
[129] J. S. Pap, B. Kripli, T. Váradi, M. Giorgi, J. Kaizer, and G. Speier, *J. Inorg. Biochem.,* **105** (2011) 911-918.
[130] C. Kleeberg and M. Bröring, *Polyhedron,* **29** (2010) 507-513.
[131] J. S. Pap, M. Giorgi, J. Kaizer, and G. Speier, *Inorg. Chem. Commun.,* **27** (2013) 152-155.
[132] T. n. Váradi, J. z. S. Pap, M. Giorgi, L. Párkányi, T. Csay, G. b. Speier, and J. Kaizer, *Inorg. Chem.,* **52** (2013) 1559-1569.
[133] É. Balogh-Hergovich, G. Speier, B. Tapodi, M. Reglier, and M. Giorgi, *Z KRIST-NEW CRYST. ST.,* **214** (1999) 579-580.

[134] J. T. Engle, G. Martić, and C. J. Ziegler, *Macroheterocycles* **6** (2013) 353-359.
[135] M. Szávuly, R. Csonka, G. Speier, R. Barabás, M. Giorgi, and J. Kaizer, *J. Mol. Catal. A.,* **392** (2014) 120-126.
[136] Y.-J. Sun, Q.-Q. Huang, T. Tano, and S. Itoh, *Inorg. Chem.,* **52** (2013) 10936-10948.
[137] M. K. Coggins, X. Sun, Y. Kwak, E. I. Solomon, E. Rybak-Akimova, and J. A. Kovacs, *J. Am. Chem. Soc.,* **135** (2013) 5631-5640.
[138] G. Yin, A. M. Danby, D. Kitko, J. D. Carter, W. M. Scheper, and D. H. Busch, *J. Am. Chem. Soc.,* **129** (2007) 1512-1513.
[139] X. Wu, M. S. Seo, K. M. Davis, Y.-M. Lee, J. Chen, K.-B. Cho, Y. N. Pushkar, and W. Nam, *J. Am. Chem. Soc.,* **133** (2011) 20088-20091.
[140] R. Zhang and M. Newcomb, *Acc. Chem. Res.,* **41** (2008) 468-477.
[141] T. J. Collins, R. D. Powell, C. Slebodnick, and E. S. Uffelman, *J. Am. Chem. Soc.,* **112** (1990) 899-901.
[142] J. T. Groves, J. Lee, and S. S. Marla, *J. Am. Chem. Soc.,* **119** (1997) 6269-6273.
[143] W. Adam, C. Mock-Knoblauch, C. R. Saha-Möller, and M. Herderich, *J. Am. Chem. Soc.,* **122** (2000) 9685-9691.
[144] W. Adam, K. J. Roschmann, C. R. Saha-Möller, and D. Seebach, *J. Am. Chem. Soc.,* **124** (2002) 5068-5073.
[145] E. M. McGarrigle and D. G. Gilheany, *Chem. Rev.,* **105** (2005) 1563-1602.
[146] J. S. Pap, J. Kaizer, and G. Speier, *Coord. Chem. Rev.,* **254** (2010) 781-793.
[147] I. Batinic-Haberle, Z. Rajic, A. Tovmasyan, J. S. Reboucas, X. Ye, K. W. Leong, M. W. Dewhirst, Z. Vujaskovic, L. Benov, and I. Spasojevic, *Free Radic Biol Med.,* **51** (2011) 1035-1053.
[148] K. H. Thompson and C. Orvig, *Science,* **300** (2003) 936-939.
[149] D. P. Riley, *Chem. Rev.,* **99** (1999) 2573-2588.
[150] G.-F. Liu, K. Dürr, R. Puchta, F. W. Heinemann, R. van Eldik, and I. Ivanović-Burmazović, *Dalton Trans.,* (2009) 6292-6295.
[151] I. Batinić-Haberle, I. Spasojević, R. D. Stevens, P. Hambright, P. Neta, A. Okado-Matsumoto, and I. Fridovich, *Dalton Trans.,* (2004) 1696-1702.
[152] R. Turcas, B. Kripli, A. A. Attia, D. Lakk-Bogáth, G. Speier, M. Giorgi, R. Silaghi-Dumitrescu, and J. Kaizer, *Dalton Trans.,* **47** (2018) 14416-14420.
[153] M. Tamura, Y. Urano, K. Kikuchi, T. Higuchi, M. Hirobe, and T. Nagano, *Chem. Pharm. Bull.,* **48** (2000) 1514-1518.
[154] M. Sjödin, J. Gätjens, L. C. Tabares, P. Thuéry, V. L. Pecoraro, and S. Un, *Inorg. chem.,* **47** (2008) 2897-2908.
[155] R. Irie, N. Hosoya, and T. Katsuki, *Synlett.,* (1994) 255-256.
[156] P. Pietikäinen, *Tetrahedron Lett.,* **35** (1994) 941-944.
[157] P. Pietikäinen, *Tetrahedron,* **54** (1998) 4319-4326.
[158] M. Newcomb, R. Shen, S.-Y. Choi, P. H. Toy, P. F. Hollenberg, A. D. Vaz, and M. J. Coon, *J. Am. Chem. Soc.,* **122** (2000) 2677-2686.
[159] J. Van der Zee, D. Duling, R. Mason, and T. Eling, *J. Biol. Chem.,* **264** (1989) 19828-19836.
[160] J. I. Manchester, J. P. Dinnocenzo, L. Higgins, and J. P. Jones, *J. Am. Chem. Soc.,* **119** (1997) 5069-5070.
[161] C. Yi, C.-G. Yang, and C. He, *Acc. Chem. Res.,* **42** (2009) 519-529.

[162] D. Naróg, U. Lechowicz, T. Pietryga, and A. Sobkowiak, *J. Mol. Catal. A.,* **212** (2004) 25-33.
[163] D. Lakk-Bogáth, B. Kripli, B. I. Meena, G. Speier, and J. Kaizer, *Polyhedron,* **169** (2019) 169-175.
[164] W. Ye, D. M. Ho, S. Friedle, T. D. Palluccio, and E. V. Rybak-Akimova, *Int. J. Inorg. Chem.,* **51** (2012) 5006-5021.
[165] E. P. Talsi and K. P. Bryliakov, *Coord. Chem. Rev.,* **256** (2012) 1418-1434.
[166] W.-H. Fung, W.-Y. Yu, and C.-M. Che, *JOC,* **63** (1998) 7715-7726.
[167] D. Lakk-Bogáth, G. Speier, and J. Kaizer, *Inorg. Chem. Commun.,* **107** (2019) 107446.
[168] Y.-D. Wu, C.-L. Wong, K. W. Chan, G.-Z. Ji, and X.-K. Jiang, *JOC,* **61** (1996) 746-750.
[169] J. T. Groves, Z. Gross, and M. K. Stern, *Inorg. Chem.,* **33** (1994) 5065-5072.
[170] W. J. Song, Y. O. Ryu, R. Song, and W. Nam, *J. Biol. Inorg. Chem.,* **10** (2005) 294-304.
[171] W. Zhang, J. L. Loebach, S. R. Wilson, and E. N. Jacobsen, *J. Am. Chem. Soc.,* **112** (1990) 2801-2803.
[172] C. Zheng and S.-L. You, *RSC. Adv.,* **4** (2014) 6173-6214.
[173] Q. Lu and F. Glorius, *Angew. Chem.,* **56** (2017) 49-51.
[174] H. Lu and X. P. Zhang, *Chem. Soc. Rev.,* **40** (2011) 1899-1909.
[175] K.-B. Cho, H. Hirao, S. Shaik, and W. Nam, *Chem. Soc. Rev.,* **45** (2016) 1197-1210.
[176] M. Mitra, H. Nimir, D. A. Hrovat, A. A. Shteinman, M. G. Richmond, M. Costas, and E. Nordlander, *J. mol. catal. A.,* **426** (2017) 350-356.
[177] J. S. Pap, V. Bányai, D. S. Szilvási, J. Kaizer, G. Speier, and M. Giorgi, *Inorganic Chem. Commun.,* **14** (2011) 1767-1772.
[178] H. Yoon, Y. Morimoto, Y.-M. Lee, W. Nam, and S. Fukuzumi, *Chem. Commun.,* **48** (2012) 11187-11189.
[179] P. A. MacFaul, D. Wayner, and K. Ingold, *Acc. Chem. Res.,* **31** (1998) 159-162.
[180] W. J. Song, Y. O. Ryu, R. Song, and W. Nam, *J. Biol. Inorg. Chem.,* **10** (2005) 294-304.
[181] D. Y. Murzin and T. Salmi, *Catalytic kinetics*: Elsevier, (2005).
[182] S. Shaik, A. W. Munro, S. Sen, C. Mowat, W. Nam, E. Derat, and G. D. Straganz, *Iron-containing enzymes*, Royal Society of Chemistry, (2011).
[183] J. J. Warren, T. A. Tronic, and J. M. Mayer, *Chem. Rev.,* **110** (2010) 6961-7001.
[184] S. Kozuch and J. M. Martin, *J. Am. Chem. Catal.,* **2** (2012) 2787−2794.
[185] Y.-D. Wu, C.-L. Wong, K. W. Chan, G.-Z. Ji, and X.-K. Jiang, *J. Org. Chem.,* **61** (1996) 746-750.

8 Appendix

Table S1. Substrate dependent reaction of $[[Fe^{IV}(asN4Py)(O)]^{2+}] = 1.5\times10^{-3}$ M, with *cis*-cyclooctene and styrene in CH_3CN at 298 K

NO.	$Fe^{IV}O$(asN4Py) (10^{-3} M)	Substrate	Substrate (M)	k_{obs} (10^{-4} s^{-1})	$Fe^{IV}O$ (as N4Py) (10^{-3} M)	k_2 (10^{-4} M^{-1} s^{-1})
1	0	Cyclooctene	0	0	0	0
2	1.5	Cyclooctene	0.3	1.63	1.5	5.4±0.2
3	1.5	Cyclooctene	0.51	2.76	1.5	5.4±0.17
4	1.5	Cyclooctene	0.75	4.06	1.5	5.4±0.2
5	1.5	Cyclooctene	0.9	5.01	1.5	5.5±0.3
6	0	styrene	0	0	0	0
7	1.5	styrene	0.3	0.87	1.5	2.9±0.2
8	1.5	styrene	0.49	1.44	1.5	2.9±0.14
9	1.5	styrene	0.6	1.75	1.5	2.9±0.3
10	1.5	styrene	0.9	2.65	1.5	2.9±0.2

Table S2. Temperature-dependent reaction of $[[Fe^{IV}(asN4Py)(O)]^{2+}]_0 = 1.5\times10^{-3}$ M, for *cis*-cyclooctene and styrene in CH_3CN

Substrate	[S] (M)	T (K)	1/T(10^{-3} K^{-1})	k_{obs} (10^{-4} s^{-1})	k_2 (10^{-4} M^{-1} s^{-1})	Log k_2
Cyclooctene	0.75	293	3.41	3.46	4.6±0.1	-3.35
Cyclooctene	0.75	298	3.35	4.06	5.4±0.3	-3.26
Cyclooctene	0.75	303	3.30	5.29	7.0±0.2	-3.15
Cyclooctene	0.75	308	3.24	7.5	10.0±0.3	-2.99
Cyclooctene	0.75	311	3.21	9.2	12.3±0.4	-2.92
styrene	1.5	293	3.412	3.09	2.0±0.03	-3.68
styrene	1.5	298	3.35	4.48	3.0±0.16	-3.52
styrene	1.5	303	3.30	8.26	5.6±0.3	-3.25
styrene	1.5	308	3.24	12.18	8.5±0.2	-3.07
styrene	1.5	311	3.21	14.07	9.4±0.3	-3.02

Table S3. Calculated value of log (*k*/T) the reaction of $[[Fe^{IV}(asN4Py)(O)]^{2+}]_0$ = 1.5×10^{-3} M, for *cis*-cyclooctene and styrene in CH_3CN

T (K)	**1/T (10^{-3} K^{-1})**	**k_2 ($S^{-1}10^{-4}$)**	**k/T (10^{-6})**	**logk/T**
293	3.412	4.6±0.1	1.574	-5.803
298	3.355	5.4±0.3	1.816	-5.741
303	3.30	7.0±0.2	2.327	-5.633
308	3.246	10.0±0.3	3.246	-5.487
311	3.21	12.3±0.3	3.94	-5.404
T (K)	1/T	k_2 (10^{-4})	k/T (10^{-7})	logk/T
293	3.412	2.0±0.03	7.030	-6.15
298	3.355	3.0±0.3	10.033	-5.97
303	3.30	5.57±0.2	18.389	-5.735
308	3.246	8.5±0.3	27.597	-5.559
311	3.21	14.0±0.3	45.24	-5.344

Table S4. The reaction of $[Fe^{IV}(asN4Py)(O)]^{2+}$ with *cis*-cyclooctene and styrene in CH_3CN at 298 K

No.	**$Fe^{IV}O(asN_4Py)$ (10^{-3} M)**	**Cyclooctene (M)**	**Styrene (M)**	**Vi (10^{-7} Ms^{-1})**
1	0.5	0.3		0.78
2	1.0	0.3		1.59
3	1.5	0.3		2.85
4	2.0	0.3		3.13
5	2.5	0.3		5.08
6	0.5		0.3	0.37
7	1.0		0.3	0.95
8	1.5		0.3	1.15
9	3.0		0.3	2.77

Table S5. The reaction of $[[Fe^{IV}(asN4Py)(O)]^{2+}]_0 = 1.5\times10^{-3}$ M, with styrene derivatives in CH_3CN at 298 K

[S]	**$[Fe^{IV}O(asN4Py)]$ (10^{-3} M)**	**Substrate (M) styrene**	**k_{obs} (10^{-4} s^{-1})**	**k_2 (10^{-4} M^{-1} s^{-1})**
0	0	0	0	0
H	1.5	0.3	0.87	2.90±0.1
H	1.5	0.49	1.44	2.94±0.2
H	1.5	0.6	1.75	2.92±0.1
H	1.5	0.9	2.65	2.943±0.15
OMe	1.5	0.3	1.43	4.62±0.2
4-Cl-	1.5	0.3	0.95	3.16±0.1
4-CN-	1.5	0.3	1.31	3.58±0.3

Table S6. The reaction of $[Fe^{IV}(asN4Py)(O)]^{2+}$ with ethylbenzene in CH_3CN

Reactions	**Temp**	**Time hour**	**Complex (M)**	**Oxidizing agent (M)**	**Ethylbenzene**	**Acetophenone mMole**	**2-Phenyl 1-ethanol mMole**	**ee%**
1	25	1.5	$5.9x10^{-3}$	$1.18x10^{-2}$	2M	0.56	0.53	9.5
2	25	3	$5.9x10^{-3}$	$1.18x10^{-2}$	2M	0.66	0.65	6
3	0	1.5	$5.9x10^{-3}$	$1.18x10^{-2}$	2M	0.122	0.116	32
4	0	3	$5.9x10^{-3}$	$1.18x10^{-2}$	2M	0.18	0.147	24.5
5	-20	1.5	$5.9x10^{-3}$	$1.18x10^{-2}$	2M	0.81	0.09	27.8
6	-20	3	$5.9x10^{-3}$	$1.18x10^{-2}$	2M	0.64	0.157	12.2

Table S7. Summary of kinetic data for the catalytic oxidation of morin with $[Mn^{II}(HL^3)Cl_2]$ **(3)** in bicarbonate buffer at pH 10 and 25 °C

Catalyst (3) (10^{-6} M)	**[H_2O_2] (10^{-3} M)**	**[HCO_3^-] (10^{-3} M)**	**[Morin] (10^{-3} M)**	**k_{obs} ($10^{-3}s^{-1}$)**	**k_{ox} ($10^6 M^{-3}s^{-1}$)**
0.62	10	50	0.16	1.6±0.06	5.3±0.2
1.6	10	50	0.16	4.2±0.16	5.2±0.2
2.5	10	50	0.16	6.7±0.37	5.4±0.3
0.62	10	50	0.16	1.6±0.06	5.3±0.2
0.62	7.5	50	0.16	1.2±0.05	5.3±0.2
0.62	5.0	50	0.16	0.78±0.02	5.1±0.1
0.62	2.5	50	0.16	0.4±0.01	5.3±0.2
0.62	10	50	0.16	1.6±0.06	5.3±0.2
0.62	10	100	0.16	3.0±0.06	5.2±0.1
0.62	10	200	0.16	7.0±0.13	5.2±0.1
0.62	10	300	0.16	10.5±0.6	5.4±0.3
0.62	10	50	0.16	1.6±0.06	5.3±0.2
0.62	10	50	0.12	1.6±0.03	5.3±0.1
0.62	10	50	0.04	1.7±0.06	5.5±0.2
0.62	10	50	0.16	1.7±0.06	5.5±0.2

Table S8. Calculated Log(TOF) for complexes (**3-8**) with $E^o_{1/2}$

log TOF	**TOF**	**TON**	**$E°'_{1/2Mn(III)/Mn(II)\ fc}$(mV)**
-2.77	0.00166	6	921.5
-2.86	0.00138	5	948
-2.93	0.00116	4.2	750
-2.946	0.00113	4.1	600.5
-2.99	0.00102	3.7	725.5
-3	0.001	3.6	387.5
-3.11	0.00077	2.8	425

Table S9. Effect of water on catalytic oxidation flavanone, [[$Mn(py)_2indH]^{2+}$] = 3 mM, [S] = 100 mM, [Ox] = 300 mM, in acetonitrile at 25 °C by *m*-CPBA

H_2O mM	**Complex (mM)**	**substrate (mM)**	**Oxidant (mM)**	**Flavone (mM)**	**TON**	**Carbonyl**	**TON**	**yield**
30	5	100	500	14.15	4.8	1.1	0.36	15.25
40	5	100	500	12.85	4.3	1.89	0.63	14.6
50	5	100	500	11.64	3.88	2.2	0.73	13.8
60	5	100	500	10.5	3.5	2.6	0.9	13.1
70	5	100	500	8.3	2.77	3.05	1	11.35
80	5	100	500	7.55	2.5	2.8	0.93	10.35
90	5	100	500	6.3	21	1.9	0.63	8.2

Table S10. Complex dependent catalytic oxidation flavanone in acetonitrile at 25 °C by *m*-CPBA

[Comp.]	**Complex (mM)**	**Substrate (mM)**	**Oxidant *m*-CPBA (mM)**	**Flavone (mM)**	**TN**	**Carbonyl**	**yield**
$Mn(py)_2$-indH	5	100	500	30	6	6.1	36.1
Mn(4-me-$py)_2$-indH	5	100	500	25	5	5.7	30.7
$Mn(im)_2$-indH	5	100	500	22.5	4.2	5.2	27.7
$Mn(tia)_2$-indH	5	100	500	21.1	4.1	5	26.1
$Mn(bim)_2$-indH	5	100	500	18	3.6	4.5	22.5
Mn(N-me-$bim)_2$-indH	5	100	500	14	2.8	4.9	20.2

Table S11. Oxidation of *N*,*N*-dimethylaniline with various co-oxidants in CH_3CN at 30 °C. $[Mn(ClO_4)_2]$ = 3 mM, [S] = 300 mM, [Ox] = 300 mM

[Comp.]	[Comp.]:[S]:[Co-oxidant]	mmole product1	mmole product2	Yield 1	Yield2	TON 1+2	Yield 1+2 (%)
$Mn(ClO_4)_2$	3:300:300 (*m*-CPBA)	5.8	2.59	1.93	0.86	2.76	2.76
$Mn(ClO_4)_2$	3:300:300 (PAA)	3.2	1.8	1.6	0.6	2.2	2.2
$Mn(ClO_4)_2$	3:300:300 (TBHP)	1.85	0.28	0.61	0.093	0.7	0.7
$Mn(ClO_4)_2$	3:300:300 (PhIO)	1.5	0.18	0.5	0.06	0.56	0.56
$Mn(ClO_4)_2$	3:300:300 (H2O2)	1.1	0.17	0.36	0.056	0.41	0.41

Table S12. Oxidation of *N*,*N*-dimethylaniline with various co-oxidants in CH_3CN at 30 °C. $[Mn^{II}(py)_2\text{-indH}]$ = 3 mM, [S] = 300 mM, [Ox] = 300 mM

[Comp.]	[Comp.]:[S]:[Co-oxidant]	mmole product 1	mmole product 2	Yield 1	Yield 2	TON 1+2	Yield 1+2 (%)
$Mn(py)_2$	3:300:300 (*m*-CPBA)	115	60	38	20	58	58
$Mn(py)_2$	3:300:300 (PAA)	93	33	31	11	42	33
$Mn(py)_2$	3:300:300 (TBHP)	44.7	22	14.9	7.33	22.3	22.3
$Mn(py)_2$	3:300:300 (PhIO)	34.7	16	11.5	5.3	16.8	16.8
$Mn(py)_2$	3:300:300 (H_2O_2)	12.5	5	4.15	1.6	5.7	5.7

Table S13. Manganese-catalyzed oxidation of [Mn^{II}] = 3 mM, [S] = 300 mM, [Ox] = 300 mM, *N*,*N*-dimethylanilines derivatives with various oxidants in CH_3CN at 30 °C

[S]	[Comp.]	[Comp.]:[S]: [Co-oxidant]	mmol prod.1	mmol prod. 2	Yield 1	Yield 2	MA/ DMA	Yield 1+2 (%)
Me	$Mn(py)_2$	3:300:300 (PAA)	138	33	46	11	4.18	57
H	$Mn(py)_2$	3:300:300 (PAA)	110	32.6	36.7	10.8	3.39	47.5
Br	$Mn(py)_2$	3:300:300 (PAA)	85	35	28.3	10	2.83	38.3
CN	$Mn(py)_2$	3:300:300) (PAA)	70	33.5	23.3	11.16	2	34.2
Me	$Mn(py)_2$	3:300:300 (m-CPBA)	145	35	48.3	11.2	4.32	60
H	$Mn(py)_2$	3:300:300 (m-CPBA)	120	33.6	40	11.2	3.6	51.2
Br	$Mn(py)_2$	3:300:300 (m-CPBA)	102	35.4	34	11.8	2.9	45.8
CN	$Mn(py)_2$	3:300:300 (m-CPBA)	60	30	20	10	2	30
Me	$Mn(py)_2$	3:300:300 (TBHP)	101	30	33	10	3	43
H	$Mn(py)_2$	3:300:300 (TBHP)	70	22.2	23.3	7.4	2.25	30.7
Br	$Mn(py)_2$	3:300:300 (TBHP)	39	21	13	7	1.85	20
CN	$Mn(py)_2$	3:300:300 (TBHP)	25	20.7	8.3	6.9	1.16	15.2
Me	$Mn(py)_2$	3:300:300 (H_2O_2)	14	6	4.7	2	2.35	6.7
H	$Mn(py)_2$	3:300:300 (H_2O_2)	10	5.7	3.4	1.9	1.8	5.3
Br	$Mn(py)_2$	3:300:300 (H_2O_2)	8.8	6.1	2.94	2	1.5	4.94
CN	$Mn(py)_2$	3:300:300 (H_2O_2)	7	6	2.4	2	1.2	4.4

Table S14. Oxidation of *N*,*N*-dimethylaniline with various co-oxidants in CH_3CN at 30 °C, [Mn^{II}(asN4Py)] = 3 mM, [S] = 300 mM, [Ox] = 300 mM under air atmosphere

[Comp.]	[Comp.]:[S]:[Co-oxidant]	mmol. Prod. 1	Mmol Prod.2	TON 1	TON 2	MA/DMA	Yield 1+2 (%)
Mn^{II}(asN4Py)	3:300:300 (*m*-CPBA)	107	36.3	35.5	12	2.9	47.5
Mn^{II}(asN4Py)	3:300:300 (PAA)	95	36	31.6	12	2.6	43.6
Mn^{II}(asN4Py)	3:300:300 (TBHP)	47.5	20.3	15.8	6.7	1.56	22.5
Mn^{II}(asN4Py)	3:300:300 (PhIO)	30	12.5	10	4.16	1.18	14.7
Mn^{II}(asN4Py)	3:300:300 (H_2O_2)	15	3.5	5	1.2	4.15	6.2

Table S15. Oxidation of *N*,*N*-dimethylaniline with various co-oxidants in CH_3CN at 30 °C, [Mn^{II}(asN4Py)] = 3 mM, [S] = 300 mM, [Ox] = 300 mM under argon atmosphere

[Comp.]	[Comp.]:[S]:[Co-oxidant]	mmol. Prod. 1	TON 1	Yield (%)
Mn^{II}(asN4Py)	3:300:300 (*m*-CPBA)	70	23.5	23.5
Mn^{II}(asN4Py)	3:300:300 (PAA)	41	13	13
Mn^{II}(asN4Py)	3:300:300 (TBHP)	29.8	10	10
Mn^{II}(asN4Py)	3:300:300 (PhIO)	14	4.6	4.6
Mn^{II}(asN4Py)	3:300:300 (H_2O_2)	10	3.2	3.2

Table S16. Oxidation of *N*,*N*-dimethylaniline with PAA and *m*-CPBA co-oxidants in CH_3CN at 30 °C, [Mn^{II}(asN4Py)] = 3 mM, [S] = 300 mM [Ox] = 300 mM

[S]	[Comp.]	[Comp.]:[S]: [Co-oxidant]	mmole prod.1	mmole prod. 2	Yield 1	Yield2	MA/ DMA	Yield 1+2 (%)
Me	Mn^{II}(asN4Py)	3:300:300 (m-CPBA)	115	35	38.3	11.7	3.32	50
H	Mn^{II}(asN4Py)	3:300:300 (m-CPBA)	107	36.3	35.5	12	2.9	47.5
Br	Mn^{II}(asN4Py)	3:300:300 (m-CPBA)	73	35.8	24.3	12	2	36.3
CN	Mn^{II}(asN4Py)	3:300:300 (m-CPBA)	53	33.5	17.7	11.16	1.58	28.86
Me	Mn^{II}(asN4Py)	3:300:300 (PAA)	110	33	36	11	3.27	47
H	Mn^{II}(asN4Py)	3:300:300 (PAA)	95	36	31.6	12	2.6	43.6
Br	Mn^{II}(asN4Py)	3:300:300 (PAA)	82.2	39	27.6	13	2	31.6
CN	Mn^{II}(asN4Py)	3:300:300 (PAA)	45	35.4	15	12	1.25	27.1

Table S17. Reactions of [Mn^{II}(asN4Py)(CH_3CN)](CF_3SO_3)$_2$ and [Mn(py)$_2$indH]$^{+2}$ with DMAs by the use of *m*-CPBA in CH_3CN at 30 °C

[S]	MA/DMA Mn^{II}(asN4py)	MA/DMA $Mn^{II}(py)_2$	σ_p	[S]	MA/DMA Mn^{II}(asN4PY)	MA/DMA $Mn^{II}(py)_2$	$E°_{ox}$
4Me-DMA	3.27	4.2	-0.17	4Me-DMA	3.27	4.2	0.69
4H-DMA	2.6	3.6	0	4H-DMA	2.6	3.6	0.76
4Br-DMA	2	2.9	0.23	4Br-DMA	2	2.9	0.92
4CN-DMA	1.25	2.1	0.66	4CN-DMA	1.25	2.1	1.15

Table S18. Reactions of $[Mn^{II}(asN4Py)(CH_3CN)](CF_3SO_3)_2$ and $[Mn(py)_2\text{-}indH]^{2+}$ with DMAs by the use of PAA in CH_3CN at 30 °C. The plot of MA to MFA ratio against the $\boldsymbol{E}^{\circ}_{ox}$ of *p*-substituted DMAs

[S]	MA/DMA Mn^{II}(asN4py)	MA/DMA $Mn^{II}(py)_2$	σ_p
4Me-DMA	3.32	4.17	-0.17
4H-DMA	2.9	3.19	0
4Br-DMA	2	2.83	0.23
4CN	1.58	2	0.66

[S]	MA/DMA Mn^{II}(asN4PY)	MA/DMA $Mn^{II}(py)_2$	$E°_{ox}$
4Me-DMA	3.32	4.17	0.69
4H-DMA	2.9	3.19	0.76
4Br-DMA	2	2.83	0.92
4CN-DMA	1.58	2	1.15

Table S19. Reactions of $[Mn(py)_2\text{-}indH]^{2+}$ to oxidation of *N*,*N*-dimethylaniline with *m*-CPBA co-oxidants in CH_3CN at 30 °C. $[Mn^{II}]$ = 3 mM, [S] = 300 mM [Ox] = 300 mM

[Comp.]	[Comp.]:[S]:[Co-oxidant]	mmol prod.1	mmol prod.2	TON 1	TON 2	TON 1+2	Yield 1	Yield 2	Yield 1+2 (%)
$Mn(py)_2$-indH	3:300:300 (*m*-CPBA)	111.9	24.5	37.3	8.15	45.45	37.3	8.15	45.45
Mn(4-me-py)$_2$-indH	3:300:300 (*m*-CPBA)	107.9	26.4	36	8.8	44.8	36	8.8	44.8
$Mn(im)_2$-indH	3:300:300 (*m*-CPBA)	97.9	28.6	32.6	9.5	42	32.6	9.5	42
$Mn(bim)_2$-indH	3:300:300 (*m*-CPBA)	91.8	27.2	30.6	9	39.6	30.6	9	39.6
Mn(N-me-bim)$_2$-indH	3:300:300 (*m*-CPBA)	88.7	29.9	29.56	10	39.56	29.56	10	39.56
$Mn(tia)_2$-indH	3:300:300 (*m*-CPBA)	76.7	27	25.5	9	34.5	25.5	9	34.5